Impact of steel ladle preheating on the decarburization of a MgO-C refractory lining

Doctoral thesis at the Chair of Ceramics

Montanuniversität Leoben

Submitted by

Magdalena Drózd-Ryś

Leoben, March 2015

AFFIDAVIT

I declare in lieu of oath, that I wrote this thesis and performed the associated research myself, using only literature cited in this volume.

Acknowledgement

Even though this work is signed under my name, it would not have come into existence without help of others.

To begin with, I would like to thank Prof. Harmuth for having trusted on me to deal with the comprehensive subject of the thesis, as well for his remarks and hints and indications, who helped me to solve the several problems I have encountered.

I would like to thank Prof. Christian Weiss for our discussions on different aspects on the subjects. They often gave me a fresh look on my work. Additionally, thank you Christian for the inspiration on new mountain adventures!

I would like to thank my colleagues at the Chair of Ceramics for their support on my work and for the friendly work atmosphere.

Special thanks to the colleagues from the Chair for Process Technology and Industrial Environmental Protection for having offered me their laboratory equipment as well as their know-how.

Thank you, Diego for the proof-reading!

Effective work has to be balanced with fun and leisure, which I was guaranteed by spending free time with my friends, very often in the amazing Austrian mountains – thank you all for those precious moments!

Special thanks go to my family for having supported me on my studies and for having encouraged me to realize my dreams – dziekuję Wam Moja Rodzinko!

My husband Adam, who always stays by my side, no matter what, deserves great thanks: dziekuję Ci mój kochany Zbójku!

Finally, thanks to the industry partners to this project for having made it possible:

The research program of the competence center “Advanced Metallurgical and Environmental Process Development” (K1-MET) is supported within the Austrian program for competence centers COMET (Competence Center for Excellent Technologies) with funds of the Federal Ministry for Transport, Innovation and Technology, the Federal Ministry of Economy, the province of Upper Austria and Styria, the Styrian Business Promotion Agency, of the Tyrol and the Tyrolean Future Foundation.

Abstract

Steel ladles are lined with a variety of refractories including shaped and unshaped, basic and non-basic materials. In many cases non-basic castables are applied to the bath area as a wear lining. In the slag area magnesia carbon bricks, with their excellent corrosion resistance, proved to be a suitable refractory.

Steel ladles need to be preheated to avoid thermal shock damage to the refractory lining. The preheating process lasts up to 40 hours. A natural gas firing is used as energy source to preheat the refractory lining up to a temperature of 1000 °C. Due to the high excess air flow during combustion, the exhaust gas contains considerable amount of oxygen. At elevated temperatures this favors carbon burnout in MgO-C refractories and, thereby, negatively influences their initial corrosion and erosion resistance.

The aim of this thesis was then to analyze the impact of steel ladle preheating procedure on possible decarburization of MgO-C refractories. This was done by:

a) Establishing a kinetic model for carbon burnout in MgO-C refractories and its experimental evaluation at laboratory scale.
b) Simulation of steel ladle preheating via computational fluid dynamics (CFD), of which output should give data to predict possible carbon burnout in MgO-C refractories.

The carbon burnout occurs via direct oxidation to carbon monoxide:

$$2C(s) + O_2(g) \rightarrow 2CO(g).$$

The kinetic model of carbon burnout was based on the shrinking core model with three resistances: mass transfer of oxygen from the gas bulk at the refractory surface, effective diffusion of oxygen in the refractory pores, and chemical reaction of oxygen with the carbon. The conversion of carbon j_R^C – in moles per second and square meter – is described with the following equation:

$$j_R^C = \frac{2 \cdot C_b^{O_2}}{\dfrac{L}{D_{eff}} + \dfrac{1}{k_m} + \dfrac{1}{k_c}}.$$

In the equation $C_b^{O_2}$ is the oxygen concentration in the gas bulk, L the depth of decarburized, layer, D_{eff} the effective diffusion coefficient, k_m the mass transfer coefficient and k_c chemical rate coefficient. The effective diffusion was determined for various MgO-C refractory materials by thermogravimetric analysis. Received values showed dependence on the temperature of the sample, with the exception of the resin bonded MgO-C refractory material M1, which contained antioxidants (AOXs). The second factor influencing D_{eff} was the carbon content of the material. The mass transfer coefficient was described with dimensionless variables: Sherwood number, Reynold's number and Schmidt number. Oxidation tests with pure graphite were conducted to compare calculated values with those determined by the experiment. The chemical rate coefficient was defined with a literature-based Arrhenius equation.

Oxidation tests with MgO-C samples were conducted to verify the proposed model. Investigated materials had various carbon contents: type M1 – 11 wt%, M2 – 10.5 wt%, M3 – 12.5 wt% and M4 – 16 wt%. The samples were tested at 600, 700, 800, 900 and 1000 °C. The carbon conversion depended on the temperature, whereupon a significant increase of carbon conversion was noticed between 700 and 800 °C. The applied air flow rate during the experiment negligibly influenced the decarburization depth of the MgO-C material. The decarburization depth was calculated using proposed kinetic model and applying various equations for chemical rate coefficient and then compared with experimental data. According to that study, the graphite kinetics has to be considered for the calculation of carbon burnout in MgO-C refractory material at the temperatures lower than 900 °C.

The second goal of the thesis was the simulation of ladle preheating, which was executed in ANSYS Fluent software as a transient simulation. The heat release from gas combustion during preheating and the exhaust gas composition were calculated by a non-premixed approach with the addition of the laminar flamelet concept. The convective heat transfer at the ladle lining walls was solved using the standard wall functions, available within the realizable k-ε turbulence model. The radiative heat exchange was described by Discrete Ordinates model.

Considering the possible carbon burnout in MgO-C lining, the regions with lining temperatures exceeding 800 °C were of interest. According to the calculations those temperatures occur after 35 hours of preheating. The oxygen mole percentage was located between 6 and 12 % within that period; the calculated mass transfer coefficient was in the range of 0.003 – 0.015 m/s.

Based on CFD calculations the prediction of MgO-C refractory decarburization during ladle preheating was possible. The depth of the decarburized layer at the end of preheating was in the range of 3 and 5.5 mm depending on the analyzed MgO-C refractory material, the applied mass transfer coefficient and the chemical rate coefficient. The carbon burnout curves of MgO-C materials M2 and M3 were similar and the decarburized depth equaled to 4.1 or 5.1 mm depending on applied chemical rate correlation. Carbon burnout in material M1, which contained AOXs proceeded similar as in materials M2 and M3 up to the 37th preheating hour. Afterwards, the oxidation is retarded. This behavior is connected with the effective diffusion coefficient within the refractory, which in case of material M1 is temperature independent. Therefore, the application of AOX seems to be more reasonable, if the lining operation temperature mostly exceeds 800 °C. The oxidation depth at the end of preheating was for M1 in the range of 3.5 or 4.6 mm depending on the applied chemical rate and it is similar as in pitch bonded refractories M4.

The model proposed for carbon burnout kinetics in MgO-C refractories was accurate enough for the purpose of this work. However, for further investigations, the proposed model should be reviewed on the influence of the convective mass transfer on carbon oxidation rate. Also, investigation of carbon burnout via other reactions, like e.g. Boudouard reaction, in MgO-C refractories would be of interest, as well as the oxidation kinetics at lower temperatures.

Table of contents

1 Problem definition

Steel ladles are lined with a variety of refractories including shaped and unshaped, basic and non-basic materials. In many cases non-basic castables are applied for the bath area as a wear lining. On the other hand, in the slag area magnesia carbon bricks with their excellent corrosion resistance proved to be a suitable refractory.

Steel ladles are preheated to avoid thermal shock damage to the refractory lining. Castables contain a considerable amount of water immediately after installation and therefore the preheating process has to be proceeded slowly and lasts up to 40 hours. During the first five hours, the ladle is purged with hot air only. Afterwards, natural gas firing is used as energy source to preheat the refractory lining up to a temperature of 1100 °C. Because of high excess air amount during combustion, there is considerable oxygen content in flue gas. At elevated temperatures this favors carbon burnout in MgO-C refractories and thereby negatively influences the corrosion and erosion resistance.

The aim of this thesis is to analyze the impact of steel ladle preheating procedure on possible decarburization of MgO-C refractory. This study comprises two sub-goals:

a) To establish a kinetic model for carbon burnout in MgO-C refractories. Within such a model, reaction limiting-factors, like diffusion and mass transfer coefficient will be defined and determined. The model will be experimentally evaluated at laboratory scale.

b) To simulate steel ladle preheating via computational fluid dynamics (CFD), the output of which should give a better understanding of the process phenomena and the necessary data to predict possible carbon burnout in MgO-C refractories. The expected results will be: the temperature distribution in the exhaust gas and in the lining as well as the exhaust gas composition.

Moreover, aided by the kinetic model and the data obtained from the CFD simulation such as lining temperature and oxygen concentration the decarburization rate of MgO-C refractory during preheating of the steel ladle will be estimated.

Finally, a computer program for calculating carbon burnout as a function of the lining temperature and oxygen concentration will be written.

2 State of the art

2.1 MgO-C refractories

Magnesia refractories are used in a multitude of heat processing industries, however the greatest quantity is applied in the steel industry. The types and amounts of magnesia refractories have changed greatly over years. In the 1950s and 1960s open-hearth furnaces were lined with an array of magnesia refractories: chemical bonded, burned, direct-bonded and fused-cast magnesia-chrome brick and magnesia ramming mixes. The development of the basic oxygen steel-making furnace (BOF) ushered in pitch-bonded doloma, doloma-magnesia, magnesia-doloma and magnesia bricks for construction of the vessel linings. In the late 1960s, high-strength pitch-impregnated, burned magnesia bricks were developed with magnesia levels of about 95% MgO. These bricks were used in place of pitch-bonded types in the higher-wear areas of BOF linings. In the mid-1970s, the Japanese introduced resin-bonded magnesia-carbon refractories for electrical arc furnaces (EAF). Within a short time period, graphite became the main carbon ingredient of this type of bricks with contents up to 35% tried in EAF hot spots. In the early 1980s, resin-bonded magnesia-carbon bricks were applied to high-wear trunnion areas of BOFs with very good results. These trials began a period of new and upgraded magnesia-carbon developments as well as experimentation in BOF zoning. Such a period has lasted to the present. The technological changes of secondary metallurgy in 1970s led to current ladle metallurgical furnace (LMF) designs with bauxite castable or brick in the working bottom and resin-bonded magnesia-carbon brick in the working slagline. The application of magnesia refractories in LMF slagline now represents the largest utilization for this class of refractories [1].

The use of magnesia for the fabrication of basic refractories developed gradually from inexpensive doloma refractories, through highly resistant magnesia linings to MgO-C refractories containing graphite [2]. The main component of magnesia refractories is magnesia (MgO), which has only one crystalline modification named *periclase*. Magnesium oxide is characterized by very high refractoriness: the melting point equals to 2800 °C. As there are no natural resources of periclase the magnesia is gained mostly as magnesite ($MgCO_3$) or dolomite ($(Mg,Ca)CO_3$) or brucite ($Mg(OH)_2$). The other possible sources of magnesia include sea-water, brines and deposits of MgO-rich salts in form of $MgCl_2$. For the synthesis of high-purity, fine-graded MgO raw materials chemical techniques are used [2], [3]. Typical basic raw materials for magnesia bricks are sintered magnesia and fused magnesia. The main properties of magnesia are high melting point, hot strength, high thermal conductivity and high resistance against basic slags and alkali oxides. These properties depend on the type and the amount of accompanying elements and the phase composition. In these cases a very important criterion is the $CaO:SiO_2$ mass ratio and the B_2O_3 content in seawater magnesia, as they both influence its melting point [3], [4]. Pure magnesia refractories show high Young's modulus and a low thermal shock resistance. To improve the thermal shock resistance, different additives, like spinel or chrome ore, are applied [4]. Another possibility to increase thermal shock resistance is a pitch bond. [4].

Carbon containing magnesia bricks can be divided into three groups:
- Carbon containing burned magnesia bricks (< 2 % C);
- Carbon bonded magnesia bricks (< 7 % C);
- Magnesia carbon bricks (≥ 7 % C).

The advantages of carbon in magnesia bricks come with the increase of thermal shock resistance. Furthermore, the infiltration depth of the slag is reduced as a consequence of the poor wettability of carbon on the one hand, and the reduction of iron oxide to metallic iron and thereby increase of eutectic temperature on the other hand [5]. The disadvantage of carbon containing magnesia bricks is that its application is restricted to inert atmospheres, because of possible carbon burnout, since it could further lead to a decrease of brick's mechanical strength or slag infiltration into the refractory and corrosion [1], [6].

Different kinds of carbon, like graphite or carbon black can be added. Additionally, these refractories are usually carbon bonded with resin or pitch, resulting in a high carbon residue after coking.

The manufacture of **carbon containing burned magnesia bricks** includes a pitch impregnation step at a temperature of 150 – 200 °C, producing maximum 2 % of residual carbon after burning. The application of such a bricks is restricted to the cases where very high erosion resistance is required [5].

The typical binder for **carbon bonded magnesia bricks** is pitch. After mixing magnesia and pitch at 100 – 200 °C the bricks are pressed and afterward tempered at 250 – 350°C to achieve satisfactory hot strength. The other possible binder is resin, partly also used for bricks containing 5 % residual carbon. Carbon bonded magnesia bricks are usually applied in the steel industry, especially in working lining of basic oxygen furnace (BOF), but also in electric arc furnaces (EAFs) [5].

Magnesia carbon bricks (MgO-C) differ from the other carbon-containing bricks in the graphite addition, which results in carbon content higher than 7 %. Two different binders are used: pitch bond with maximal 15 % of carbon content, possible also with a combination of pitch impregnation and resin bond with maximal 25 % of carbon and the possible addition of antioxidants (AOXs) in the form of metallic Si, Al, Mg. Lately B_4C, CaB_6, ZrB_2 and TiB_2 have also been introduced [1], [5]. Adding AOX to magnesia carbon bricks improves their oxidation resistance and mechanical strength. The manufacture of pitch bonded MgO-C bricks includes mixing magnesia and pitch at 100 – 200 °C, pressing and tempering at 250 – 300 °C. The resin bonded bricks are manufactured with phenol resol or phenol novalac solution at temperatures lower than 100 °C and afterwards hardened at 100 – 120 °C [5]. The properties of MgO-C bricks are embossed by graphite: density, cold strength and thermal expansion decrease, while thermal shock resistance and heat conductivity increase compering with magnesia bricks without carbon addition. Application of MgO-C bricks is restricted to non-oxidizing atmospheres. Examples of the employment of magnesia carbon bricks include converters, steel ladles, and electric arc furnaces [4].

2.1.1 Carbon sources in MgO-C refractories

The reasons for including carbon in steel-making refractories are high refractoriness and thermal stability in non-oxidizing conditions, poor wettability, high thermal conductivity and the increase of thermal shock resistance Main carbon sources in general use in refractories are pitch used as a binder and impregnate, resins used as a binder and graphite and carbon black used as matrix component for improvement of refractory properties [1], [7].

Carbon black and graphite

Carbon blacks are formed in the absence of air by thermal decomposition of natural gas in a previously heated chamber containing checkerwork. The refractory industry generally uses a thermal carbon black type, because of its surface area, which should be as low as possible to minimize the level of added liquid binder [1].

Graphite could be divided into three classes for commercial purposes:
- Flake – a scaly or lamellar form with each flake being a separate crystalline particle in metamorphic rock;
- Crystallite – found in rocks as veins or pocket accumulation;

- Amorphous – occurs in metamorphic rocks as minute, blocky, cryptocrystalline, graphite particles [1].

In Mg-O refractories almost only flake graphite is applied, which can have many grades usually based on particle size and carbon purity. For the refractory industry, the coarsest grades with wide-particle size distribution and high carbon purity are of interest. Additionally, the ash content is important. The ashes should be examined for their refractoriness and compatibility with the refractory body – high contents of alkalis should be avoided [1].

The structure and properties of crystalline graphite are well known. The bond strengths in the two principal directions within the crystal are the highest and lowest possible, leading to a large anisotropy in the properties in these two crystallographic directions. The strong bonding within the graphene layers results in high theoretical values of the elastic modulus in this plane, which contrasts drastically with the low shear modulus parallel to the graphene layers. This deformability is important during the fabrication of graphitic composites, enabling the flakes to effectively fill the spaces between the aggregate in oxide composites. The anisotropy of graphite manifests also in its chemical behavior. Oxidation takes place from the edges of the graphene layers, at the edges of crystals or where vacancies in exposed graphene layers reveal such edge atoms. Oxidation of pure graphite crystals follows well defined crystallographic directions creating hexagonally shaped etch pits. Impurities in the graphite may be catalytically active and act predominantly at the edges of pits where they are mobile and catalyze the reaction in their wake [7].

Binders

The most common binders for MgO-C bricks are pitch and resin.

Pitch is a complex material obtained mostly from the thermal decomposition of coal or sometimes petroleum. Coal-tar pitch is the oldest used organic binder in the production of magnesia–carbon bricks. Its benefits include good adhesion to the granules, plastic deformability at low temperatures (low softening point for improved wetting), high yield of coke with an anisotropic structure and low costs. A major drawback of this product is its content of carcinogenic aromatics, especially benzo[a]pyrene (about 10,000–13,000 ppm) [8]. At a temperature higher than 400 °C an isotropic molten phase is formed, which grows under the impact of the continued release of volatile aromatics and the separation of hydrocarbon radicals and eventually is transformed into a solid phase at about 500 °C. Radicals continue to be separated and are eliminated through condensation reactions to produce larger polynuclear species. In the further course of pyrolysis density of the coke phase increases and at temperatures between 900 °C and 1000 °C, the material exhibits an anisotropic coke skeleton similar to that of graphite [9]. Some of these processes occur during the production of the pitch whereas others may be active during the thermal processing of the pitch within the refractory material itself. The degree of aromaticity is greater for coal-tar pitch than for petroleum pitch [7]. Product development leads to new innovative low-toxic carbon binders, like for example Carbo-Resin, where coal tar pitch is treated at high temperatures under vacuum or Polymer Binder, a specific petroleum derived binder, generated by thermal cracking of the gas oil fraction from crude oil [10], [11]. The graphitic-like structure derived from pitch significantly influences the oxidation behavior of the coke. Petroleum pitch derived cokes demonstrate the greatest oxidation resistance in comparison to coal tar pitch or phenol resin derived cokes [10]. A usual type of coal tar pitch binder leads to a greater residual carbon content than the phenol resins. This leads to a higher strength of the coked pitch-bond samples after pyrolysis [9].

The softening point of the tar pitches is in the range of 70 – 80 °C, so they are processed at a temperature of 120 – 150 °C to guarantee sufficiently low viscosity. In many cases, the molding process is followed by tempering at 300 – 450 °C to eliminate a part of the volatile components [10]. Pitch is used also for impregnating previously shaped refractories to enhance the brick's slag resistance [1]. Pitch-bonded brick has an ability to deform under load at higher temperatures [6].

Phenolic resins applied in the refractory industry are mainly novolacs and resols [1]. Phenolic resins are an alternative to coal tar pitch and are frequently used organic binder in the production of magnesia–carbon bricks. They allow carrying out both moulding and mixing at room temperature. The coking residue of resin binders is always less than that of high-quality pitches. Unlike pitch, phenol formaldehyde resin binders show a thermosetting behavior. At a temperature between 150 and 200 °C the resins harden either directly or catalytically. A high-molecular phenol structure, called the resite skeleton, is formed. The pyrolysis of resite begins above 350 °C with the separation of phenols, cresols, xylenes and lower oligomers as well as the release of hydroxyl groups. Later on, small amounts of aromatic cores are separated at above 550 °C. As the result of pyrolysis, a polymeric carbon skeleton with a spatially interlinked band structure is formed, what can be characterized as widely isotropic [9]. The isotropic phase of the coke residue results in lower oxidation and corrosion resistance [8].

2.2 Kinetic model of carbon burnout in MgO-C refractories

Carbon burnout in MgO-C refractory should be considered as a heterogeneous reaction, in which gas contacts solid and reacts into a gaseous product. Decarburization in magnesia-carbon refractories may occur through direct carbon burnout by oxygen (direct oxidation), characterized by Eq. (1), indirect oxidation described by Eq. (2), through Boudouard reaction presented by Eq. (3) or reaction with water described by Eq. (4) [12].

.

$$2C(s) + O_2(g) \rightarrow 2CO(g) \tag{1}$$

$$MgO(s) + C(s) \rightarrow Mg(g) + CO(g) \tag{2}$$

$$C(s) + CO_2(g) \leftrightarrow 2CO(g) \tag{3}$$

$$C(s) + H_2O(g) \leftrightarrow CO(g) + H_2(g) \tag{4}$$

Reaction (2) becomes important at temperatures greater than 1400 °C ([13] – [16]) and is therefore not considered for ladle preheating. The rates of carbon oxidation by steam and carbon dioxide are of the same order of magnitude and are generally much less than the reaction of carbon with oxygen. Estimated carbon conversion at 800 °C and 10 kPa pressure were in relation to each other 1 for CO_2, 3 for H_2O and 10^5 for O_2. [17]. Detailed kinetic information for reactions (1) (3) (4) can be found in [17] – [23]. Direct oxidation with oxygen defined in Eq. (1) plays the decisive role for carbon burnout during steel ladle preheating.

2.2.1 Carbon burnout reaction kinetics

The kinetics of carbon burnout in MgO-C refractories can be described with the help of the shrinking core model as described in [24] – [26]. The kinetics of heterogeneous reaction differs from the homogenous reactions, as the reaction rate equation incorporates mass transfer terms in addition to the usual chemical kinetics term. Solid material may shrink during reaction or remain unchanged in size if it contains large amounts of impurities or if they form a firm reaction product. The shrinking-core model assumes that the reaction occurs at first at the outer skin of the material. Within time, the zone of reaction moves into the solid, leaving behind completely converted material and inert solid (e.g., ash; decarburized MgO-C layer). During conversion, there is an unreacted core of material, which shrinks. The limitation of the shrinking core model is a sharp interface between ash and fresh solid. In the case of rather diffusive reaction front a progressive-conversion model is more suitable [24]. Fig. 1 illustrates the principle of the shrinking-core model.

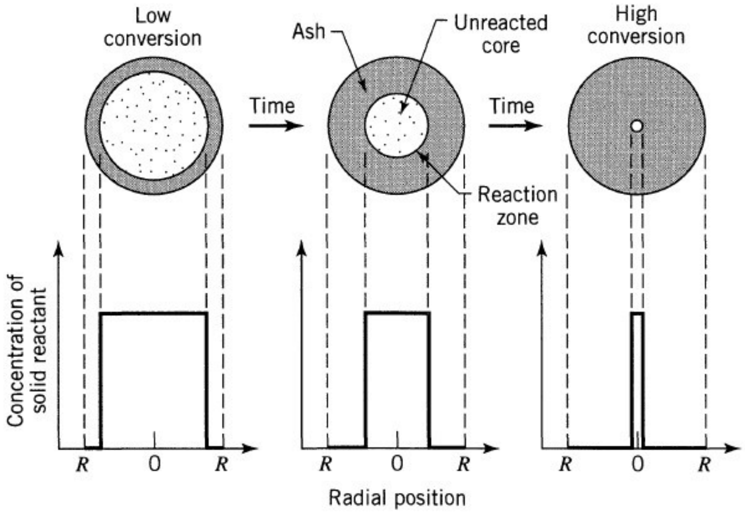

Fig. 1: Illustration of the shrinking core model presented by [24]. Reaction proceeds at a narrow front which moves into the solid particle. In this case the reactant is completely converted as the front passes by.

Shrinking-core model was developed by Yagi and Kunii [27], who visualized five steps occurring during reaction: i) beginning with diffusion of gaseous reactant through the concentration boundary layer surrounding the solid surface, ii) penetration of ash/inert layer, iii) reaction of gaseous reactant with solid, and iv) diffusion of gaseous products through the ash layer, and v) boundary layer back into the gas bulk. The kinetic of carbon oxidation within MgO-C refractory was described in similar manner by several authors: [12], [28], [29], [30].

The kinetics comprises five steps described by equations (5) - (9), where C_b, C_s and C_t represent concentrations in the gas flow bulk, at the surface of the oxidizing sample, and at the reaction interface, respectively. The species is indicated by a superscript. The constants k_m, D_{eff}, k_c and K_E, are the convective mass transfer coefficient, effective diffusivity, rate coefficient of heterogeneous chemical reaction, and the equilibrium constant for the reaction (1). The radius of the sample is represented by r_0, the sample's length by l and r_t is the radius of unoxidized cross-section. Molar flux of the reacting species is denoted by j_n. In Fig. 2 a micrograph of already used MgO-C refractory with schematic illustration of the kinetic model of carbon oxidation with all reaction steps is presented.

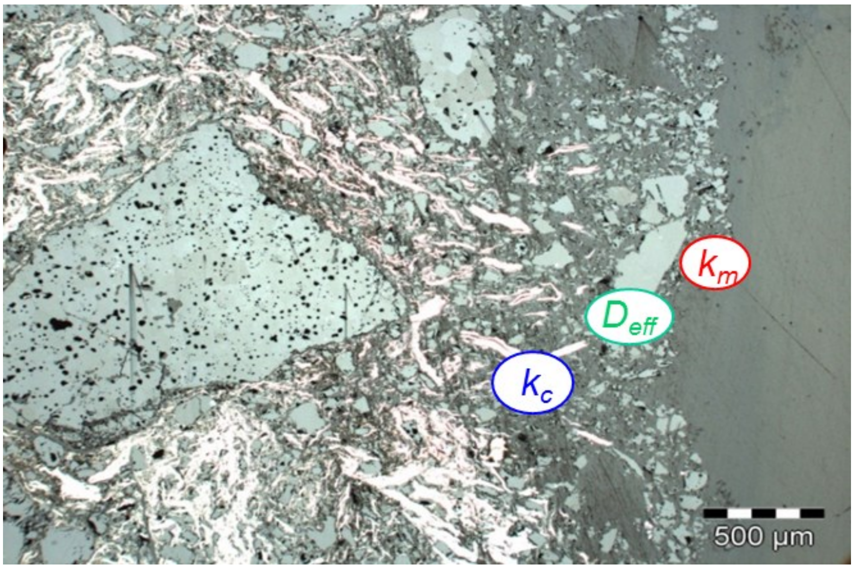

Fig. 2: Micrograph of already used MgO-C refractory with schematic representation of the kinetic model for carbon oxidation.

At first oxygen is transported from the gas bulk to the refractory surface (inward mass transfer). The molar flux of oxygen, $q_1^{O_2}$, from the gas phase to the specimen surface is:

$$q_1^{O_2} = 2 \cdot \pi \cdot r_0 \cdot l \cdot k_m \cdot \left(C_b^{O_2} - C_s^{O_2} \right) \qquad (5).$$

Here the dimension of the concentrations is in moles per volume. Afterwards, oxygen diffuses through the already reacted porous refractory layer (inward diffusion). The molar flux of oxygen, $q_2^{O_2}$,from the surface to the reaction interface is:

$$q_2^{O_2} = 2 \cdot \pi \cdot l \cdot D_{eff} \frac{(C_s^{(O_2)} - C_t^{(O_2)})}{\ln\left(\frac{r_0}{r_t}\right)} \qquad (6).$$

At the reaction interface oxygen reacts with carbon to carbon monoxide (chemical reaction). The molar flux *of* O_2, $q_R^{O_2}$, oxidizing C at the reaction interface is:

$$q_R^{O_2} = 2 \cdot \pi \cdot r_t \cdot l \cdot k_c \left(C_t^{(O_2)} - \frac{\left(C_t^{(CO)}\right)^2}{K_E} \right) \qquad (7).$$

In Eq. (7) K_E is equilibrium constant for the reaction (1) given in mol/m^3. Carbon monoxide diffuses then through the porous layer to the refractory surface (outward diffusion). The molar flux of CO, q_1^{CO}, from the reaction interface to the surface is:

$$q_1^{CO} = 2 \cdot \pi \cdot l \cdot D_{eff} \frac{(C_t^{(CO)} - C_s^{(CO)})}{\ln\left(\frac{r_0}{r_t}\right)} \qquad (8).$$

After that CO is transferred from the refractory surface into the gas bulk (outward mass transfer). The molar flux of CO, q_2^{CO}, from the sample surface to the surrounding atmosphere is:

$$q_2^{CO} = 2 \cdot \pi \cdot r_0 \cdot l \cdot k_m \cdot \left(C_s^{CO} - C_b^{CO} \right) \tag{9}.$$

With the assumption that the oxidation process is at a quasi-steady state due to the slow progression of reaction front, the above five steps take place at the same rate for a short period from t to $t + dt$ and based on the mass balance we receive Eq. (10):

$$2q_1^{O_2} = 2q_2^{O_2} = 2q_R^{O_2} = q_1^{CO} = q_2^{CO} \tag{10}$$

Combining Eq. (10) with Eq. (5) – (7) recognizing that

$$q_R^C = 2 \cdot q_R^{O_2} \tag{11},$$

and considering that equilibrium concentration of oxygen in Eq. (7) is very small, so the second term in the bracket could be set to zero, $q_R^{O_2}$ can be defined with Eq. (12):

$$q_R^{O_2} = \frac{2 \cdot \pi \cdot l \cdot C_b^{O_2}}{\frac{\ln(r_0 / r_t)}{D_{eff}} + \frac{1}{r_0 \cdot k_m} + \frac{1}{r_t \cdot k_c}} \tag{12}.$$

The molar flux density of oxidized carbon, j_R^C, may also be equated to the rate of disappearance of solid carbon (in mole) per unit time and per unit of interface area S_t, so that:

$$j_R^C = \frac{1}{S_t} \cdot q_R^C = \frac{1}{2\pi \cdot r_t \cdot l} \cdot q_R^C \tag{13}.$$

The molar flux density of oxidized carbon is then defined by Eq.(14):

$$j_R^C = \frac{2 \cdot C_b^{(O_2)}}{\frac{r_t \ln(r_0 / r_t)}{D_{eff}} + \frac{r_t}{r_0 \cdot k_m} + \frac{1}{k_c}} \tag{14}.$$

Carbon conversion defined in Eq. (14) is determined by three resistances: mass transfer at the solid surface, diffusion in the pores and chemical reaction. The overall reaction rate is limited by the largest single resistance.

The conversion of carbon can also be described as a radius change in the time as it is done in Eq.(15):

$$\frac{dr_t}{dt} = -\frac{2}{C^{(C)}} \frac{C_b^{(O_2)}}{\frac{r_t \ln(r_0 / r_t)}{D_{eff}} + \frac{r_t}{r_0 \cdot k_m} + \frac{1}{k_c}} \tag{15},$$

where $C^{(C)}$ is the molar concentration of graphite in the MgO-C refractory. Integration of both sides of Eq. (15)

$$\int_{0}^{t} \frac{2 \cdot C_b^{(O_2)}}{C^{(C)}} \cdot dt = -\int_{r_0}^{r_{t\_end}} \left(\left(\frac{\ln(r_0)}{D_{eff}} + \frac{1}{r_0 \cdot k_m} \right) \cdot r_t - \frac{1}{D_{eff}} \cdot r_t \cdot \ln r_t + \frac{1}{k_c} \right) \cdot dr_t \qquad (16),$$

yields a relation between the radius of the unoxidized cross-section r_t and the oxidation time t:

$$t = \frac{\rho_{M_C}}{2 \cdot C_b^{(O_2)}} \cdot \left(\frac{1}{2D_{eff}} r_t^2 \cdot \ln r_t - \left(\frac{\ln(r_0)}{D_{eff}} + \frac{1}{2r_0 \cdot k_m} + \frac{1}{4D_{eff}} \right) r_t^2 - \frac{1}{k_c} \cdot r_t + + \left(\frac{r_0}{2k_m} + \frac{r_0^2}{4D_{eff}} + \frac{r_0}{k_c} \right) \right) \qquad (17).$$

The determination of the diffusion coefficient D_{eff} in a different experimental setup has been presented in [12]. The sample was placed in such a manner that there was only one contact surface of cylinder cross-sectional face for gas and solid and the carbon oxidation occurred uniaxial. The depth of decarburization L was than presented as in Eq.(18):

$$\frac{dL}{dt} = \frac{2}{C^C} \frac{C_b^{O_2}}{\frac{L}{D_{eff}} + \frac{1}{k_m} + \frac{1}{k_c}} \qquad (18).$$

In Eq.(18) C^C is the carbon molar concentration in the refractory material. The molar flux density of oxidized carbon, j_R^C, is then:

$$j_R^C = \frac{2 \cdot C_b^{O_2}}{\frac{L}{D_{eff}} + \frac{1}{k_m} + \frac{1}{k_c}} \qquad (19).$$

According to Eq. (14) the oxidation limiting step can be the chemical reaction, the pore diffusion or the mass transfer from the gas to the solid. Several authors [17], [21], [26], have postulated a temperature dependence of the rate controlling mechanism. Fig. 3 presents this graphically: at low temperatures (zone I) chemical reaction is the rate-determining step. Here, the experimentally observed activation energy will be the true activation energy. Zone II is characterized by control due to both chemical reaction and diffusion. The observed activation energy will in this case be roughly half of the true value. At high temperatures mass transfer is the limiting factor (zone III). The activation energy shows very small values.

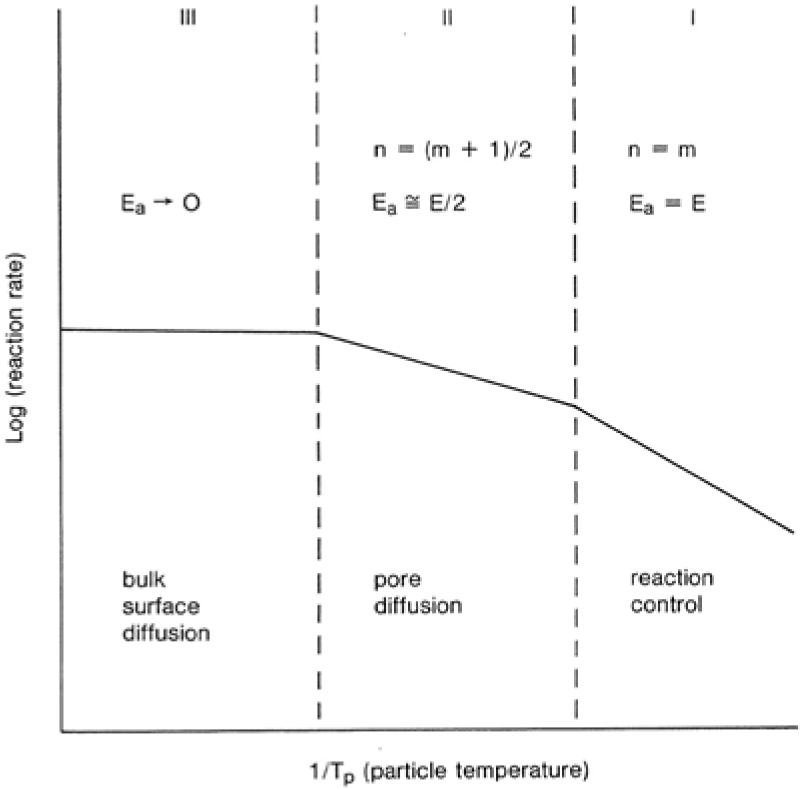

Fig. 3: Rate-controlling regimes for heterogeneous reaction [17]. E_a is the apparent activation energy, E true activation energy, n the apparent reaction order, m the true reaction order.

2.2.2 Kinetics of graphite oxidation

In Eq. (14) one of the reaction-limiting factors is the chemical reaction rate coefficient, k_c. In many studies concerning carbon burnout in MgO-C refractories this parameter is not taken into consideration as it has no or hardly influence on the general reaction rate. This assumption can be justified at high temperatures, exceeding 1000 °C. However, k_c strongly depends on the temperature, as expressed by Arrhenius equation described by Eq. (20):

$$k_c = A \cdot e^{-E_a/(RT)} \tag{20}$$

where A is a pre-exponential factor, E_a the activation energy in J/mol, R the general gas constant equal to 8.314 J/molK and T the temperature in Kelvin. The activation represents the minimum energy content of reacting molecules before the reaction will occur. It is determined experimentally by carrying out the reaction at different temperatures. The larger the activation energy, the more temperature-sensitive is the rate of reaction [25].

Within MgO-C refractories at elevated temperatures two carbon bearing phases are present: graphite and residual carbon from the binder. The intrinsic chemical reaction rates vary strongly, depending on the carbonous material. In general, it has been found that the more pure forms of carbon are less reactive than the chars [17].

Many studies have been carried out to describe the kinetics of graphite oxidation [32] – [39]. The determined activation energies were located in the range of 165 – 190 kJ/mol, depending on the applied temperatures or used material, the greatest value of 218 kJ/mol has been found in [33], whereas the lowest in [19] and [40]. Estimated order of reaction for graphite oxidation varied between 0 and 1. Within his study, Chi et al. [32] noticed the effect of the coke type on the oxidation behavior at temperatures of 603 °C and 702 °C. The graphite made of pitch coke showed a greater resistant to oxidation than that derived from petroleum coke for both temperatures. This effect of the coke type nearly disappeared at temperatures of 808 °C and 911 °C. Further, it has been shown that oxidation rate increases drastically, of about 10-14 times, between temperatures of 702 °C and 854 °C. Between 854 °C and 911 °C oxidation rate does not change significantly anymore. In studies done in [33], the oxidation rate did not change above the temperature of 1060 °C.

Smoot [17] and Smith [41] presented a review of oxidation rate parameters for various char types. The kinetic parameters varied strongly depending on the material, as well as its thermal history, specific surface or present impurities in the char. Activation energies of the presented chars were significantly less than the graphite activation energies and ranged between 60 – 100 kJ/mol.

Fig. 4 presents oxidation rates of carbon materials, graphite and various chars, depending on the temperature. The values of the oxidation rate are plotted at logarithmic scale.

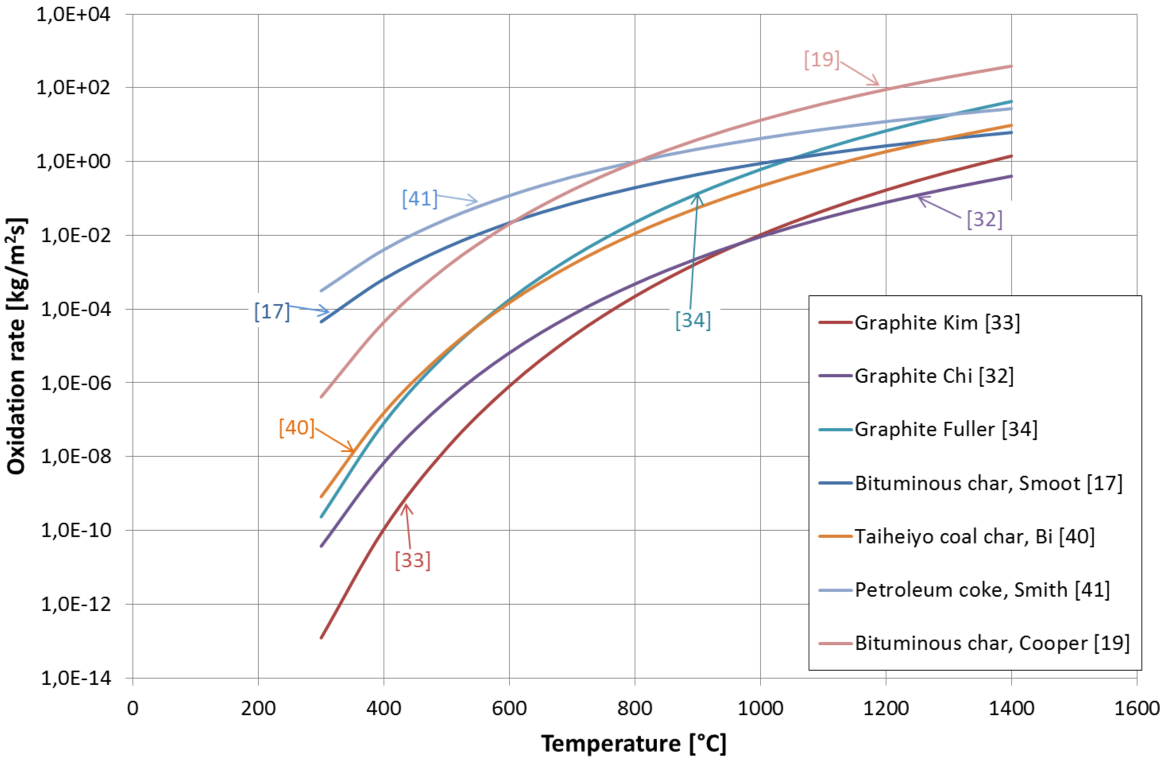

Fig. 4: Oxidation rates of carbon materials, graphite and various chars, versus temperature. The curves were calculated based on the studies presented in [17], [19], [32], [33], [34], [40], [41].

2.2.3 Further factors influencing carbon burnout

A number of authors have studied the oxidation of magnesia carbon refractories considering the influence of temperature, carbon content, carbon type, grain size and antioxidants on the oxidation [13], [15], [29], [30], [42] – [50]. An attempt to summarize these studies can be found in [42]. Most of the reports concerned resin bonded bricks, the only exception being [42].

Carbon content

Most of the studies show that the oxidation rate decreases with increasing carbon content [42], [43], [48],. However, [43] remarks that the thickness of the oxidized layer decreases with increasing graphite content. Also carbon particle size impacts the oxidation behavior. According to [42], [48] and [52] larger carbon particle size improves the resistance. Following that graphite flakes are recommended instead of carbon black.

Atioxidants

Metal powder additives, named antioxidants (AOX), are commonly applied in resin-bonded magnesia-carbon bricks. The main purposes of the AOXs are to increase oxidation resistance in resin-bonded MgO-C refractories and to reinforce the bond. The most common antioxidants used in MgO-C grades are aluminum and silicon powders. Other less frequently used additives include Al-Mg, Al-Si, Mg-Si, carbides, and borides [50]. Numerous investigations have been performed to describe the impact of AOX on the oxidation resistance of MgO-C bricks [8], [28], [29], [44], [46], [47], [50], [53], [54].

Aluminum revealed to be one of the most common and effective antioxidants. It melts at 660 °C and forms Al_4C_3 and AlN at approximately 800 °C. At higher temperatures Al_4C_3 decomposes and reacts with O_2 or CO to form Al_2O_3. Together with MgO, magnesium aluminate spinel is then generated. These newly formed reaction products increase the hot strength and, due to the reduced apparent porosity, oxidation resistance is increased. A disadvantage of Al_4C_3 is the susceptibility to hydration, which can destroy the microstructure and thus the entire brick [50].

In [28] and [29] the authors investigated the effect of Al and alumina addition on the MgO-C oxidation rate at various temperatures and 10% graphite content. The used binder was phenolic resin. In both cases, an increase of Al content showed a decrease of the oxidation rate. In [8], the effect of TiO_2- and Al-additions on the oxidation resistance and the mechanical properties of MgO–C refractories were examined. The samples contained 12 wt% of natural graphite flakes and various Al and TiO_2 contents. The investigations showed that the addition of TiO_2 and TiO_2/Al in carbon bonded refractories leads to the formation of TiCN and TiC, respectively, which improved the oxidation resistance. Furthermore, TiO_2 in carbon-bonded refractories with Al as an antioxidant contributes to the formation of mainly crystalline Al_4C_3, Al_2OC and Al_4O_4C whiskers, which present a higher oxidation resistance in comparison to amorphous whiskers containing Al, C and O.

Silicon is the second most common metallic powder applied in resin-bonded MgO-C bricks as an AOX. Combined with aluminum powder, the formation of silicon carbide occurs below 1000 °C, which also results in higher structural strength. Near the hot face, a dense forsterite zone is formed from the reaction of oxidized silicon carbide and MgO, increasing thus the oxidation resistance of the brick. Furthermore, the mixed Al-Si carbide has an increased hydration resistance. The disadvantages of such additives can be higher brittleness and increased expansion [50], [55].

In [47] the oxidation behavior at temperature range from 1000 °C to 1600 °C with antioxidants like Al, Si, SiC and 7-13 % graphite content in bricks was studied. According to the investigation results Al was the most effective antioxidant at lower temperatures (1100 °C-1200 °C), while Al+Si or Al+SiC at higher temperatures (>1300 °C).

Boron carbide (B_4C) is one of the newly introduced antioxidants. It reacts with oxygen to form boric acid, which reacts further in the matrix to generate viscous, low temperature melting phases. In theory, these phases form a protective film covering the pore walls and carbon components, thereby reducing oxygen attack. Essential for the effectiveness of B_4C is the amount of B_4C added; however, particle grain size has also influence. The formation of boron-containing liquid phases appears to lower the brittleness of the brick compared with other antioxidants. A further positive side effect of boron carbide addition is very effective hydration protection [50]. Boron carbide showed high effectiveness in combination with the commonly used Al and Si metal powders.

In [44], the authors examined and compared the effects of different antioxidants, Al, Si, SiC and B_4C on the oxidation resistance of magnesia–carbon refractory bricks at temperatures of 1300 °C and 1500 °C. The material contained 15 wt % graphite and 1% or 3 wt % of AOX. Phenolic resin was used as a binder. According to the experimental results, B_4C turned out to be the most effective antioxidant at both temperatures. The second most effective AOX was the Al. The SiC was the least effective antioxidant at both temperatures. Similar results were achieved by [45]. Within these experiments effective diffusion coefficients of oxygen in MgO-C refractories were determined for Mg, Al, Si, SiC and B_4C as antioxidants. Testing temperature was 1200 °C, AOX content varied between 1-7%. The results showed that B_4C was the most effective addition to block the diffusion path for oxygen. The second most efficient AOX was Si. SiC and Al had similar effective diffusion coefficients which were approximately 1.5 larger of those of Si. Mg had no positive influence on oxidation resistance. In all cases, except Mg, with increasing content of AOX in the sample the effective diffusion coefficient was decreasing.

2.2.4 Determination of the effective diffusion coefficient

Several authors have tried to propose a mathematical model for the direct oxidation kinetics of magnesia-graphite refractories and also dealt with the determination of kinetic parameters of carbon oxidation in those materials. An attempt to summarize these proposals can be found in [51]. Most of the studies concerned resin bonded bricks, the only exception being [42]. All authors neglected the chemical reaction coefficient k_c assuming that it has no or less influence on the carbon conversion and recognized diffusion coefficient as a limiting factor for oxidation. Several tests have been carried out to determine the diffusion coefficient, mostly based on the kinetic model described in Chapter 2.2.1. In Tab. 1 and Tab. 2 oxidation tests of four different authors were compared.

In the experiments of these tables, high quality magnesia with an MgO content of 97 – 99% was used. As a binder a phenolic resin was applied, the graphite content varied between 7 and 15 wt %. The samples had cylindrical shape, except in [51].

Tab. 1: Characteristics of MgO-C refractory bricks used in experiments

	Li [12]	Sadrnezhaad [30]	Faghihi-Sani [13]	Volkova [51]
Magnesia type	Sintered	Sintered	Fused (60%) Sintered (20%)	
Binder	Phenolic resin	4.8 wt% Phenolic resin	4 wt% Phenolic resin	Phenolic resin
MgO purity (wt%)	98.0	97.1	99.0	97.5
Graphite content	15 wt% (8 wt% ash)	14.3 wt% (5 wt% ash)	10 wt% (180-300nm) 10 wt% (<180nm)	7 wt% 15 wt%
Samples geometry [mm]	ϕ 44mm, 40mm length	ϕ 30mm, 25mm length	ϕ 20mm, 20mm length	20mm cube
MgO-C density [kg/m^3]	2850	ca. 2700		
Porosity [%]	12.67 % (after preoxidation)	ca. 6% after coking	12.3 % (before oxidation test)	4-5%

The oxidation experiments were performed at a temperature of 600 – 1600 °C for different durations. All samples were coked before tests at reducing atmosphere. The oxidizing agent in all cases was ambient or dry air, supplied by natural convection or gas flow. In most of the investigations, a thermo-balance apparatus was designed for the oxidation test to realize continuous measurements of the oxidation. In experiments presented in [12], CO generated by oxidation of the MgO-C refractory was further oxidized to CO_2, and the continuous quantitative analysis of the CO_2 concentration using an infrared spectrometer allowed the determination of the oxidation rate. Also the experimental set-up differed from the other oxidation tests, which is presented in Fig. 5. Details of testing procedures are given in Tab. 2.

Tab. 2: Testing procedures and parameters

	Li [12]	Sadrnezhaad [30]	Faghihi-Sani [13]	Volkova [51]
Coking in CO atmosphere	1000 °C for 10 h	600 °C for 5 h	400 °C for 3 h	No?
Pretreatment	Preoxidation at 400 °C for 50h	-	Heated at 1300°C for 3 h	no?
Furnace	tubular	tubular	furnace	Tube furnace
Temperature [°C]	1000; 1100; 1200; 1300; 1400(20h)	600; 650; 700; 800; 950; 1100; 1250	1000; 1100; 1200	800; 1000; 1200; 1400 1500; 1600
Air flow rate [l/min]	0.5	Natural convection	Air flow	3.3
Oxidizing agent	Dry air		Ambient air (?)	Dry air
Preheating/ cooling atmosphere	N_2 atmosphere	sample placed after heating up	sample placed after heating up	sample placed after heating/ Heating up in air
Exhaust gas measurement	CO, CO_2 IR-gas analyser	-	-	-
Mass loss measurement	2.5, 5, 10, 15h		continuously	5, 15, 30, 60 min
C-concentration in MgO-C	0.43 g/cm3	?	0.56 g/cm3	?

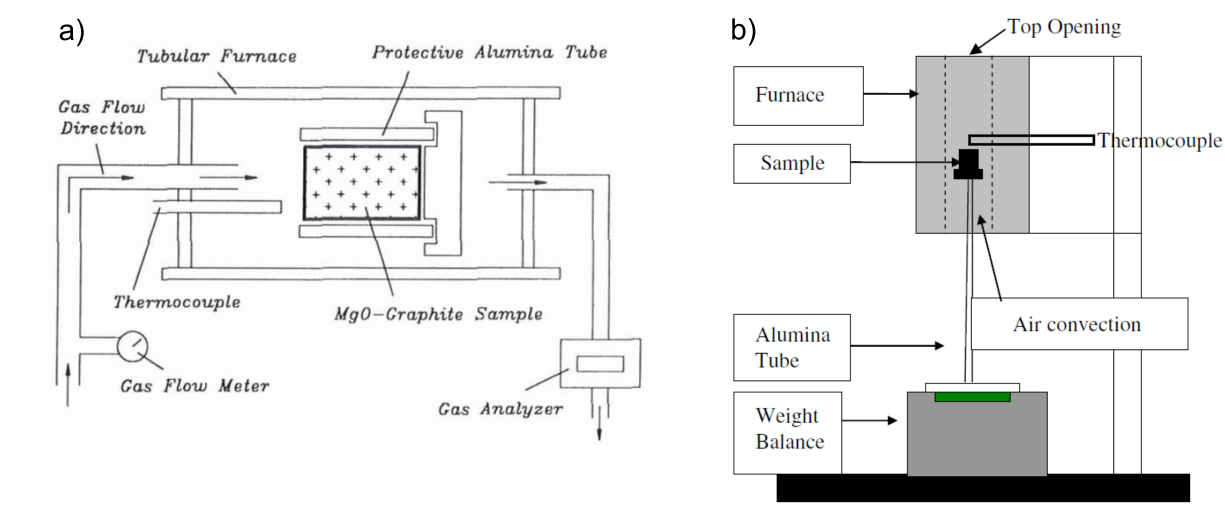

Fig. 5: Experimental set-ups applied for oxidation tests in a) Li' s experiments [12] and b) Sadrnezhaad's experiments [30]

The experimental results were presented as a weight loss or as CO_2 concentration during the oxidation time. From these results the depth of the decarbonized layer was derived and according to Eq.(17). D_{eff} and partly also k_m were determined. Fig. 6 presents diffusion coefficients determined by various authors.

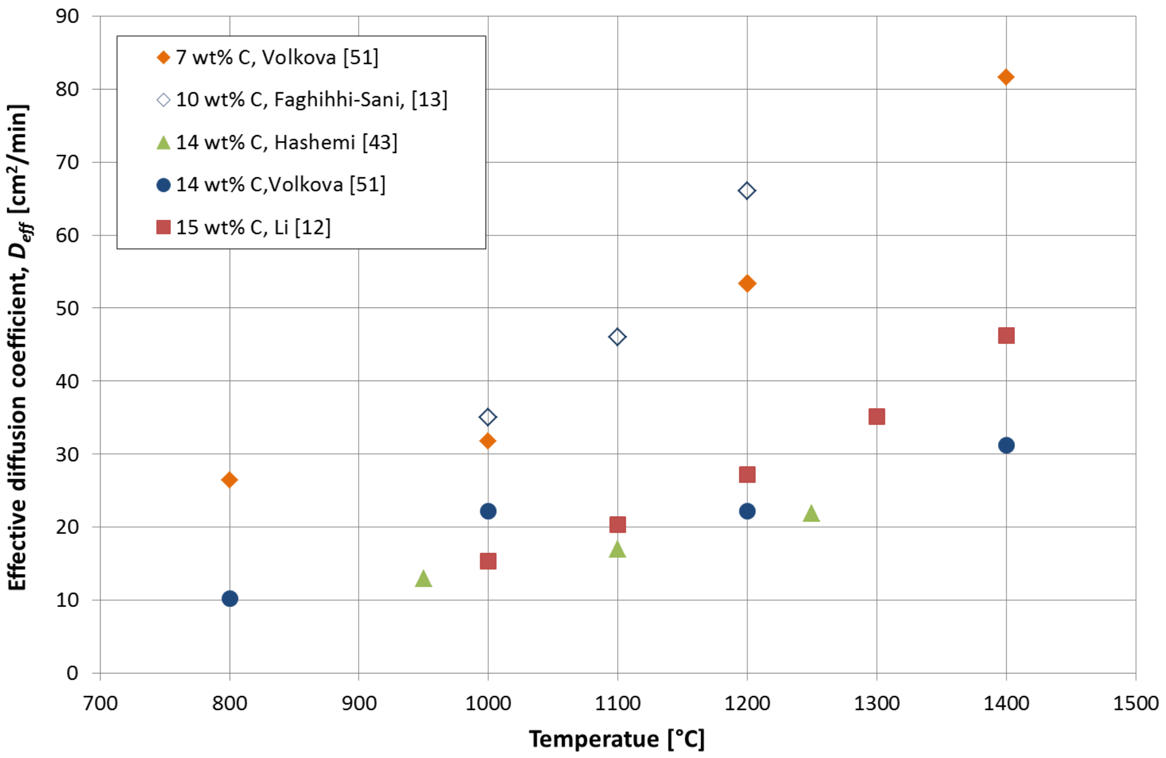

Fig. 6: Effective diffusion coefficients determined in [12], [13], [43], [51] within oxidation tests at various temperatures and graphite contents

According to the data presented in Fig. 6 D_{eff} depends strongly on the graphite content and temperature: with increase of the temperature D_{eff} also increases, whereas with increase of the graphite content it decreases. Diffusion coefficient values from different literature sources determined at same temperatures and graphite contents show good agreement. Additionally, activation energies for the diffusion mechanism through the pores have been calculated: 48.5 and 49.5 kJ/mol at 1000 – 1400 °C for Li [12] and Faghihi-Sani [29], respectively. Sunayama, omitted in above detailed compilation, determined activation energies of 36.9 and 43.3 kJ/mol for the same carbon content in the same temperature range [51]. Sadrnezhaad determined activation energies in the range of 18 - 25 kJ/ mol for pore diffusion for MgO-C at temperature range 600 – 1260 °C [30]. Activation energies given by Volkova [51] are 26 and 28 kJ/mol for refractories with graphite content of 7 wt% and 14 wt%, respectively at temperatures of 600 – 1400 °C. Ghosh [15] also determined activation energies for graphite oxidation by pore diffusion in MgO-C-material and achieved various values: 35.8, 43.4, 36 and 37.4 kJ/mol depending on carbon content, which was equal to 2.8, 4.4, 12 and 20 wt%, respectively.

2.2.5 Mass transfer coefficient

In the assumed kinetic model for carbon burnout in MgO-C refractories, the mass transfer of oxygen from the gas bulk to the refractory surface is one of the reaction limiting steps. The diffusional flux density can be described with first Fick's law as a ratio of the flux to concentration gradient:

$$j_A = -D_{AB}\frac{dc_A}{dy} \qquad (21),$$

Where j_A is molar flux of component A, D_{AB} is the binary diffusion coefficient of component A in B with the unit of [m^2/s], c_A the concentration of A and y the space coordinate. Molar flux density can equivalently be represented applying a mass transfer coefficient:

$$j_A = k_m \Delta c_A \qquad (22).$$

Here k_m is the mass transfer coefficient with the unit of [m/s]. Mass transfer coefficients depend on the physical properties of material, the flow regime (laminar or turbulent) and the geometry of the system [56].

Boundary layer theory, described by [56], is based on the concept that the mass transfer occurs within a thin film of thickness δ next to wall. Applying a difference quotient in Eq. (21) and equalizing the result with Eq. (22) yields:

$$j_A = k_m \Delta c_A = \frac{D_{AB}}{\delta} \Delta c_A \qquad (23)$$

and further

$$k_m = \frac{D_{AB}}{\delta} \qquad (24).$$

In Eq. (23) Δc_A is the difference between the species concentration on the surface and in the gas bulk. The film thickness δ depends primarily on the hydrodynamics of the system and hence on the Reynolds number and the Schmidt number [57]. Thus, various power laws relating Sherwood number (Sh), Reynolds number (Re) and Schmidt number (Sc) have been developed for different geometries:

$$Sh = \frac{k_m \cdot L_{char}}{D_G} = a \cdot \mathrm{Re}^m \cdot Sc^n \qquad (25).$$

The parameters a, m, n of Eq. (25) depend on the flow regime (laminar or turbulent) and the given geometrical conditions. Dimensionless relations for laminar and turbulent flow and the laminar-turbulent transition including external and internal forced flow for various geometries are quoted in [57], [58], [59].

An overview of diffusivity relations for gases is given in [57]. A well-known relation for binary gas mixtures at low pressure with non-polar components is the one expressed by Chapman-Eskog theory, described by Eq.(26).

$$D_{AB} = \frac{0.001858 T^{3/2} \cdot \sqrt{\frac{1}{M_A} + \frac{1}{M_B}} \cdot}{P \sigma_{AB}^2 \Omega_D} \qquad (26).$$

In Eq. (26) for diffusivity D_{AB} of two gas components A and B, T represents the Kelvin temperature, M the molar mass, P is the pressure in atm, σ_{AB} is an average collision diameter in A° and Ω_D is a temperature-dependent collision integral. Definition and calculation of σ_{AB} and Ω_D can be found in [57], [58], [59].

To calculate diffusivity of multicomponent gas mixtures at low pressure Blanc's law as described by Eq. (27) can be applied

$$D_m = \left(\sum_{j=1}^{N_C} \frac{x_j}{D_{ij}} \right)^{-1} \tag{27}$$

In Eq. (27) for the calculation of multicomponent diffusivity D_m, N_C is number of components, x_j the mole fraction of component j in the gas and D_{ij} the binary diffusion coefficient of species i and j [57], [61].

2.3 Ladle preheating

Secondary metallurgy covers the processing and treatment of molten steel after the tapping of the primary steel making furnace up to the casting. All these processes make use of steel ladles. Ladles are refractory-lined cylindrical vessels with a bottom. Fig. 7 shows a ladle used to transport molten metal in steel mills from the converter to the caster, and for treatment of the steel.

Fig. 7: Steel ladle during service: a) at the left side filled ladle will be just taken by a crane, at the right side empty ladle; b) ladle transported by a crane [62].

There are four primary reasons for preheating ladles prior to pouring molten metal into them:

- To minimize the cooling of the liquid metal. A cold ladle could cool the liquid metal enough to cause a layer to solidify on the surface.
- To minimize the thermal shock of the refractory; hot face temperature would rise from ambient conditions to that of the liquid metal (ca. 1500°C) in a few seconds.
- To remove any moisture that may have accumulated in the vessel, especially in the case castables are applied, and avoid danger of explosion
- To make the process more consistent. Without preheating, the temperature of a given ladle would vary significantly from one heat to the next [63].

The benefits of ladle preheating include lower tapping temperatures, increased ladle lining life, lower refractory maintenance costs, and increased productivity and quality in casting due to more consistent steel temperatures.

2.3.1 Technology of ladle preheating

A steel ladle is a relatively small, refractory-lined vessel that, during preheating behaves very much like a small furnace. Heat transfer by the preheater to the ladle is primarily by convection and radiation [63].

There are various possibilities of steel ladle preheating. One of the most popular is preheating with a gas burner, where the enthalpy of the gases is transformed into the heat of the combustion products. As combustion gas a natural gas is usually employed. In the steel industry very often recovered by-product gases like blast furnace gas and coke oven gas are utilized [64]. The preheating stations are usually equipped with ladle covers in order to prevent heat losses by radiation [65]. The main disadvantage of this conventional ladle preheating is its low efficiency. Several efforts have been made to improve heating efficiency, including air preheating and oxygen enrichment of the air in order to increase combustion temperature and decrease of the gas flow rate [65], [66], [67].

A typical classification distinguishes two types of burners, according to how fuel and oxidizer are mixed: premixed burners and diffusion burners. In a premixed burner, fuel and oxidizer are completely mixed before combustion begins. They produce shorter and more intense flames. For industrial heating plants usually diffusion gas burners are applied. In such burners a non-premixed combustion takes place, which means that the gas and combustion air do not mix until they have left the ports of the burner. The two fluids are kept separate within the burner itself, but the nozzle is designed in such manner that it provides mixing of the fluids as they leave. The mixing process is significantly slower than the following combustion reaction, so the principle “mixed means burnt” is valid. Diffusion burners typically have longer flames, do not have as high temperature at hot-spots as premixed burners and usually have a more uniform temperature and heat distribution [64], [68], [69]. Another type of burners are the staged burners. Secondary and sometimes tertiary injectors in the burner are used to supply a portion of the fuel or the oxidizer into the flame, downstream of the root of the flame. Staging is often done to produce longer flames, control heat transfer and reduce NO_X formation. These longer flames have typically lower peak flame temperature and more uniform heat flux distribution [69].

The majority of the industrial burners use air as the oxidizer. In many of the higher temperature heating and melting applications pure oxygen is used as oxidizer in a burner, often referred to oxy-fuel burner [70] – [73]. To increase productivity of the heating system on the one hand and not to damage the furnace or the product on the other hand a Diluted Combustion Technology, often referred to as flameless combustion, is applied. In this technology fuel and oxygen injections are separated and fuel and oxygen are mixed ‘locally’ with a burden of inert gases before they react, which results in lower flame peak temperatures, lower NO_X emissions and uniform temperature distribution in furnace [74]. The installation of diluted combustion systems for ladle preheating improves the performance with an average fuel consumption reduction by 58% [71], [73]. At a steel plant they may be large quantities of gas with low calorific value, such as coke oven gas, blast furnace gas, BOF gas. Application of oxyfuel instead of air-fuel makes the combustion of low calorific fuels attractive and comparable with air-fuel combustion [72], [75]. Another possible technology is a combination of air and oxygen, referred to as oxygen-enriched air combustion [75], [76].

A further option of ladle preheating is indirect preheating mainly utilizing radiative heat transfer. An example is the porous burner technology, where combustion takes place in a porous high temperature ceramic instead of an open flame. This results in a flameless combustion in the form of glowing ceramic foam, which can then be used as a radiating surface and acts as a homogeneous source of heat. The homogeneous heat distribution within the ladle eliminates temperature “hot spots” or “cold holes” related to airflow and associated possible lining damage. Furthermore, the preheating time and energy costs are reduced [77].

Due to the binding agents of the refractory material the preheating procedure is associated with a substantial emission of hydrocarbons, some of which are known to be highly carcinogenic. At present, in most melting facilities, the exposure of workers to these emissions can be avoided only by covering the ladle with a lid and further exhaust gas treatment. The evaporation of phenols and PAH into the ladle atmosphere is already active at lower temperatures. These molecules appear as resistant to the thermo-chemical conditions inside the ladle for most part of the temperature range of the preheating, also in the case of high oxygen content. The optimization of the combustion process and the realization of a new suction hood aim to achieve the complete oxidation of the hydrocarbons within the combustion system [65].

Fig. 8: Photographic representation of a ladle preheating station [65]

2.3.2 Simulation of ladle preheating: state of the art

Steel quality is strongly influenced by the temperature of the liquid metal entering the continuous caster, so steelmaking operations in general require a good temperature control. One of the factors influencing heat losses from molten steel is ladle thermal status. The thermal status of the ladle is determined by the refractory thermal history from previous heats and the ladle refractory configuration and wear. Several models have been developed for calculation of the transient thermal state of metallurgical ladles during the whole life cycle of the ladle [66], [78] – [85]. Many authors were interested in thermomechanical behavior of ladle linings as the stresses thereby produced can lead to failure of refractory materials [82] – [84]. For these reasons Finite Element Simulations were carried out. Others, like Volkova [66] and Fredman [80] used a simple, one-dimensional model for calculation of both stationary and transient heat conduction within the lining. Another approach to steel ladle simulation was presented in [62], [65], [78], [81], [85], where CFD calculations have been applied to predict not only ladle wall temperature distribution, but also dynamic gas flow inside the ladle during the preheating process and flow fields in both the molten steel and the gas phase, as well as the temperature distribution in the liquid metal, the gas phase and all layers in the ladle wall. Most of the authors used commercial software ANSYS Fluent, only Glaser [78] applied COMSOL Multiphysics. In the work of Glaser [78], no detailed modelling was applied for the combustion. Instead, the temperature of the outer surface of the flame was given as a boundary condition. The shape of the flame was based on photographic images of the flame, while the temperature was based on IR images. A two dimensional model has been applied to simulate the gas flow within the ladle. The domain consisted of three subdomains, namely the solid phase, the gas phase and the flame, whereupon a constant temperature of the gas-flame interface was assumed. Volkova [85] and Al-Harbi [81], who used ANSYS Fluent for CFD simulations, do not give any details about the models chosen for combustion during ladle preheating. The result achieved by Volkova [85] showed very low gas velocity near the lining and dead zones in the area near the lining of the slag zone and the lid. The surface of the inner lining is characterized by strong temperature differences. Although the bottom is overheated, the ladle lid is relatively cold. In [65], a simulation study has been done in order to optimize the gas flow in the ladle during preheating. The burner flame was simulated as a flow of air at a certain temperature and velocity. The radiation was simulated using a Discrete Transfer model, while the flow simulation applied a standard k-ε turbulence model. Achieved velocity field in the ladle was characterized by a central downward flow, which returned at the bottom and moved upwards along the lining walls. A part of the flue gas recirculates into the flame. The other part exits through the gap between cover and ladle into the surrounding area. The upper part of the ladle lining presented higher temperatures than the bottom of the ladle, probably because of higher thermal conductivity of MgO-C bricks applied in the slag bath area. Also in other studies the simulations as well as the measurements have showed that the lower part of the ladle has lower temperatures than in upper part [65], [78], [83].

Javurek [62] investigated the same voest alpine steel ladle, as it is of interest within this work, however, the preheating process was treated superficially; gas combustion was not considered and heat transfer within the lining was solved only with a specified temperature curve as the boundary condition. The focus was on the whole life cycle of the ladle with emphasis on modelling of radiative heat transfer between lining walls, molten steel and slag and the flow field of the molten steel during casting.

2.3.3 Gas combustion model

In combustion processes, fuel and oxidizer are mixed and burned. There are several combustion categories based upon whether the fuel and oxidizer is mixed first and burned later (premixed combustion) or whether combustion and mixing occur simultaneously (non-premixed combustion). It is further distinguished whether the combustion is laminar or turbulent. Because of safety considerations non-premixed flames are mostly used in industrial furnaces and burners [86].

In non-premixed flames fuel and oxidizer enter separately into the combustion chamber and the mixing of both streams takes place by convection and diffusion. Only where fuel and oxidizer are mixed on the molecular level, chemical kinetics converts them into products, with attendant release of energy. This corresponds to the maxim "mixed = burnt". Only an infinitely rapid reaction can be approximated by a fast one-step conversion of fuel and oxidizer to the products. Under the assumptions that the mass and thermal diffusivities of all species are equal (Lewis number equals unity) and that the chemicals reach equilibrium as fast as they mix, the description of the thermochemistry problem can be reduced to a single parameter: the mixture fraction ξ, defined by Eq. (28):

$$\xi = \frac{Z_i - Z_{i,ox} \cdot}{Z_{i,fuel} - Z_{i,ox}} \qquad (28),$$

where Z_i is the mass fraction of element i. The subscript ox denotes the value at the oxidizer stream inlet and the subscript fuel denotes the value at the fuel stream inlet. The mixture fraction may be understood as another expression for the local equivalence ratio [86]. Mixture fraction values are located between 0 and 1, whereby 0 means there is only oxidizer in the stream and 1 there is only fuel. At the stoichiometric mixture fraction, ξ_{stoich}, neither fuel nor does oxidizer exist, but only combustion products. If the chemical reaction has a finite rate, the linear relations are no longer valid. A schematic illustration of the linear dependence of species mass fractions w from the mixture fraction in an idealized combustion is presented in Fig. 9.

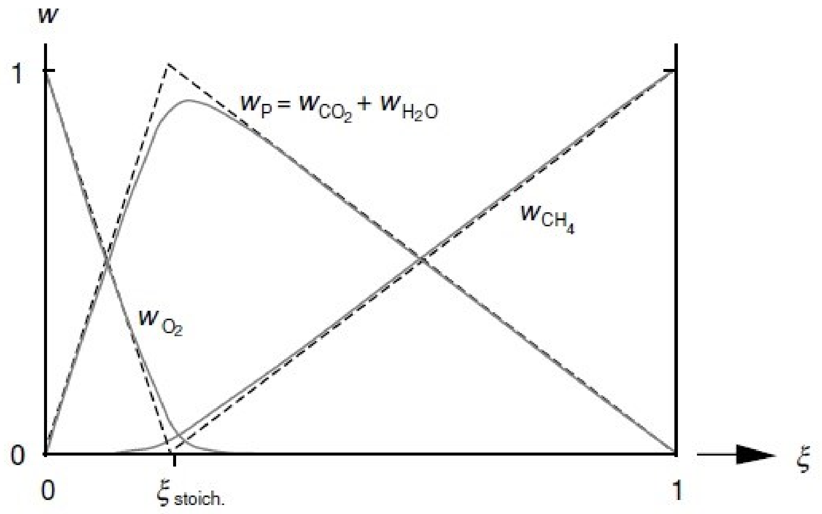

Fig. 9: Schematic illustration of the possible deviations from the linear dependence of species mass fractions w from the mixture fraction in an idealized combustion [86].

A conservation equation for the mixture fraction ξ can be derived,

$$\frac{d(\rho\xi)}{dt} + div(\rho\vec{\upsilon}\xi) -_i div(\rho D \cdot grad\xi) = 0 \qquad (29)\ [86].$$

In Eq. (29) ρ is mass density of species, $\vec{\upsilon}$ mean flow velocity of the species. It should be noted that ξ does not have a chemical source or sink term, ξ is conserved during chemical reaction and hence it is often called a conserved scalar.

All scalar variables like temperature, mass fractions, and density are functions of the mixture fraction only. Under the assumptions stated above, the turbulent non-premixed flame problem can be reduced to tracking the turbulent mixing of ξ. Fluctuations of the mixture fraction are taken into account by introducing a presumed probability density function (PDF), which can be thought of as the fraction of time that the fluid spends in the vicinity of the state ξ, as presented by Eq. (30)

$$p(\xi)\Delta\xi = \lim_{t \to \infty} \frac{1 \cdot}{t} \sum_i \tau_i \qquad (30).$$

In Eq. (30) τ_i is the duration ξ stays in the interval $\Delta\xi$ and t the length of the time interval for sampling the τ_i. The shape of the function $p(\xi)$ depends on the nature of the turbulent fluctuations of ξ. In practice, $p(\xi)$ is unknown and modeled as a mathematical function that approximates actual PDF shapes that have been observed experimentally [86], [87]. The illustration of Eq. (30) can be found in Fig. 10.

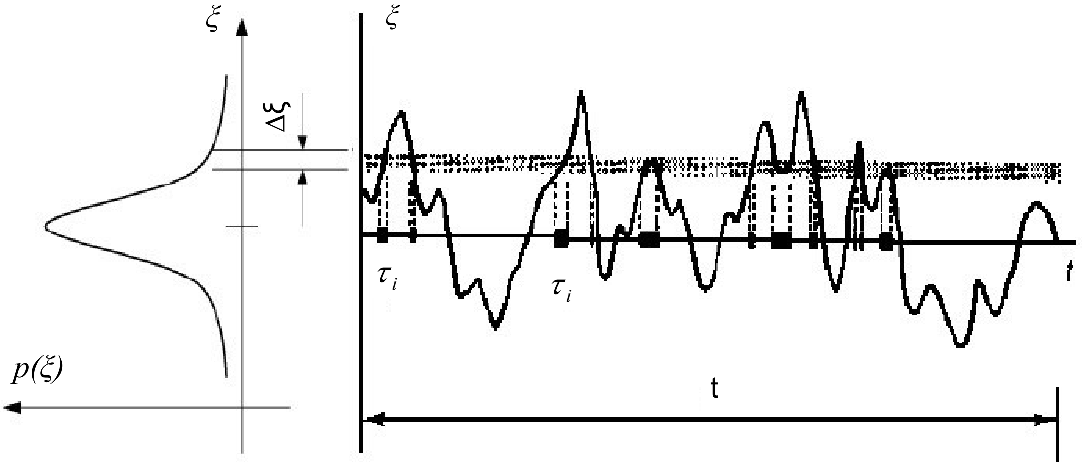

Fig. 10: Graphical representation of the Probability Density Function *p(ξ)* [87].

If the PDF of the mixture fraction is known, the mean values of the scalars, depending on ξ, can be calculated. Density-weighted mean species mass fractions and temperature can be computed by Eq. (31),

$$\overline{\phi_i} = \int_0^1 p(\xi)\phi_1(\xi)d\xi \qquad (31),$$

for a single-mixture-fraction system. The chemical composition can then be modeled as being in chemical equilibrium or considering the impact of the flow field onto chemical equilibrium using steady laminar flamelet model. The steady laminar flamelet model described by Peters [88], [89] views the turbulent flame as an ensemble of laminar, locally one-dimensional flamelet structures embedded within the turbulent flow field. A common laminar flame used to represent a flamelet is the counterflow diffusion flame, which consists of opposed, axisymmetric fuel and oxidizer jets.

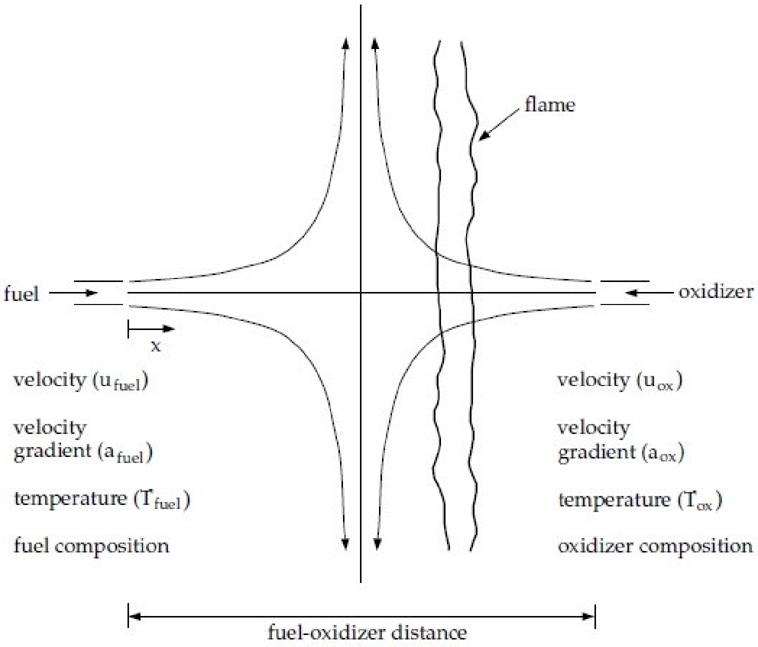

Fig. 11: Schematic illustration of the flamelet concept [87].

As the distance between the jets decreases or the velocity of the jets increases, the flame is strained and it can eventually extinguish. Species mass fraction and temperature can be uniquely described by two parameters: the mixture fraction and the scalar dissipation [87]. This reduction of the complex chemistry to two variables allows the flamelet calculations to be preprocessed, and stored in look-up tables. By preprocessing the chemistry, computational costs are reduced considerably [87], [90] – [92].

For the description of the combustion kinetics and the species transport a 41-reaction mechanism for methane combustion proposed by Correa [93] was used consisting of the following 16 species: N_2, O_2, CH_4, H_2, CO, CO_2, H_2O, OH, H, O, CH_3, HCO, HO_2, H_2O_2, CH_2O and CH_3O. Prior CFD studies presented in [94], [95] revealed the suitability of the Correa mechanism for the combustion gas mixtures of interest in the current study.

2.3.4 Heat transfer during steel ladle preheating

The heat released during the combustion is transferred to the lining walls by convection and radiation. Therefore, a non-adiabatic simulation approach should be chosen for solving the energy transport equation.

The convective heat transfer at the wall surfaces is solved using a wall function according to the law of the wall theory [96]. Wall functions are semi-empirical formulas used to bridge the viscosity-affected region between the wall and the fully-turbulent region and thus eliminate the necessity to modify the turbulence models to account for the presence of the wall [87].

The radiative heat is released by a transparent combustion flame, representing an optically thin medium with no scattering. Under this assumption, the radiative heat exchange dominates transfer directly between the walls. The modelling of thermal radiation is a complex area and various models were proposed while trying to meet three major aspects – a good computational economy, a relatively simple mathematical description and the applicability in arbitrary complex geometries [87]. These requirements can be fulfilled by the Discrete Ordinates (DO) radiation model, which spans the entire range of optical thicknesses and is commonly applied for simulation of methane combustion [87].

The absorption coefficient can be defined with the help of weighted-sum-of-gray-gases model (WSGGM), as a composition depending function. It is a reasonable compromise between the oversimplified gray gas model and a complete model that takes into account particular absorption bands [87], [97].

2.3.5 Simulation of gas flow in the ladle

Despite of the unsteady operating conditions during the steel ladle a quasi-steady reference state was assumed for the flow, described by the Reynolds-averaged Navier-Stokes (RANS) equations [86], [98]. Gas turbulence was modelled by the realizable k-ε turbulence model. According to [87] this choice is fully justified for the high Reynolds numbers for the burner jet flow in the ladle interior.

3 Validation of the kinetic model

The kinetic model for the carbon burnout in MgO-C refractory was presented in Section 2.2.1. Throughout the current Chapter, the determination of the effective diffusion coefficient of various refractory materials will be described and the kinetic model evaluated by laboratory experiments.

3.1 Tested refractory materials

The investigation of the MgO-C materials comprised of four different types M1-M4. The differences between various refractories were among others in the binder, carbon content, type of magnesia raw material and porosity. Material M1 contained metallic aluminum and silicon as antioxidants (3% wt). Properties of investigated materials are presented in Tab. 3.

Tab. 3: Properties of tested MgO-C refractories

MgO-C sample	Bond type	Density [kg/m3]	Porosity [%]	Carbon content [% wt]	Graphite content [% wt]
M1	Resin bonded	3070	1,77	11.0	9.0
M2	Resin bonded	3050	2,97	10.5	9.0
M3	Pitch bonded	3000	4,54	12.5	9.4
M4	Pitch bonded	2790	5,63	16.0	Not known

Resin bonded MgO-C bricks M1 and M2 were hardened at 180 °C for 6 h, while the pitch bonded bricks M3 were tempered at 280 °C also for 6 h. M4 bricks were not tempered.

3.2 Effective diffusivity in various MgO-C bricks

Effective diffusion coefficients for oxygen diffusion in the porosity of the refractory material were determined for the materials defined in Tab. 1 by thermogravimetric analysis (TGA), following the procedure presented in [29] and [30]. The furnace was heated up to a certain temperature and afterwards a specimen was placed inside. Samples had cylindrical shape with a height of 100 mm and a diameter of 35 mm. Air support was guaranteed by natural convection. Mass changes were automatically recorded every second during the whole experiment. The tests were carried out until mass remained constant. TGA was run at four temperatures: 700, 900, 1000 and 1100 °C. For every temperature, two tests were performed to assure reproducibility. All experiments were carried out at the German Institute for Refractories and Ceramics (DIFK - Deutsches Institut für Feuerfest und Keramik).

Fig. 12 depicts the results of the TGAs at 1000 °C as mass loss of the sample vs. time. The presented mass loss curves of material M1 include the mass change caused by antioxidants oxidation. The experiments show consistent reproducibility, as the curves for a certain brick and a certain temperature are nearly the same. Only in case of M4 an aberration smaller than 1% can be noticed.

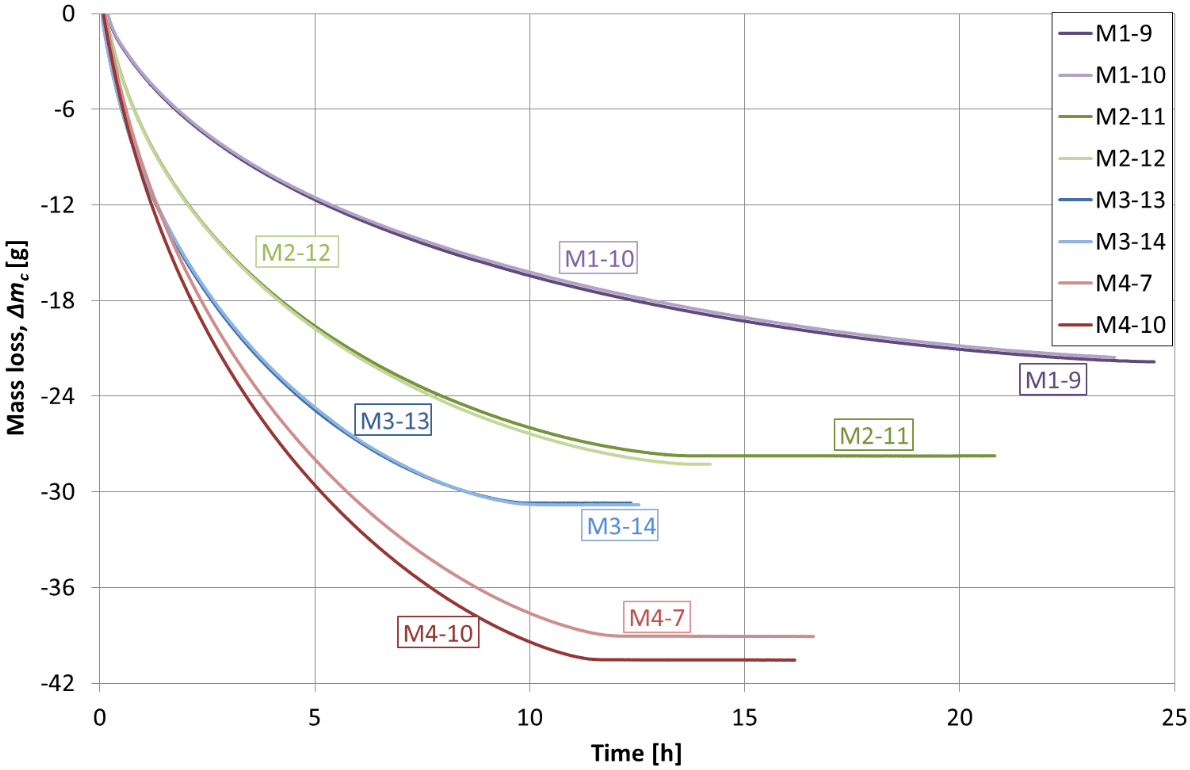

Fig. 12: Mass loss of various MgO-C bricks at 1000 °C.

MgO-C bricks with antioxidants (M1) show the lowest mass loss among the tested samples. The resin bonded bricks (M2) have lower mass loss than the pitch bonded bricks. The curves of pitch bonded bricks (M3 and M4) have nearly coincide within the first two hours, but afterwards the curve of refractory material M4 decreases faster. Test results from Fig. 12 can be also presented as a relation between the radius of unoxidized cross-section (r_t) and time.

The mass fraction of unoxidized graphite (X_m) in the sample is defined in Eq. (32):

$$X_m = \frac{x_C \cdot m_{C_0} + \Delta m_C}{x_C \cdot m_{C_0}} \qquad (32).$$

Here x_C is the mass fraction of graphite in the sample; m_{C_0} the initial mass of sample; Δm_C is the mass loss at the time t calculated as a negative quantity. The mass fraction of unoxidized graphite equals the following unoxidized specimen volume fraction X_V defined in Eq. (33):

$$X_V = \frac{\pi \cdot r_t^2 \cdot l_0}{\pi \cdot r_0^2 \cdot l_0} = \frac{r_t^2}{r_0^2} \qquad (33).$$

Here r_0 is the initial radius of the specimen and r_t the actual radius, computable with Eq. (34):

$$r_t = r_0 \sqrt{\frac{x_C \cdot m_{C_0} + \Delta m_C}{x_C \cdot m_{C_0}}} \qquad (34).$$

Fig. 13 shows the radius of the unoxidized cylinder cross-section as a function of time for refractory M3 at various temperatures. The radius change curves at 800, 900, 1000 °C have similar shape and the samples were fully oxidized after 8-12 h. The curve shape at 700 °C differs from those at higher temperatures and the end of oxidation occurs after 40 h.

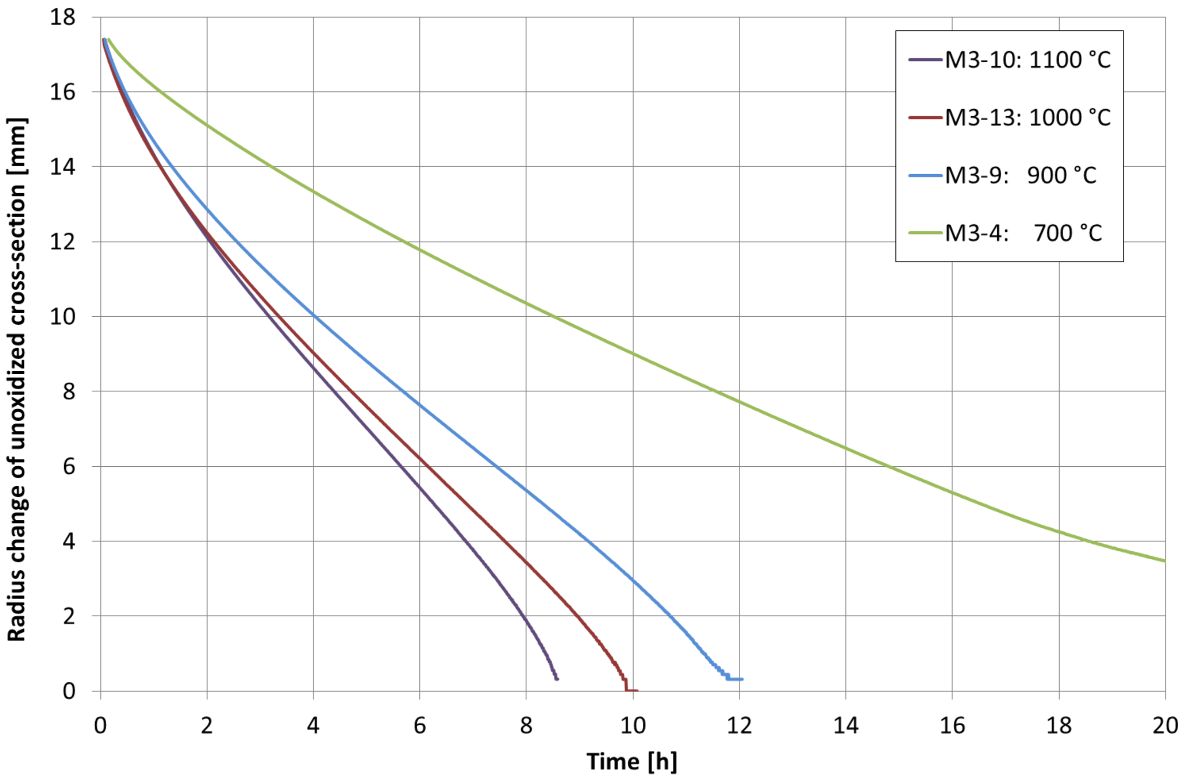

Fig. 13: Radius of unoxidized cylinder cross-section for refractory material M3 at various temperatures

The radius change of sample's unoxidized cylinder cross-section as a function of time is expected to follow the typical form of Eq. (17), presented as in Eq. (35):

$$t = a \cdot r_t^2 \cdot \ln r_t + b \cdot r_t^2 + c \cdot r_t + d \qquad (35).$$

Implementation of a non-linear regression method to evaluate the data shown in Fig. 13 serves to estimate the parameters a, b, c and d in Eq. (35) and consequently the kinetic parameters mentioned in Eq. (14). Curve fitting agrees with the experimental data (see Fig.A. 2 - Fig.A. 12), with the only exception being the temperature of 700 °C.

The effective diffusion coefficient can then be calculated from the parameter *a* according to Eq. (35):

$$D_{eff} = \frac{\rho_{M,C}}{4 \cdot a \cdot C_b^{(O_2)}} \qquad (36).$$

The calculated parameter a of Eq. (35) as well as D_{eff} from Eq. (36), at various temperatures and for different refractory materials are listed in Tab. 4.

Tab. 4: Values of parameter a in Eq. (35) and effective diffusion coefficients for various refractory materials at different temperatures determined with help of TGA

Refractory material	**M1**	**M2**	**M3**	**M4**
Temperatur [°C]	Coefficient a [min/cm^2]			
1100	680.07	306.66	216.09	222.57
1000	608.70	317.85	216.60	270.15
900	567.90	404.85	281.52	305.37
Temperatur [°C]	Effective diffusion coefficient, D_{eff} [cm^2/min]			
1100	5.09	10.77	16.45	20.95
1000	5.31	9.65	15.68	16.19
900	5.31	6.76	10.60	13.38

The determined diffusion coefficients depend on the temperature for materials M2-M4. In the case of refractory M1 the calculated coefficients exhibit the lowest value of approximately 5 cm^2/min, which does not change with the temperature. Pitch bonded bricks (M3 and M4) show higher effective diffusivities than resin bonded brick M2. Material M4 with the highest carbon content of 16 % wt achieved also the highest diffusivity values: 21 cm^2/min at 1373 °C and 16 cm^2/min at 1000 °C. The values of D_{eff} for M3 at 1000 °C is 15,68 cm^2/min and for M2 9.65 cm^2/min. The determined values of effective diffusion coefficients of materials M2-M4 are quite similar to those reported in [12] and about the half of those reported in [13].

The obtained diffusion parameters were expected to show an Arrhenius type relation with temperature. Fig. 14 presents this dependence for the tested materials. Additionally, the value of the activation energy can be calculated by implementing a linear regression. The obtained activation energies for M2-M4 are the half of the energies calculated in [12] and [13]. Refractory material M1 was not considered in Fig. 14, since it showed no dependence on the temperature. Pre-exponential factors and activation energies of effective diffusion in MgO-C refractories for various material types are presented in Appendix (see Fig.A. 13)

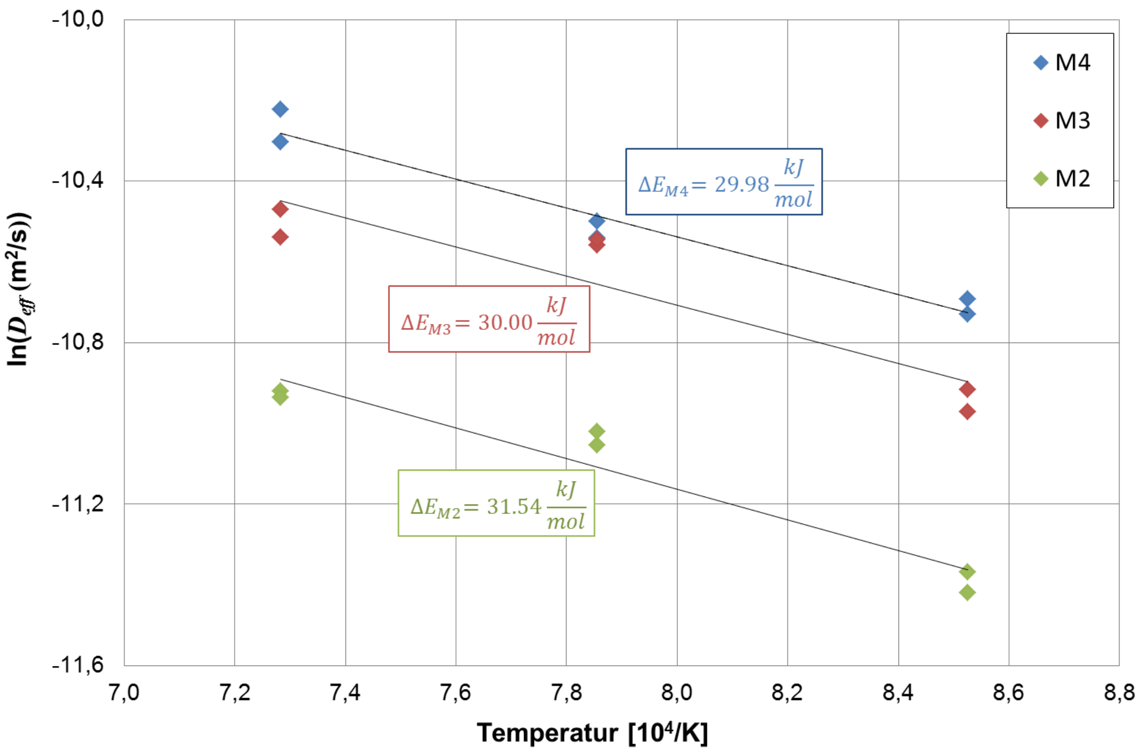

Fig. 14: Arrhenius plot of the effective diffusivity for various MgO-C refractory materials

Fig. 15 illustrates the change of the oxidation front depending on temperature. The samples were removed from the furnace after losing 12 % (Fig. 15a) and 9 % (Fig. 15b) of their initial mass. At 1000 °C (Fig. 15a) the oxidation front is easily recognizable and seems to be homogeneous: the depth of decarbonized layer is the same for whole sample perimeter. At 700 °C (Fig. 15b), the reaction front is impossible to recognize. This phenomenon corresponds with data shown in Fig. 13 where it was not possible to determine the diffusion coefficient for this temperature according to the radius change during the test.

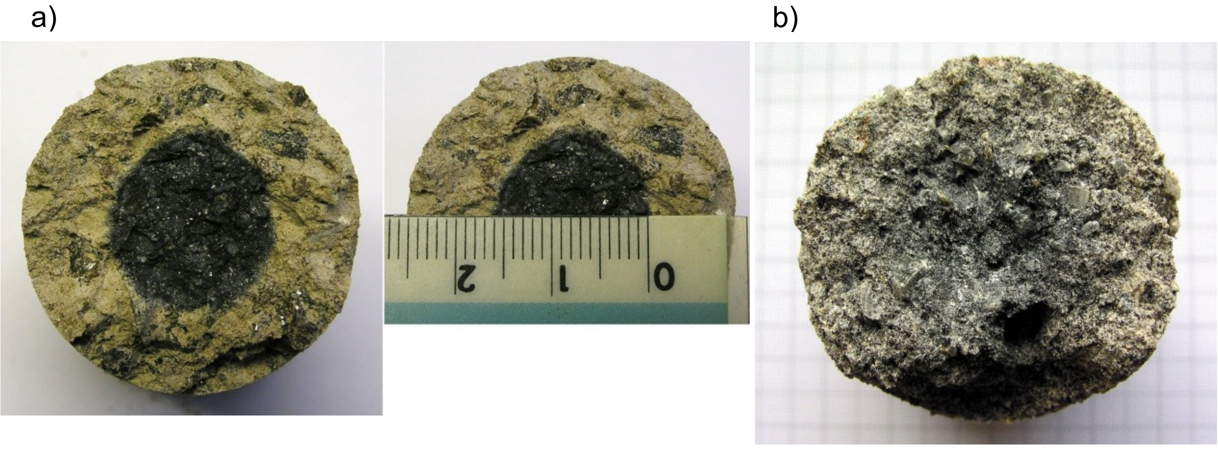

Fig. 15: Cross section of MgO-C samples after (a) 12 % mass loss at temperature of 1000 °C and (b) and 9 % mass loss at 700 °C

Similar results were achieved in research and presented in [30] and [99]. At lower temperatures of 600 °C, 650 °C and 700 °C no recognizable boundary was observed at the cross sectional areas of the samples. At temperatures higher than 800 °C, a sharp boundary was developed. According to own gathered data and to that presented in [30], a change in the oxidation kinetics around 800 °C should be expected. In [30] it is explained with a possible Boudouard reaction within the pore volume, since at temperatures lower than 800 °C, soot is formed according to Eq. (3) and thus causes pore-end blockage. However, considering the kinetics of graphite oxidation described in Section 2.2.2, an alternative explanation could be that the carbon burnout in MgO-C refractory at that temperature is determined by a chemical reaction controlling step and not by diffusion (see 2.2.1).

3.3 Mass transfer at ladle walls

Mass flux of reacting carbon has three resistances as proposed in Eq. (12): mass transfer, pore diffusion and chemical reaction. In Section 3.2 the determination of effective diffusion coefficient D_{eff} within various MgO-C refractory materials was already presented. The chemical parameter k_c was discussed in Section 2.2.2. The mass transfer coefficient k_m depends on several factors, such as flow regime or geometry of the body. For the prediction of carbon burnout model k_m may be calculated by a dimensionless relation alike that presented in Eq. (25). The information necessary for the calculation of the Reynolds and Schmidt numbers like gas velocity and temperature can be achieved from CFD simulation data. To verify the mass transfer coefficients calculated in this manner experiments in a tube furnace were carried out. Within the oxidation experiments, graphite samples were tested to eliminate the factor of diffusion within the MgO-C refractory material and to concentrate only on the mass transfer of oxygen from the gas bulk at the refractory surface.

The oxidation experiments to determine mass transfer coefficient were run in a tube furnace. The experimental setup is presented in Fig. 16. The samples were placed inside a corundum tube which was heated by an electrical furnace. Temperature was measured inside the electrical furnace, but not inside the tube. Gas was supplied by a pressure cylinder. The flow rate was regulated according to flowmeter measurements. Such a meter was located before the gas inflow. After leaving the tube furnace, the gas passed through a gas analyzer, where CO, CO_2 and H_2O contents were measured. The setup inside the tube was prepared as shown in Fig. 16 and Fig. 17, so that only one plane contact surface parallel with the gas flow was accessible for the oxygen. A ceramic lattice was placed inside the tube to regulate and homogenize the gas flow over the sample.

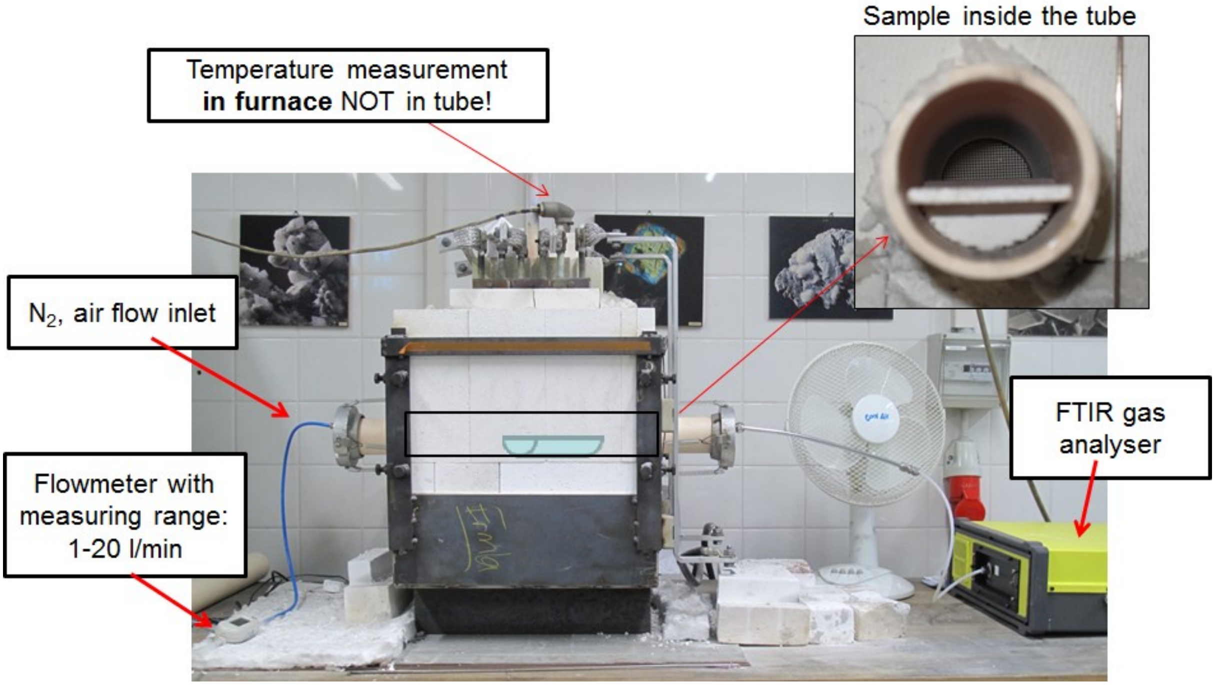

Fig. 16: Experimental setup for the graphite oxidation tests, carried out in a tube furnace. A schematic view of corundum tube is presented with the sample placed inside

Fig. 17 illustrates the experimental setup inside the tube. The heated part of the tube inside the furnace was 24 cm long. The fireclay furnace insulation was 10 cm thick, and the protruding parts of the tube were 13.5 and 13 cm long. The lattice was placed 17 cm behind the gas inlet. The graphite bars were placed at the end of corundum half-cylinder. The graphite bars were 15x15x55 mm, with a weight of about 20 g. In the experiments, two of them were placed together. The shape of the bars was adjusted by polishing, as to fit them into the tube. Behind the graphite sample placed in corundum, a corundum body has been inserted to assure only one contact surface between gas and graphite.

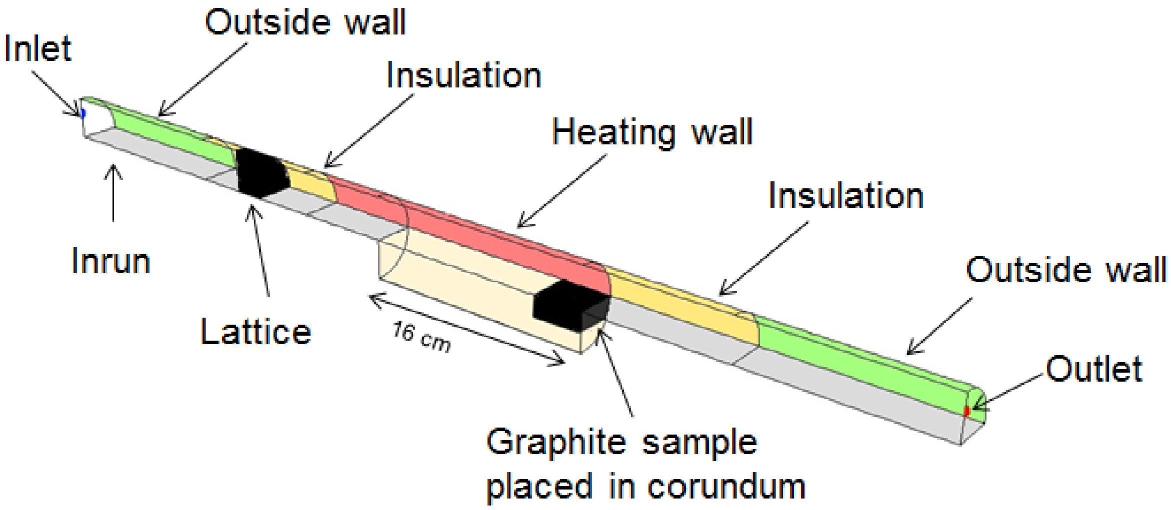

Fig. 17: Illustration of the experimental setup inside the tube for graphite oxidation tests

The samples were heated up in the furnace to a predefined temperature under nitrogen atmosphere. After having reached the final temperature, synthetic air (Linde Gas GmbH) was purged through the tube with a given flow rate for about 60 min. The amounts of CO_2, CO and H_2O were measured in off-gas with a portable gas analyzer (Gasmet™ DX4000 Fourier Transform Infrared Spectroscopy (FTIR)). The registered spectrums were evaluated by the software Calcmet, which displays compounds concentrations in volume percent. Cooling was carried out again under nitrogen atmosphere. The height and weight of the samples was measured before and after experiment. The flow rate of the purged air was measured before its entrance into the tube with a flowmeter (Low Flow Model 4140, Driesen + Kern GmbH) and was registered during the whole experiment.

Fig. 18 presents mass fluxes densities of oxidized graphite during the experiments at various flow rates. The oxidation rate of graphite increases with the increasing dry air flow rate. At higher flow rates, a maximum is reached within the first few minutes of the experiment. Afterwards the curves tend to fall down slightly. This tendency is not observed at the lower flow rates of 1.8 l/min and 2.7 l/ min. This fact could be explained with burnout progression: faster oxidation at higher flow rates leads to graphite geometry change, which, in turn, influences oxygen mass transfer from the bulk at the sample’s surface and further the mass flux of reacted carbon.

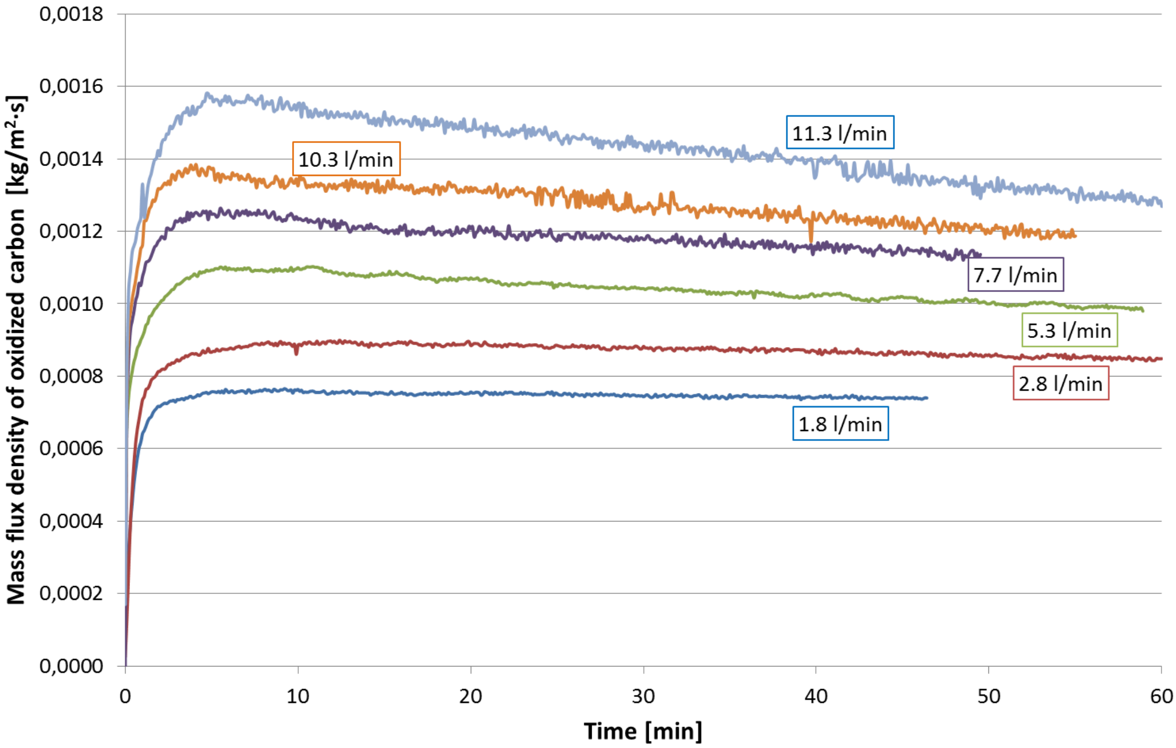

Fig. 18: Mass flux densities of oxidized graphite at various air flow rates and a temperature of 1000 °C

In Fig. 19, graphite samples after experiments at 1000 °C and a flow rate of 2.7 l/min and 11.7 Nl/min are compared. The red arrows show the flow direction of the dry air. At flow rate 11.7 Nl/min, the oxidized depth changes along the sample from 4 mm at the left side to about 2 mm at the right one. The oxidized depth for 2.7 l/min varies less, the difference between the reacted graphite height at the begin and end of the sample is less than 0.5 mm. Graphite geometry changes confirm their influence on the mass transfer coefficient and, further, on the oxidation rate. For the case of Fig. 19b, a larger part of the specimen becomes situated in a dead zone of the air flow after oxidation progressed.

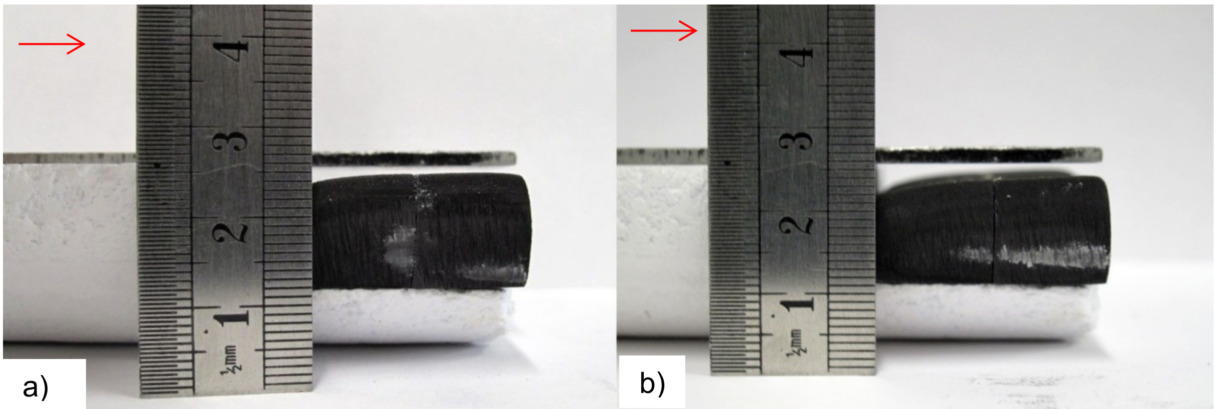

Fig. 19: Photographical documentation of graphite samples after oxidation experiments at 1000 °C and at flow rate of a) 2.7 l/min and b) 11.7 l/min

Simultaneously with the experimental work, a CFD simulation was developed to gather information on gas temperature and flow within the tube. For the flow simulation, a realizable k-ε turbulence model was used. Radiative heat transfer was calculated with a discrete ordinate model and the convective heat transfer at the gas-solid interface was determined with a standard wall function (see Section 2.2.4). Boundary conditions were set with a predefined temperature along the tube and the sample of 1000 °C. The velocity of the entering gas stream varied depending on the applied flow rate, the temperature was set at 25 °C. The generated mesh consisted of 1883499 cells, both hexahedral and tetrahedral. The simulation was run as a stationary solution to the model equations.

Fig. 20 depicts a typical simulation result for a flow rate of 10.3 l/min. Two velocity profiles colored with temperature values are shown above the graphite sample. On the one hand, the temperature of the gas rises across the tube; while, on the other hand, purged air decreases slightly the temperature field of the sample.

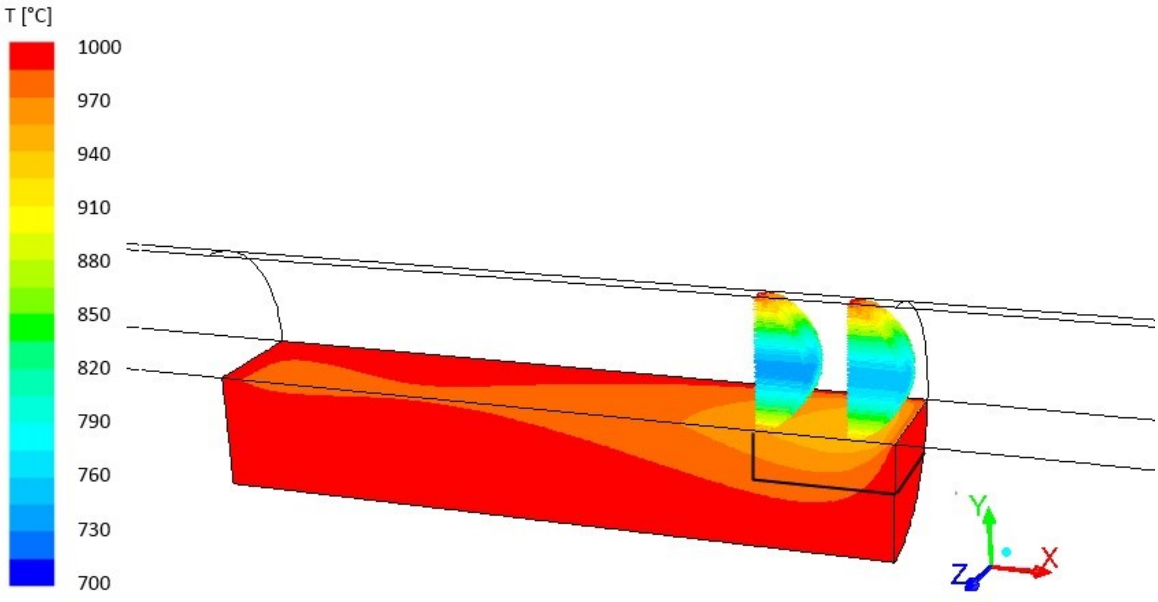

Fig. 20: CFD simulation of process conditions during an oxidation test. Calculated sample temperature field and gas velocity vectors over the graphite sample colored with temperature values at air flow rate of 10.3 Nl/min

The simulation data provide information about the flow characteristics. In Fig. 21, velocity profiles in the tube furnace over the graphite sample are presented. Continuous lines present profiles at the beginning of the graphite sample, the dashed line profiles in the middle of its length. Profiles for one flow rate differ slightly only at higher flow rates, what indicates that the flows are aerodynamically developed. The parabolic shape of the profiles indicates a laminar flow through the tube, which is also confirmed by the calculated Reynolds number, being equal to 145 for the highest flow rate.

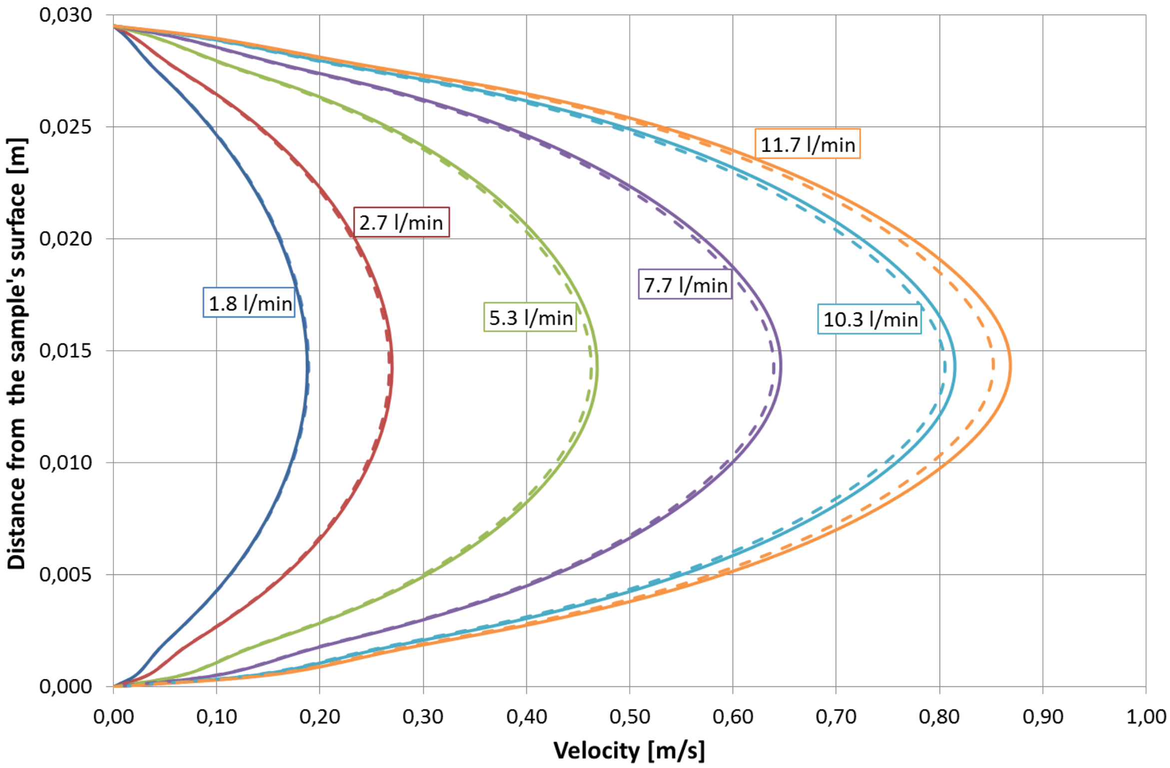

Fig. 21: Velocity profiles in the tube furnace over the graphite sample. The continuous line represents the profile at the beginning of the graphite sample, while the dashed line profile is valid for the middle of its length

Fig. 22 presents the temperature profiles over the samples. In this case, the profiles differ significantly along the tube length. Gas temperatures increase with length, so the flow is still not thermally developed. Moreover, the cooling effect of the sample is visible: the temperature of the sample surface decreases along the tube. According to the ideal gas equation, the molar concentration of gas is inversely proportional to the temperature and reflects the heat flow development.

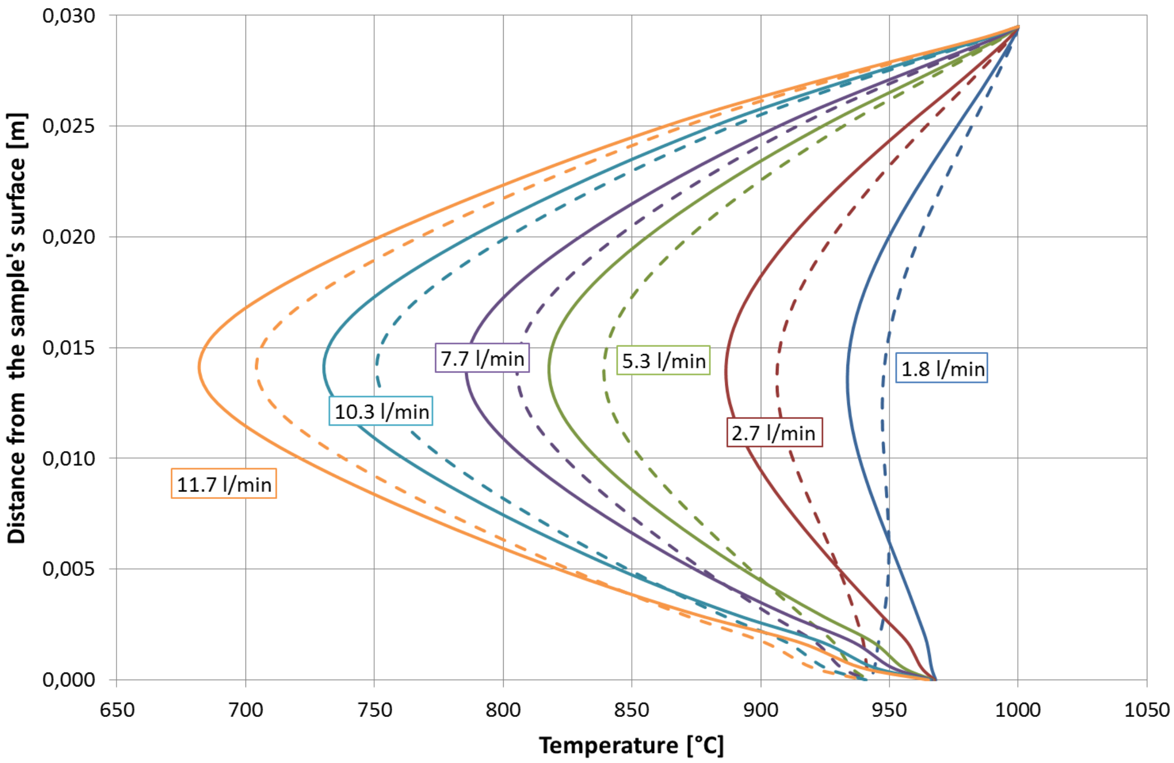

Fig. 22: Temperature profiles in tube furnace over the graphite sample. The continuous line represents the profile at the beginning of the graphite sample, while the dashed line profile is valid for the middle of its length

To calculate the local mass transfer coefficients from CFD simulation data, the power law approach (25) was applied, according to [58]. The local Sherwood number was defined as a relation of dimensionless variables for a thermal and hydrodynamic entry flow in a tube according to [58]

$$Sh_{x,T} = \left[Sh^3_{x,T,1} + 0.7^3 + \left(Sh_{x,T,2} - 0.7\right)^3 + Sh^3_{x,T,3}\right]^{1/3} \quad (37),$$

where $Sh_{x,T,1}$ is

$$Sh_{x,T,1} = 3.66 \quad (38),$$

$Sh_{x,T,22}$ is

$$Sh_{x,T,2} = 1.077\left(\mathrm{Re}\, Sc \frac{d_i}{x}\right)^{1/3} \quad (39),$$

and $Sh_{x,T,3}$ is

$$Sh_{x,T,3} = 0.5\left(\frac{2}{1+22Sc}\right)^{1/6}\left(\mathrm{Re}\, Sc \frac{d_i}{x}\right)^{1/2} \quad (40).$$

Index x gives the information of inrun length of the flow. In the graphite oxidation experiments; it was the distance between the flow correction lattice to the beginning or the middle of the sample and was equal to 23 or 26 cm.

As a characteristic length d_i a hydraulic diameter $d_{i,h}$ as defined by Eq. (41) was used:

$$d_{i,h} = \frac{4 \cdot A}{P} \tag{41}$$

In Eq. (41) A is a cross sectional area and P a wetted perimeter of a cross-section. The diffusion coefficient of oxygen in the gas bulk applied in Eq. (25) was calculated with Eq. (26). The necessary parameters for Eq. (26) were taken from [61]. Mass transfer coefficients were calculated for two positions of the graphite sample, at its beginning and in the middle of its length, and then averaged. A calculation is presented in the appendix (see Fig.A. 18).

The values calculated from the simulation data were compared with experimental mass transfer coefficients. Based on Eq. (19) and assuming no diffusion within the graphite material and spontaneous graphite reaction immediately after oxygen is adsorbed at the graphite surface, the coefficient k_m is determined with Eq. (42):

$$k_m = \frac{\dot{j}_R^C}{2 \cdot C_b^{O_2}} \tag{42}$$

Oxygen concentration $C_b^{O_2}$ was calculated with the ideal gas law, according to the temperature distribution achieved within the simulation. The reaction rate coefficient k_c was omitted in Eq. (42), as all the tests were carried out at 1000 °C, where the chemical reaction does not influence the graphite conversion.

Fig. 23 presents the comparison between the mass transfer coefficients determined within experiments and those calculated from simulation data. Experimental coefficients were calculated in two manners: by using the average graphite oxidation rate from the experiment and by applying the maximal value registered during the test (see Fig. 18).

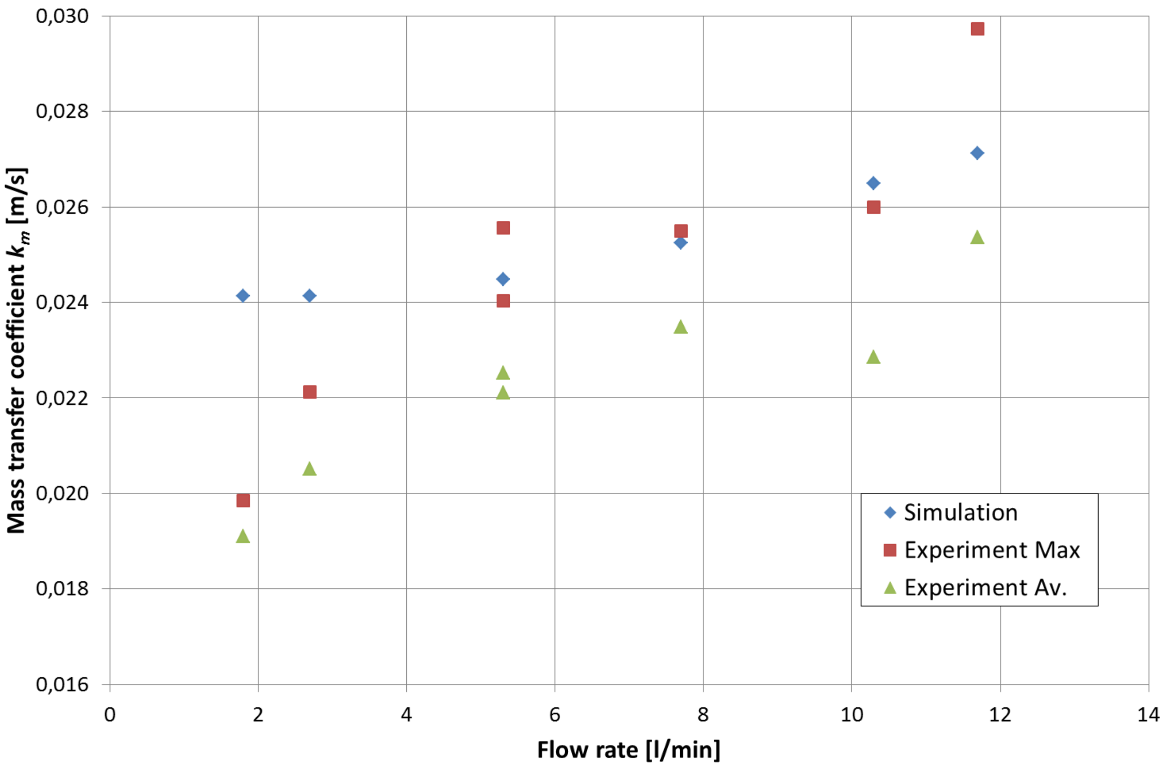

Fig. 23: Mass transfer coefficients determined within the graphite oxidation experiments and calculated from CFD simulation data

The simulated and experimentally determined values are in the same order of magnitude and show agreement at flow rates equal or higher than 5.3 Nl/min. The difference of 10 – 20 % can be seen at the flow rates of 2.7 and 1.8 l/min.

3.4 Experimental evaluation of the carbon burnout kinetic model

To evaluate the kinetic model of carbon burnout in MgO-C refractory bricks a series of experiments were carried out in a tube furnace. The results of the experiments were presented as carbon burnout curves, where the depth of the decarburized MgO-C layer was plotted against time. Simultaneously, the oxidation depth was calculated according to proposed kinetic model.

The experimental setup was the same as that one used for the graphite oxidation tests (see Fig. 16). The tested material was a pitch bonded MgO-C refractory with 12 wt% carbon content (material M3). The setup inside the tube was similar to that presented in Fig. 17 and the shape of the samples was a half-cylinder with 55 mm diameter and 8 cm length. The sample was placed inside the tube behind a corundum body as shown in Fig. 24. Behind the MgO-C sample, a corundum body has been inserted to assure only one contact surface between gas and graphite.

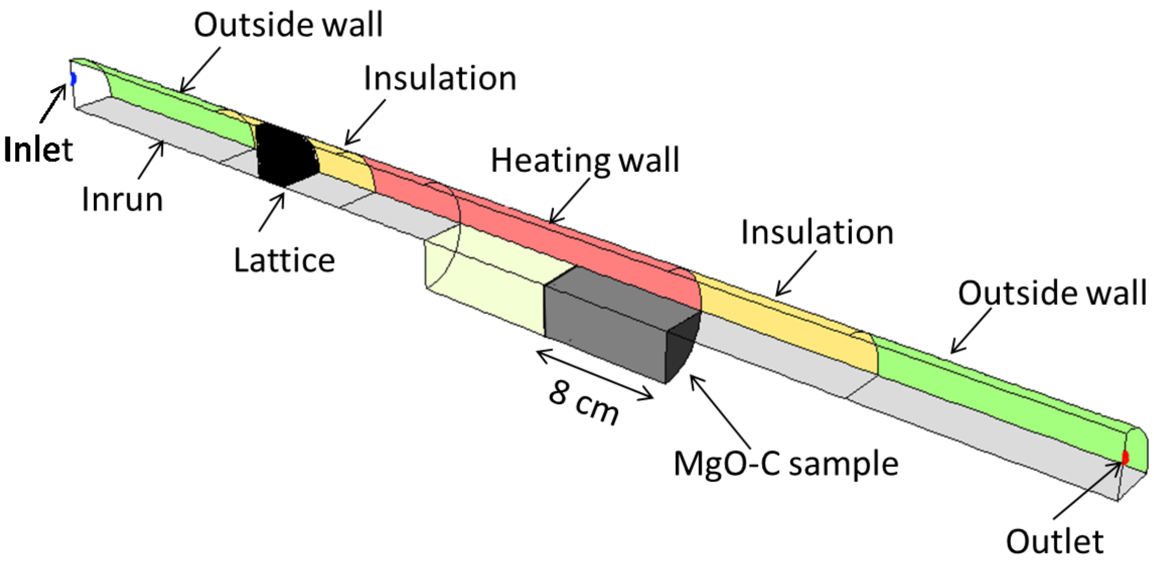

Fig. 24: Illustration of the experimental setup inside the tube for MgO-C refractory material oxidation tests

All of the samples were coked before the oxidation tests in carbon monoxide atmosphere to remove volatile components. Afterwards, the samples were placed in the tube furnace, heated up under inert atmosphere to a preset temperature and then synthetic air was purged through the tube with a predefined flow rate for about 90 min. The carbon monoxide and carbon dioxide contents in the exhaust gas were measured during the experiment. The mass of the samples was measured before and after the test. Samples have been documented photographically, an example being shown in Fig. 25. The oxidation front at 1000 °C was sharp and clearly visible. The depth of the decarburized layer was measured according to the color change of the sample and calculated from the reacted carbon mass which was determined form the gas analysis.

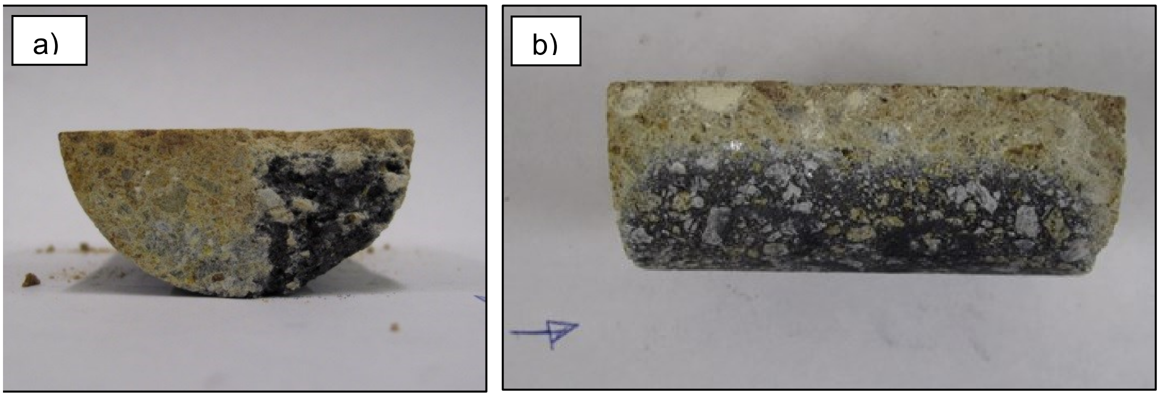

Fig. 25: MgO-C refractory sample of material M3 after oxidation test at 1000 °C with a) sample's front view with a partly scratched material at the right side of the sample and b) sample's side view. The marked arrow points the air flow direction

One of the goals of the experimental work was to study the influence of temperature on the carbon burnout. The refractory material was tested at: 600°C, 700 °C, 800 °C, 900 °C and compared with experiments run at 1000 °C. The photographical documentation of the samples after the oxidation tests is presented in Fig. 26. At 600 °C, the MgO-C refractory material did not change its initial black color; however, it showed partial material disintegration. At 700 °C, there was a slight change of color and the material was more disintegrated. At 800 °C the change of color was more apparent, but there was still no clear diffusion front noticeable. At 900 °C, the oxidized material showed a bright color, the material was disintegrated. The oxidation front was sharp and clearly visible and the sample looks similar to samples tested at 1000 °C.

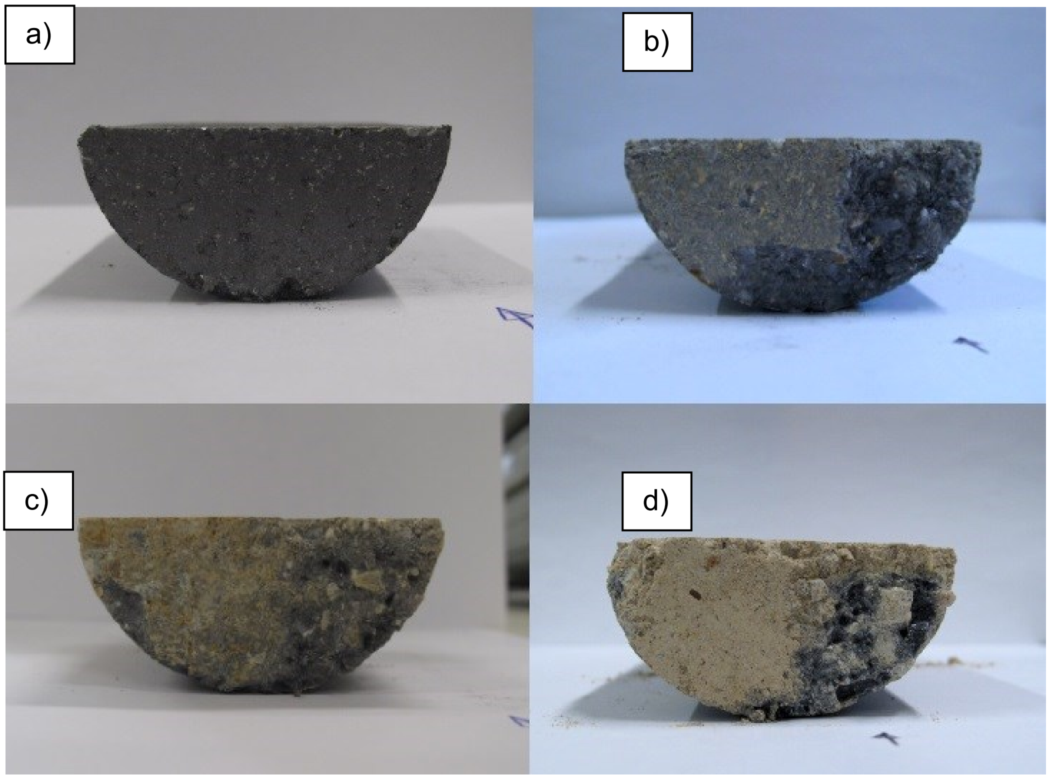

Fig. 26: The front side of the MgO-C refractory samples (material M3) after oxidation tests at air flow rate of 5 Nl/min and temperatures of a) 600K b) 700°C c) 800K d) 900 °C. The right side of the sample's front was scraped

The measured content of carbon monoxide and carbon dioxide in the exhaust gas were converted into the carbon mass flux density during the oxidation test. Fig. 27 presents experimental results for various test temperatures as a mass flux of reacting carbon versus time.

The curves representing temperatures of 1000 and 900 °C differ within the first 30 minutes, but afterwards they approach one another. The mass flux density curve at 800 °C shows a different shape within the first hour of the test, but afterwards it gets closer to the curves for 900 and 1000 °C which oscillate around a mass flux density of $1.5*10^{-4}$ kg/s·m^2. The mass fluxes densities of reacting carbon at 700 and 600 °C are of different order of magnitude than those at higher temperatures: they oscillate at ca. $5*10^{-5}$ kg/s·m^2 for 700 °C and $3*10^{-5}$ kg/s·m^2 for 600 °C. The carbon burnout rate is considerably lower, especially at 600 °C.

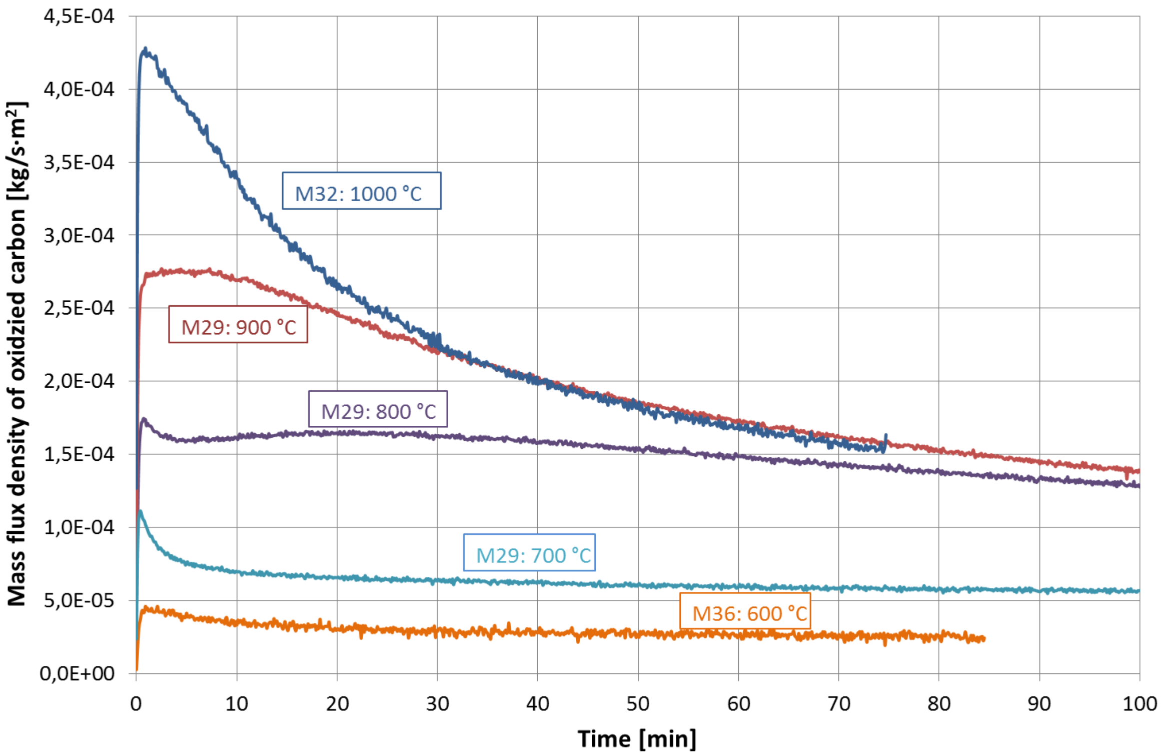

Fig. 27: Mass flux densities of reacting carbon during oxidizing tests of MgO-C samples type M3 at various temperatures

The goal of the experiments was to evaluate the kinetic model of carbon burnout described in Section 2.2.1. For this purpose, the experimental results were compared with calculations of decarburization depth executed using Eq. (44), which was achieved by integration of Eq. (18):

$$L = D_{eff} \cdot \left(-\frac{k_m + k_c}{k_m k_c} + \sqrt{\left(\frac{k_m + k_c}{k_m k_c} \right)^2 + \frac{4}{D_{eff}} \frac{C^{O_2}}{C^C} \cdot t} \right) \qquad (43).$$

In the computation, the mass transfer coefficient k_m was determined as described in Section 3.3. The effective diffusion coefficient D_{eff} was calculated according to Arrhenius relation presented in Section 3.2. For the calculation of the chemical reaction rate k_c various Arrhenius correlations, described in Section 2.2.2, were studied to consider their impact on the depth of the decarburized layer. The oxygen concentration C^{O_2} was calculated from the ideal gas equation for the respective temperature.

The decarburization depth curves achieved from the experimental data and calculated with Eq. (44) are presented in Fig. 28. The calculated curves have been computed using graphite oxidation kinetics proposed by Chi [32].

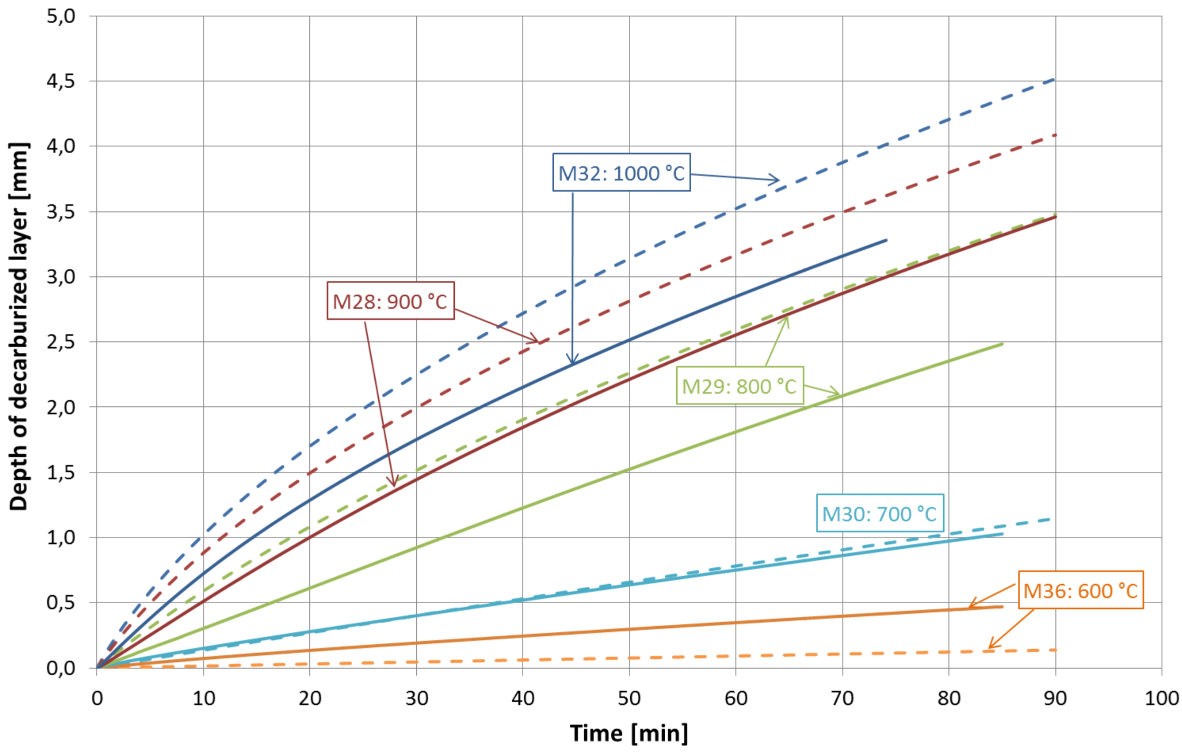

Fig. 28: Depth of MgO-C samples type M3 decarburized layer during oxidation tests at various temperatures. The continuous curves present experimental values, while the dashed lines present values calculated with Eq. (44) using the graphite oxidation kinetics proposed by Chi [32]

Analyzing experimental data, the decarburization depth during the tests at 900 and 1000 °C differ only about 0.25 mm. Carbon burnout at 800 °C is significantly lower than at 900 °C and the difference increases with the time to be nearly 1 mm after 70 min. The decarburization curves at 700 and 600 °C are nearly linear. The values at 700 °C are about 2.5 less than the values for 800 °C. The values at 600 °C are about the half of the values at 700 °C.

Compared to the measurements, the calculated curves of the decarburization depth for temperatures at 600 °C are about 60 – 70 % less. The calculated curve for 700 °C fits the experimental curve. At the temperatures of 800, 900 and 1000 °C the experimental depths are about 20 % mm less than the calculated values.

In Fig. 29, the curves of decarburization depth gathered from the experiments and calculated with Eq. (44) are compared; here the calculated curves were computed using the graphite oxidation kinetics proposed by Kim [33].

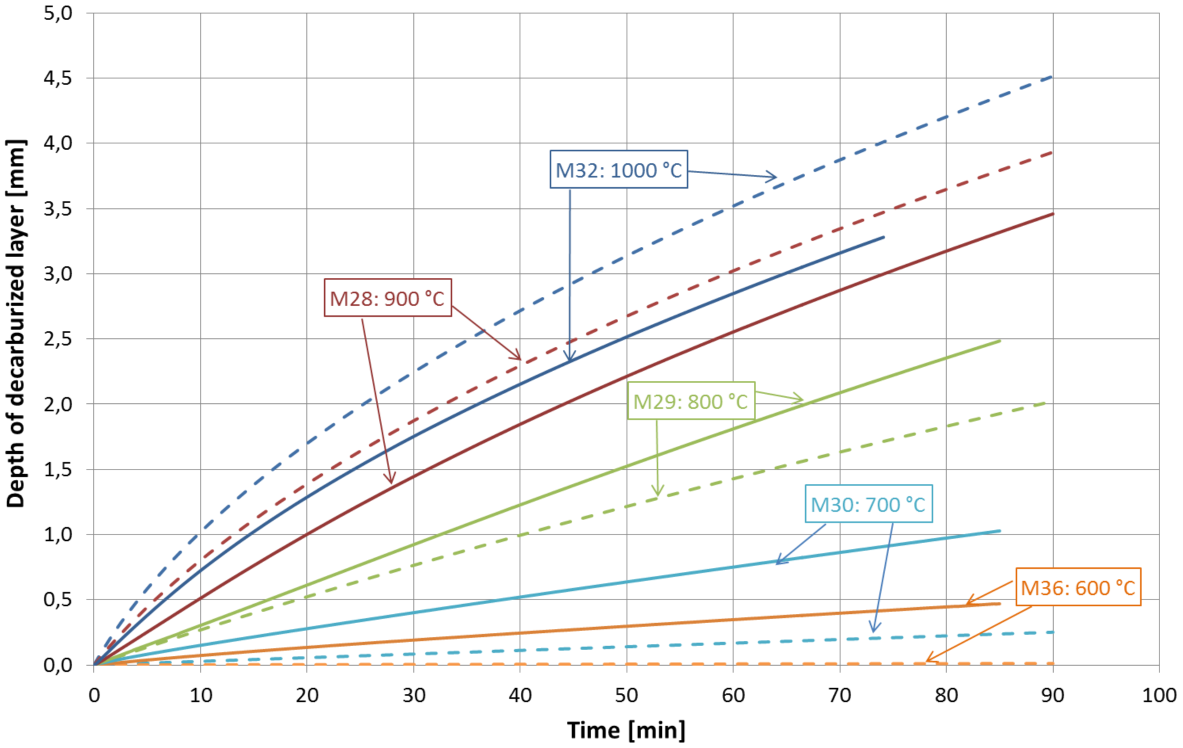

Fig. 29: Depth of MgO-C samples type M3 decarburized layer during oxidation tests at various temperatures. The continuous curves represent experimental data, while the dashed lines, data calculated with Eq. (44) using the graphite oxidation kinetics proposed by Kim [33]

The carbon burnout in MgO-C samples calculated using the graphite kinetics proposed by Kim showed nearly no decarburization at 600 °C. The values for 700 °C are about 70% less than the experimental results. For the temperature of 800 °C, the calculated curve fits the experimental with ca. 95 % accuracy. The calculated values at 1000 °C are the same as in the case with kinetics proposed by Chi [32] at 900 °C they are slightly less.

In Fig. 30 the experimental curves of carbon decarburization during the oxidation tests of MgO-C material type M3 materials are compared with curves calculated with Eq. (44), but in this case the chemical reaction kinetics was not considered at all, i.e. infinite chemical reaction rate was assumed. For the temperature of 1000 °C the result does not change in comparison to calculation presented in Fig. 28 and Fig. 29; for 900 °C the values are slightly larger. However, for all temperatures below 900 °C, the calculated values are much larger than the experimental ones and also larger in comparison with calculations where graphite kinetics was considered (see Fig. 28 and Fig. 29).

Based on these own conducted experimental data compared with theoretical results, the graphite kinetics has to be considered for the calculation of carbon burnout in MgO-C refractory materials at temperatures lower than 900 °C.

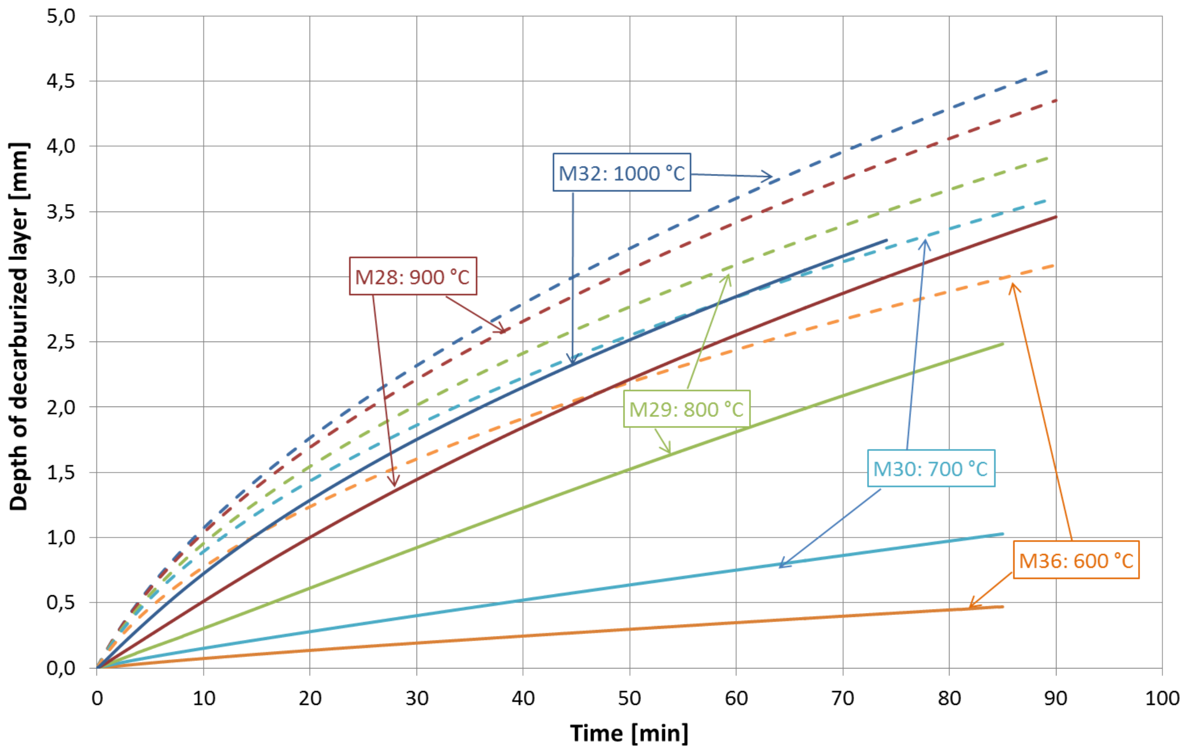

Fig. 30: Depth of MgO-C samples type M3 decarburized layer during oxidation tests at various temperatures. The continuous curves present the data achieved from experiments, the dashed lines present data calculated with Eq. (44) without considering chemical reaction kinetics

At 1000 °C several tests were executed to analyze the impact of the air flow rate on the carbon burnout. The applied flow rates were 2.7, 5.3, 7.7 and 10 Nl/min. In Fig. 31, the mass fluxes of reacting carbon during oxidation tests at various flow rates of air are presented.

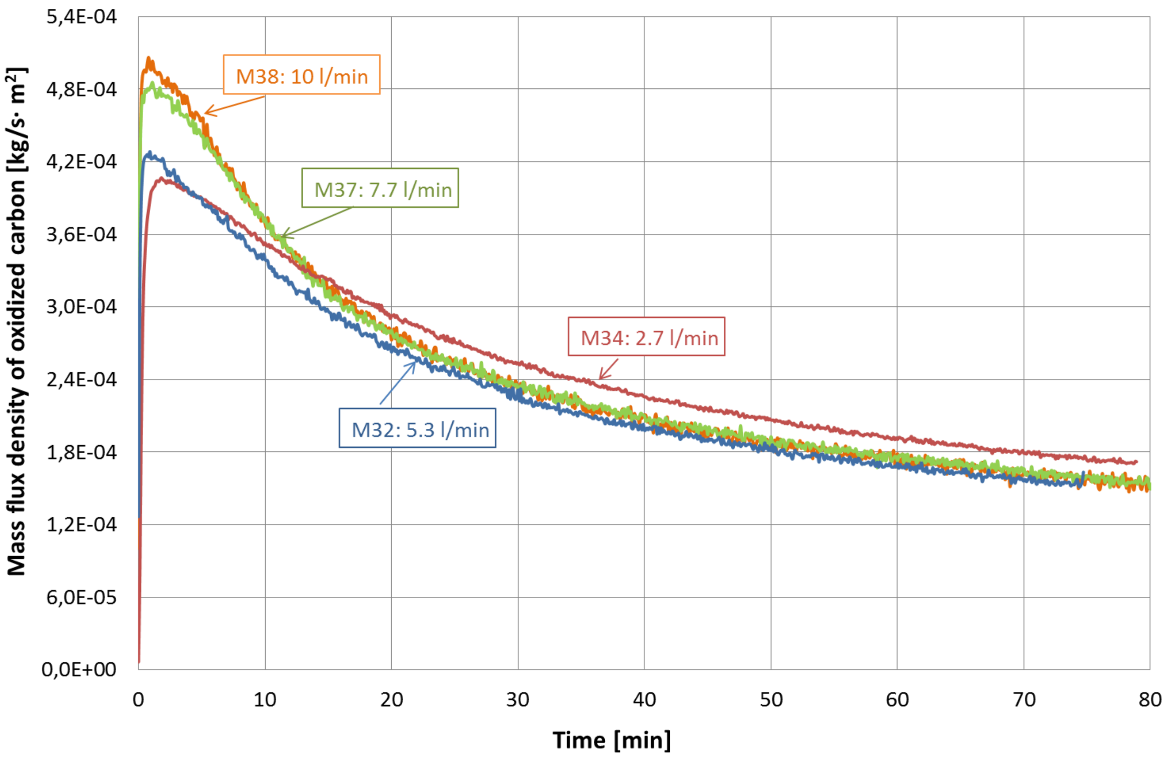

Fig. 31: Mass flux density of reacting carbon during oxidation tests for MgO-C samples type M3 at various flow rates of air

Within the first ten minutes of the experiment the applied flow rate of the air influences carbon conversion. Thereafter, the mass flux density curves at all flow rates approach one another with only exception for 2.7 Nl/min, which has slightly higher values. This could be explained with different rate-controlling regimes for the reaction: at the experiment start the mass transfer is the limiting factor, afterwards, the diffusion.

In Fig. 32 the experimental results were presented as change of the depth of the decarburized layer during the oxidation test. The curves are similar for flow rates 2.7; 7.7 and 10 Nl/min and at the end of the experiments the oxidation depth is nearly the same and equals 3.75 mm. The result for 5.3 Nl/min differs from the others and the final carbon burnout depth is about 0.2 mm less.

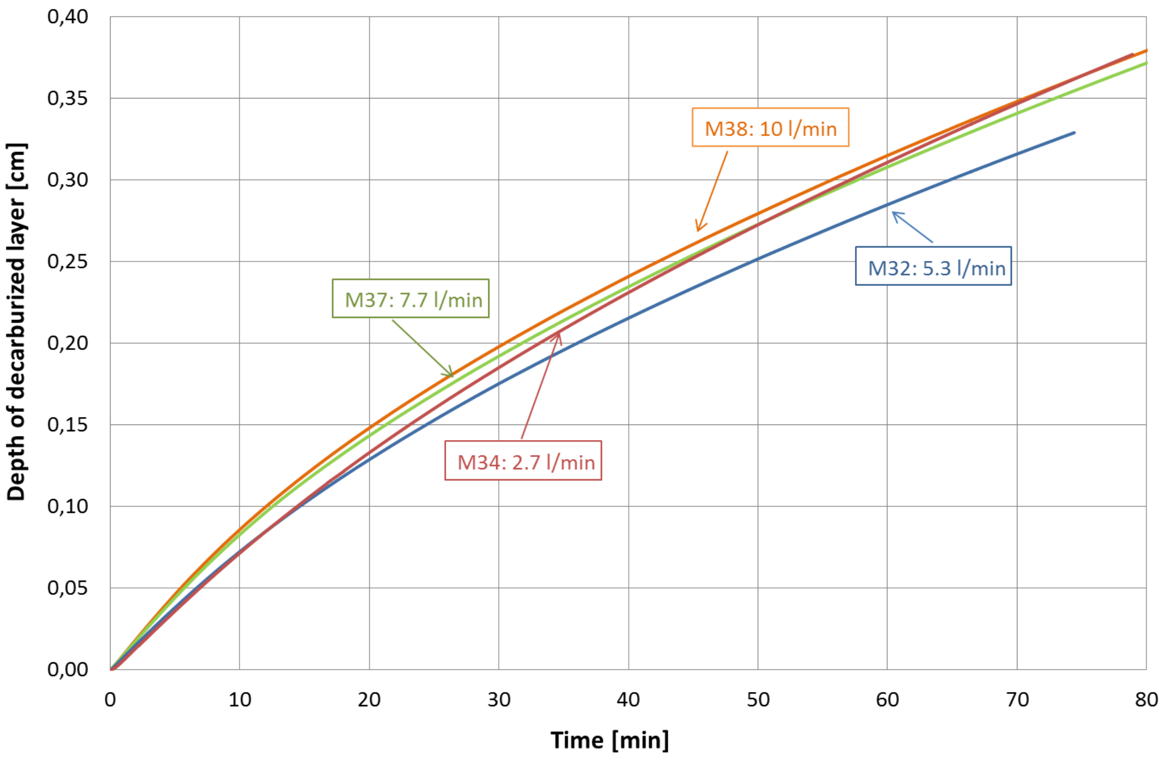

Fig. 32: Depth of decarburized layer during oxidation tests on MgO-C refractory type M3 for various air flow rates at a temperature of 1000 °C

Based on the decarburization curves presented in Fig. 32, effective diffusion coefficients were determined similarly as it in Section 3.2. However, for this experimental setup Eq. (18) for uniaxial oxidation was applied, same as in the experiments presented in [12]. The decarburization curves are then described with Eq. (44).

$$t = \frac{\rho_{M_C}}{4D_{eff} C_b^{O_2}} L^2 + \left(\frac{1}{k_m} + \frac{1}{k_c} \right) \frac{\rho_{M_C}}{2C_b^{O_2}} L \qquad (44).$$

The effective diffusion coefficient is then evaluated with the coefficient of L^2. In Fig. 33 the coefficients determined for different flow rates, but at the same temperature of 1000 °C are presented. For comparison purposes, the effective diffusion coefficient determined by TGA (see Section 3.3) is also shown in the figure and marked by a red point.

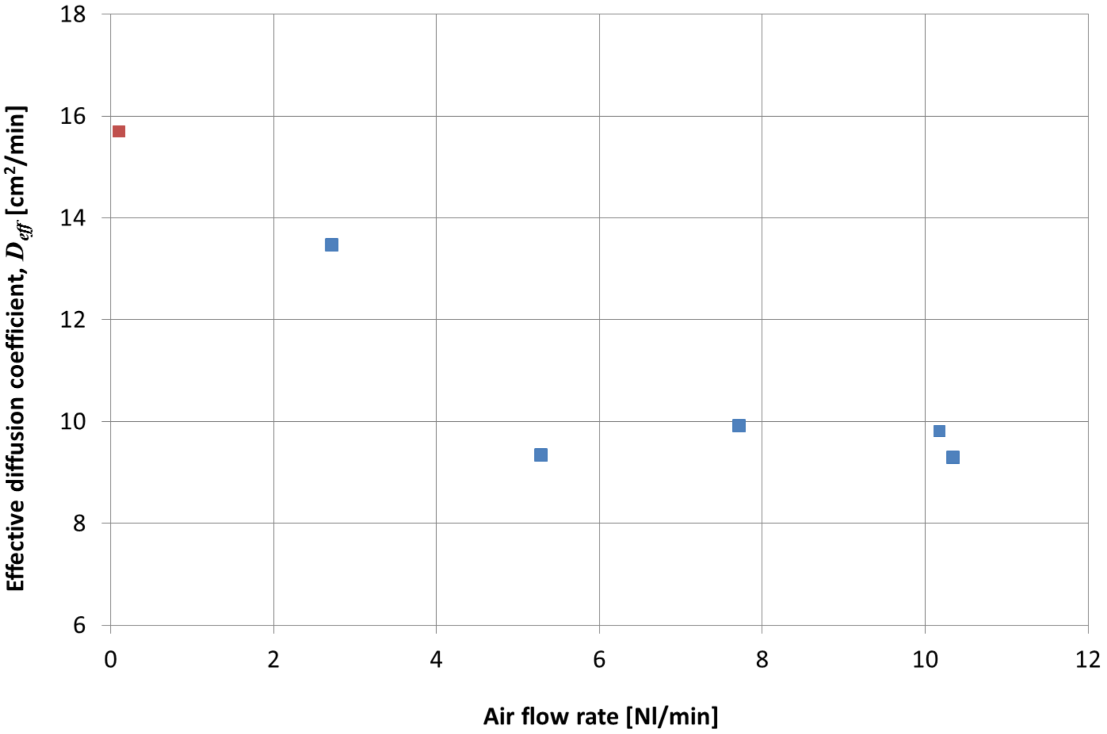

Fig. 33: Effective diffusion coefficients at 1000 °C determined during oxidation tests in a tube furnace for the MgO-C refractory material type M3 at various applied air flow rates. The red point shows the effective diffusion coefficient determined for this material by TGA (see Section 3.2)

The experimental values from the oxidation tests in the tube furnace are about 10 cm^2/min for all flow rates except for 2.7 Nl/min, which equals 13.5 cm^2/min. Those values are less than the effective diffusion coefficient determined by TGA, which equals 16 cm^2/min. Applying D_{eff} equal to 10 cm^2/min into the carbon burnout calculation yields decarburization depth values only 15 % greater than the experimental data (see Fig. 34). However, the question is, how the experimental setup influences the determination of the effective diffusion coefficient and what impact has the flow rate. To answer these questions, more detailed experimental work should be done with an improved setup. Proposed improvements should comprise gas temperature and velocity measurements in the tube and the consideration of the size of the gas-solid contact surface.

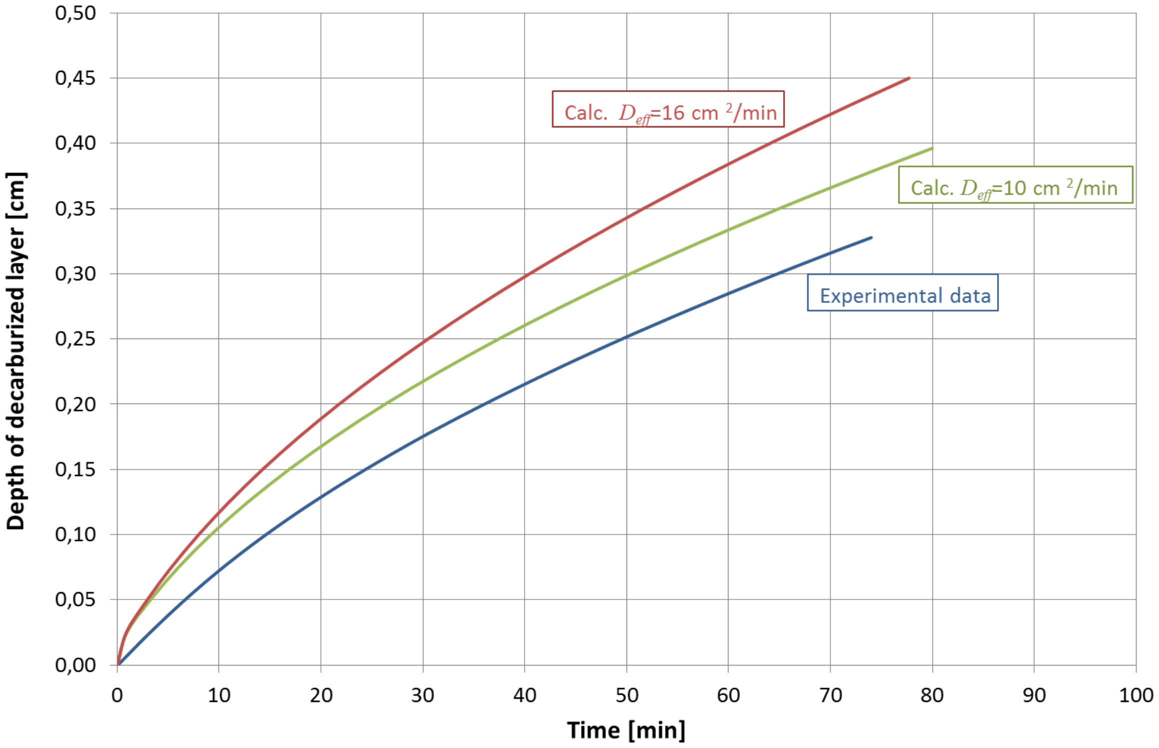

Fig. 34: Comparison of calculated depth of decarburized layer in MgO-C sample type M3 and experimental values for temperature of 1000 °C and flow rate 5.3 Nl/min. In the calculation different values for the effective diffusion coefficient D_{eff} were applied: 10 and 16 cm^2/min

4 Simulation of the preheating process

To estimate a possible carbon burnout in MgO-C refractories not only the refractory properties, like carbon content or porosity, but also the preheating conditions play a decisive role. One of the key factors is the oxygen content in the exhaust gas. Another important parameter is the lining temperature during preheating. Additionally, the gas flow pattern in the ladle is of interest, as it determines the mass transfer of gas species at the lining surface. With a CFD simulation, those data should be collected.

Within this thesis the results of steel ladle preheating simulations will be presented. The CFD calculations were executed using the commercial software ANSYS Fluent. A three dimensional model is used. During preheating the ladle is covered with a lid, which has two exhaust gas outlets. This fact did not allow applying an axisymmetric model. Instead, a quarter of the ladle with two symmetry walls was taken into the calculations. Due to the significance of the temperature development during preheating a transient calculation was carried out.

4.1 Process

The examined steel ladle is applied in in the steel mill of voestalpine Linz, Austria. The working lining consists of a non-basic monolithic castable in the bath area and magnesia carbon bricks in the slag area. The steel ladle is preheated to avoid later thermal shock damage of the refractory lining. Due to the castable, which contains a considerable amount of water after installation, preheating has to proceed slowly and lasts up to 39 h. During the first 6 h the ladle is purged only with hot air. Afterwards, natural gas firing is used as an energy source to preheat the refractory lining up to a temperature of 1000 °C. The described preheating takes place in a separate hall. Then, the steel ladle is transported to the steel works, where the end preheating proceeds. Here only the first heating step is analyzed.

The preheating is thermally controlled by temperature measurement at the ladle bottom, which has to be equal to the specified preheating temperature curve. According to that fuel gas and secondary air amount are adjusted. The average fuel gas flow rate value is about 40 Nm^3/h, that of secondary air 1600 Nm^3/h. Within the final six hours, when there is no water present anymore in the castable, the amount of gas increases linearly up to 110 Nm^3/h. This leads to an accelerated temperature rise in the lining. The primary air flow rate is not measured. Fig. 35 presents the temperature and flow rate data monitored during steel ladle preheating.

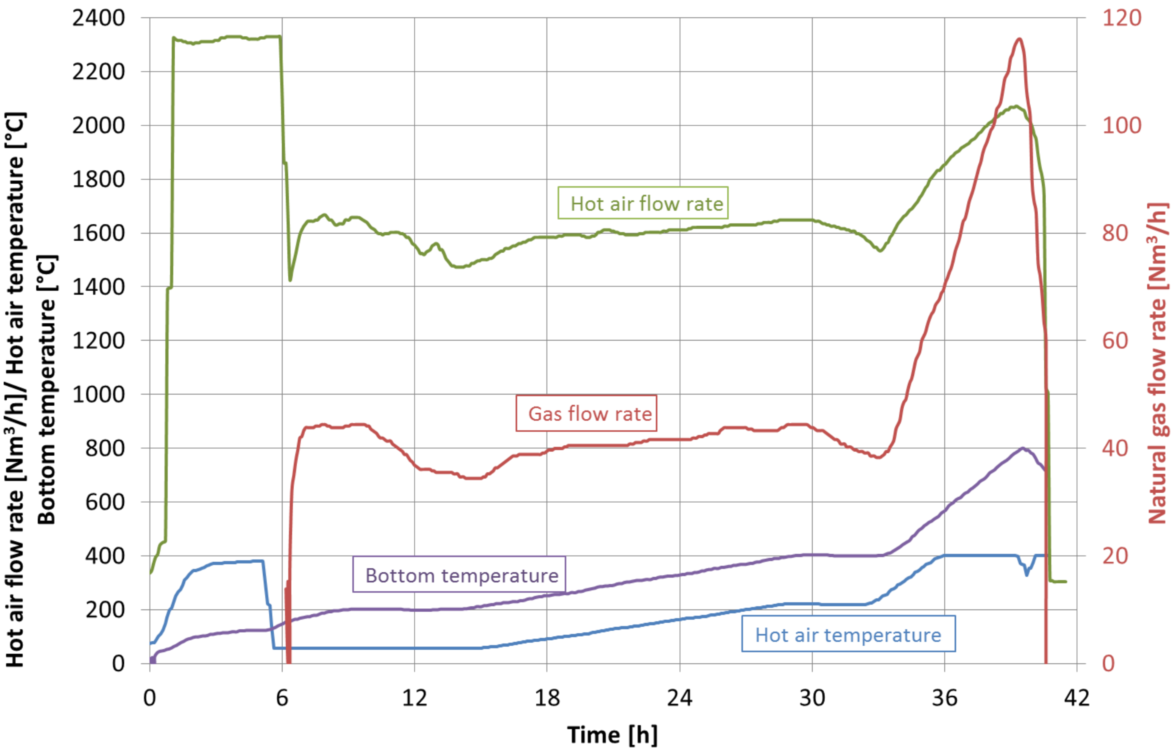

Fig. 35: Temperature of hot air, temperature at the ladle bottom, flow rate of hot air and flow rate of natural gas as registered during steel ladle preheating

4.2 Materials

The examined steel ladle is composed of a steel shell and a refractory lining. Its lining consists of a wear lining which is exposed to erosion and thus must be renewed several cycles and a safety lining, which has no direct contact with molten steel and is used permanently. The wear lining is composed of a high corrosion resistant MgO-C refractory in the slag area and non-basic low-cement castable in the bath area. As a safety lining a bauxite refractory with 80% of Al_2O_3 is applied. For insulation a fibre blanket and insulating boards are applied between the safety lining and the steel shell. In Fig. 36 the cross section of the steel ladle with applied materials is presented.

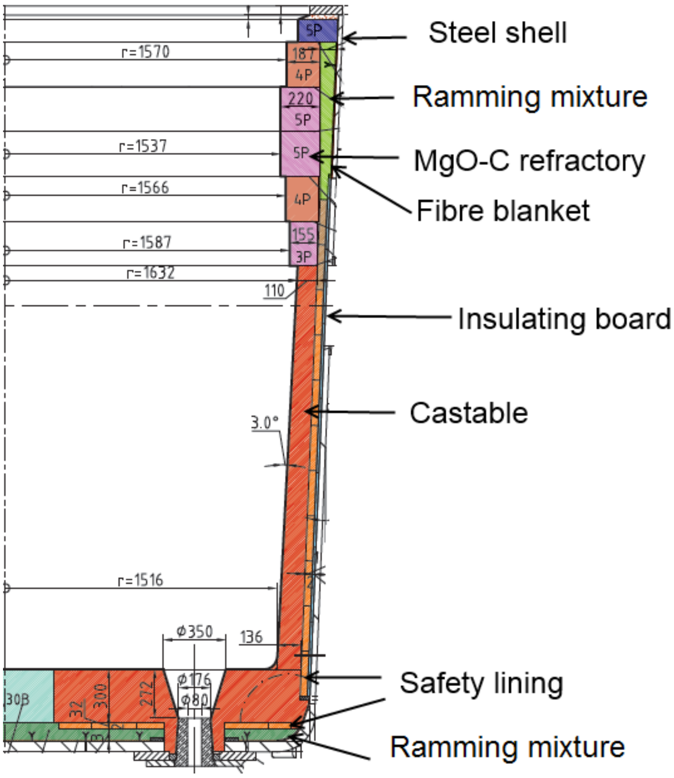

Fig. 36: Cross section of a steel ladle with applied lining materials

The properties of the lining materials are shown in Tab. 5. Heat capacities as well as thermal conductivities of particular materials depend on temperature. The heat capacity values were taken from [62].

Tab. 5: Properties of the lining materials.

Material	**Density** [kg/m^3]	**Thermal conductivity** [W/mK]			**Heat capacity** [J/kgK]			
MgO-C refractory	2900	11 (500 °C)	8 (750 °C)	6.5 (1000 °C)	856 (0 °C)	1000 (100 °C)	1200 (300 °C)	1354 (1600 °C)
Castable	3000	3.7 (400 °C)	2.7 (800 °C)	2.4 (1200 °C)	See Fig. 37			
Ramming mixture	3000	2.2 (whole temperature range)			833 (0 °C)	1338 (1600 °C)		1338 (1600 °C)
Safety Lining	2750	2 (whole temperature range)			707 (0 °C)	1338 (1600 °C)		1338 (1600 °C)
Insulating board	1200	0.23 (195 °C)	0.24 (315 °C)	0.31 (600 °C)	1000 (whole temperature range)			
Fibre blanket	10	0.05 (200 °C)	0.1 (400 °C)	0.19 (600 °C)	1700 (whole temperature range)			

An effective heat capacity was defined for the castable as a function of temperature at a given preheating rate, where evaporating of water at 100-110 °C, as well as the release of chemically bonded water at 240 - 300 °C were included within. Fig. 37 presents the effective heat capacity of the castable as a function of temperature [62].

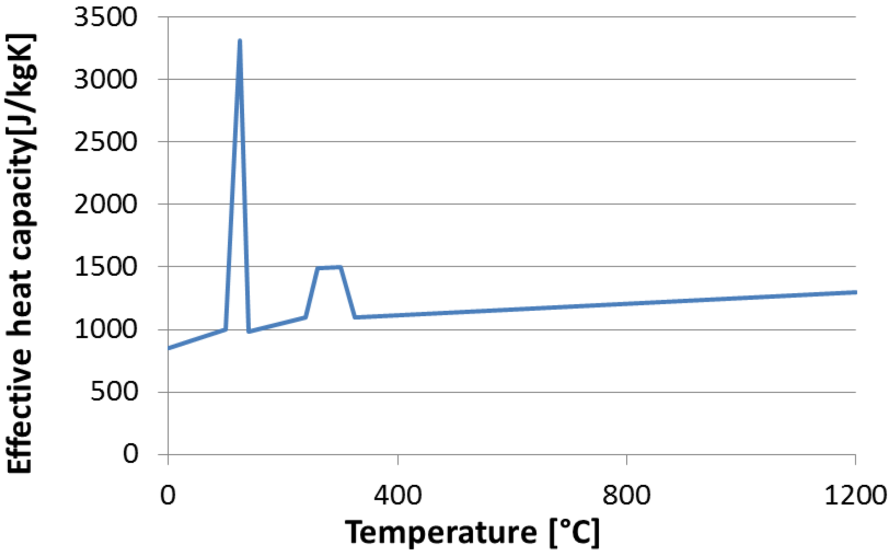

Fig. 37: Specific effective heat capacity of the castable including water release as a function of temperature [62]

4.3 Geometry and mesh generation

The ladle geometry and mesh were generated with the commercial software Gambit. Fig. 38 shows the 3D model used in the simulation, which was built according to the design plan. The height of the side walls is 3.7 m. The radius depends on the ladle height and varies between 1.5 to 1.7 m. The grey shaded region in Fig. 38 represents the MgO-C lining with a height of 1.37 m and a thickness up to 0.22 m. During preheating the ladle is covered with a lid. In the middle of the lid, a burner is located.

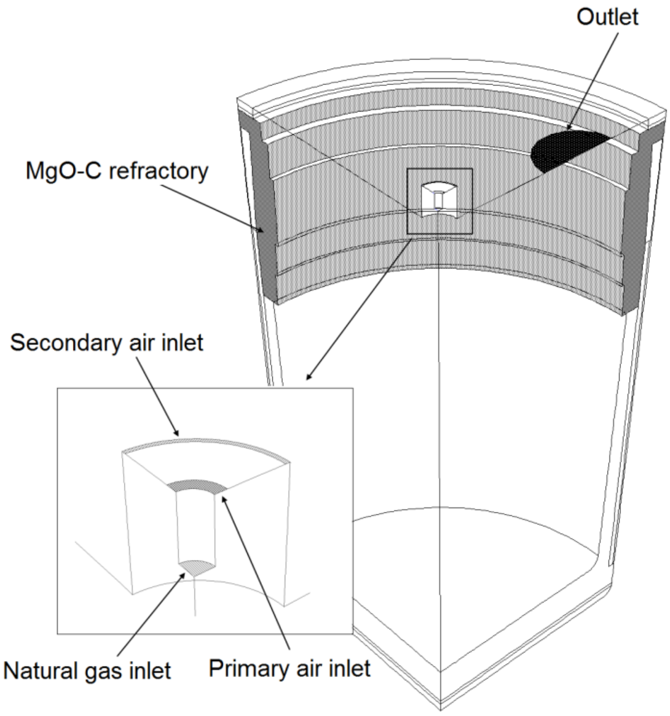

Fig. 38: Steel ladle geometry applied for the simulation with specification of inlet and outlet boundaries

The ladle model consists of gas and solid (refractory) domains, two symmetry walls, outlet and three inlets: natural gas inlet, primary and secondary air inlet. For better representation of the flow at the outlet, the geometry was extended at this region (Fig. 39a red mark). Fig. 39 represents a view at one symmetry plane of the created mesh and an enhanced look at the gas inlets.

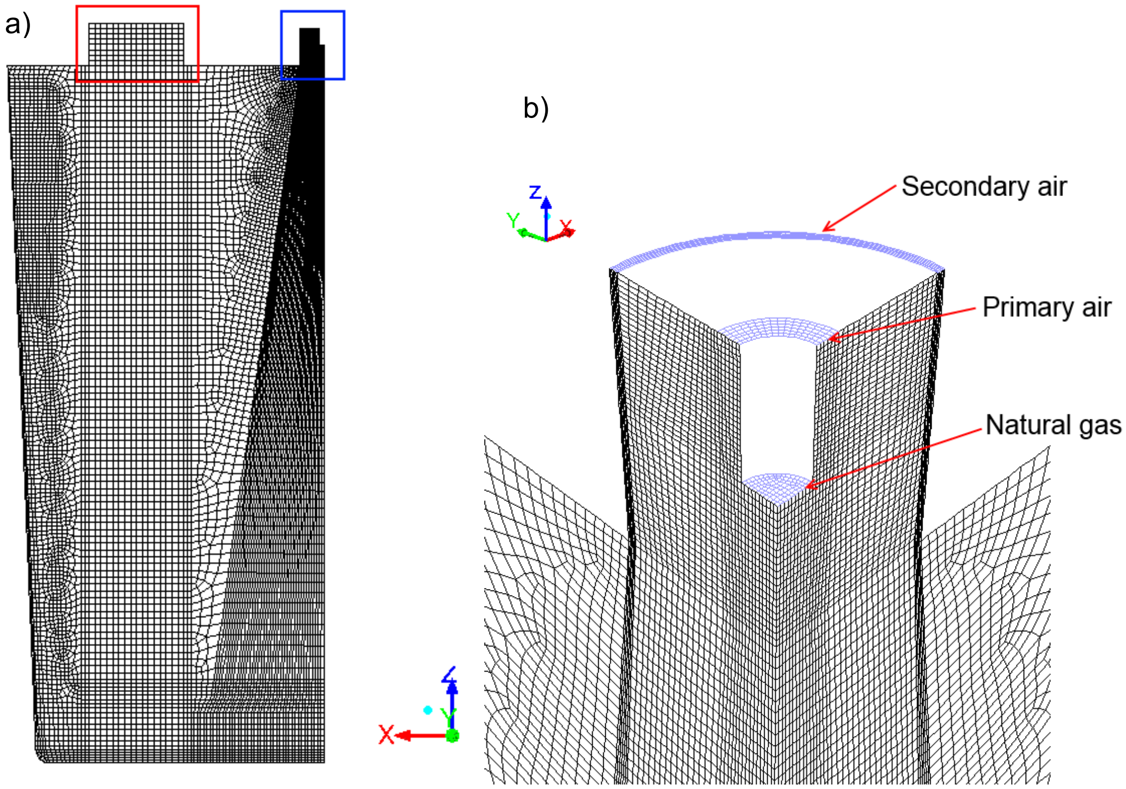

Fig. 39: Created mesh for the CFD simulation; a) view at one symmetry plane of the mesh with marked outlet (red) and combustion chamber (blue) b) mesh at the gas inlets area with marked gas, primary and secondary air inlet

The generated mesh consists of 387735 hexahedral cells with non-equal cell spacing. Fine meshing was used in the flame region as well as at near-wall area with the smallest cell size of 1.75 $*10^{-8}$ m^3, and larger cells in the rest of the ladle, with the maximal size of $1.64*10^{-4}$ m^3.

The inlet velocity profiles of gas and secondary air were precalculated in a separate simulation, as the geometry of the natural gas burner is more complex and requires a much finer mesh. Fig. 40 represents the design of the burner in detail.

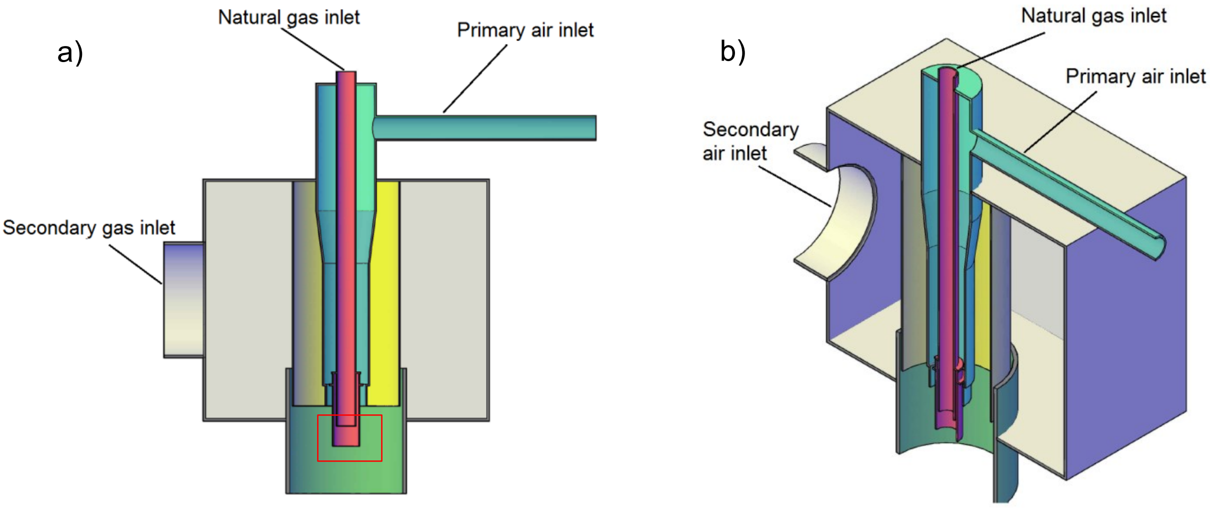

Fig. 40: Design of the burner with marked inlet flows a) front view with marked natural gas inlet b) side view

In Fig. 41 an enhanced view of natural gas inlet (marked red in Fig. 40) with an example of the velocity profile is shown. The calculations were done for various flow rates of gas and the velocity profiles were saved and then applied in the simulation of the steel ladle preheating.

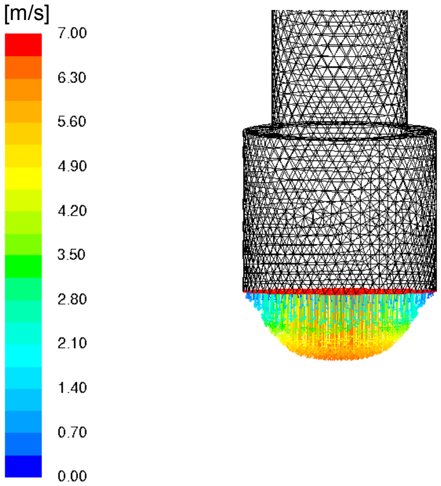

Fig. 41: Example of natural gas velocity profile at a flow rate of 44 Nm^3/h

4.4 Simulation setup

The models used for gas combustion during ladle preheating, described in Section 2.3.3, are provided by ANSYS Fluent. A detailed explanation of the model implementation in Fluent can be found in the Fluent User's Guide [87].

Combustion modeling

As the free jets of gas and air are mixed after entering the combustion chamber, a non-premixed approach was applied to model the combustion and to characterize the flue gas composition and temperature. Based on [94] and [95] for the description of the combustion kinetics and the species transport, a 41-reaction mechanism consisting of 16 species for methane combustion, according to [93], was chosen. The composition and the entering temperatures of incoming gases are given in Tab. 6.

Tab. 6: Composition (molar fraction) and temperature of fuel and oxidizer

	Fuel	*Oxidizer*
CH_4 [-]	1.00	
O_2 [-]		0.21
N_2 [-]		0.79
Temperature [°C]	300	330

Based on the above defined kinetics and boundary conditions of gases, laminar non adiabate flamelets were generated. The generated flamelets were included in the calculation of PDF-Lookup-Tables.

Heat transfer modeling

The heat released during the combustion is transferred to the walls by convection and radiation. The convective heat transfer at the refractory surface is solved using the standard wall functions in FLUENT, available within the realizable k-ε turbulence model [87]. The radiative heat transfer was simulated with Discrete Ordinates (DO) approach. This model solves the radiative heat transfer equation for a finite number of discrete solid angles, each associated with a vector direction [87]. The number of solid angles was chosen according to studies presented in [100] and was doubled compared with the default values. A non-gray formulation of weighted-sum-of-gray-gas (WSGG) model was employed to compute the gas absorption coefficients [87].

Turbulence modeling

Turbulence was calculated with a realizable k-ε model with default values for model constants.

Spatial discretization and transient formulation

As the temperature evolution in the lining during preheating is of interest for this thesis, a transient simulation was chosen. Due to computational time constraints a modified calculation method was used. The time step size was predefined in dependence of the calculated domain. For the gas domain a time step smaller than 0.1 s was chosen, and for the solid domain, a time step of several seconds was applied. SIMPLE algorithm was used to model the pressure-velocity coupling and a second-order upwind scheme was chosen to solve all governing equations.

4.5 Boundary conditions

The values necessary to set boundary conditions were taken from data registered during steel ladle preheating. Primary air – the unknown quantity – was calculated from the natural gas flow rate with the assumption of an excess air coefficient (λ) equal to unity. Due to the convoluted geometry of the burner, preliminary simulations were done to obtain velocity profiles at the combustion chamber inlet. For simplification, the whole preheating procedure was divided into phases of different duration, so to keep constant boundary conditions in each individual phase. Tab. 7 presents the flow rates and velocities of the gas streams used in the calculations.

Tab. 7: Flow rates, fuel gas and air velocities of streams entering the burner chamber for each of the simulated phases

Phase	Duration Time [min]	Flow rate [Nm^3/h]			Secondary air Temperature [°C]	Mean velocity [m/s]		
		Gas	Primary air	Secondary air		Gas	Primary air	Secondary air
1	42			405	100			7.5
2	17			1395	192			24.1
3	295			2320	321			40.1
4	47	34	324	1510	57	3.6	20.6	61.6
5	177	44	419	1647	57	4.6	26.6	63.8
6	129	41	393	1604	57	4.3	25.0	66.0
7	262	35	338	1512	57	3.7	21.5	61.6
8	563	41	387	1596	57	4.3	24.6	66.0
9	241	44	416	1637	127	4.6	26.4	63.7
10	198	41	393	1613	207	4.3	25.0	78.4
11	91	43	413	1635	221	4.6	26.2	63.7
12	96	63	598	1809	272	6.5	37.9	73.4
13	91	82	778	1938	364	8.5	49.4	78.4
14	96	104	986	2044	400	10.8	62.6	81.8

The temperatures of primary and secondary air listed in the Tab. 7 were measured. The temperature of natural gas was equal to 25 °C, while the initial lining temperature was set to 10 °C. The heat loss at the outer walls of the ladle was set to 15 W/m^2. The outlet in the lid was set to a pressure outlet.

4.6 Simulation results

The data required for prediction of possible carbon burnout in MgO-C refractories according to kinetic model described in Chapter 2 are the temperature distribution in the lining, the gas temperature distribution, the gas velocity field and the gas composition. Within this chapter, the simulation results relating to aforementioned quantities will be presented.

4.6.1 Gas velocity and temperature fields

Fig. 42 illustrates the calculated velocity pathlines in the ladle after 20 and 36.8 h of preheating (phase 8 and 14). The peak velocities are reached within the secondary air jet and equal 75 m/s in phase 8 and 95 m/s in phase 14. In the flame region, the gas velocity decreases, in the case of phase 14 the velocity values are about 75% of the values in phase 8. In both cases, in the middle of the ladle bottom a stagnant point can be observed. The gas flow moves from that point over the ladle bottom and rises along the walls up to the lower MgO-C layers, where it collapses because of the ladle geometry. Therefore a circulating flow develops in the lower part of the ladle. In its upper part another circulation pattern can be observed at that symmetry plane, where there is no gas outlet. At the other symmetry plane no characteristic flow pattern can be defined, except an overall trend of flow towards the outlet. The gas flow pattern in the ladle remains very similar for all phases.

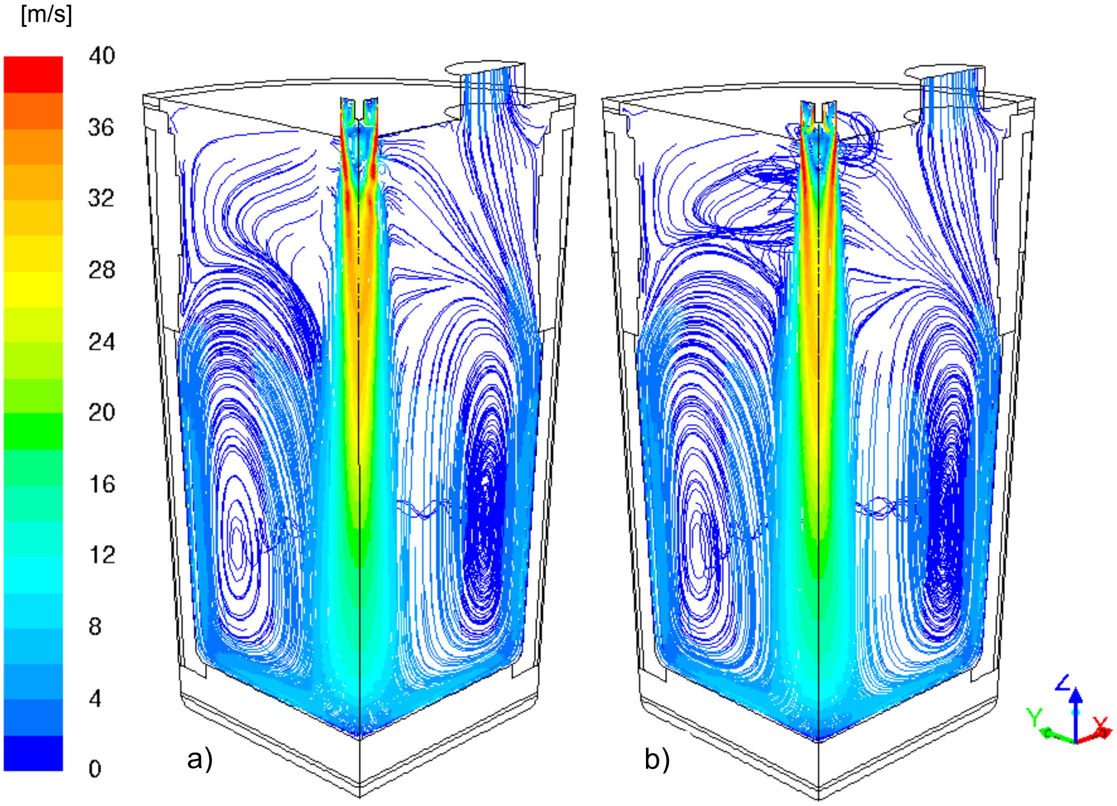

Fig. 42: Simulated velocity path lines after a) 20 and b) 36.8 hours of ladle preheating in m/s

The velocity field is of importance for the calculation of decarburization depth in MgO-C refractories, since it influences the mass transfer of oxygen to the refractory surface. Fig. 43 presents the velocity vectors in a distance of 1 cm from the MgO-C refractory hot face after 36.8 h and 39 h of preheating. Due to the lining geometry, the gas flow in the slag area is not homogeneous. At higher firing rate (after 39 h of preheating), the velocities are slightly higher and thus the flow pattern changes.

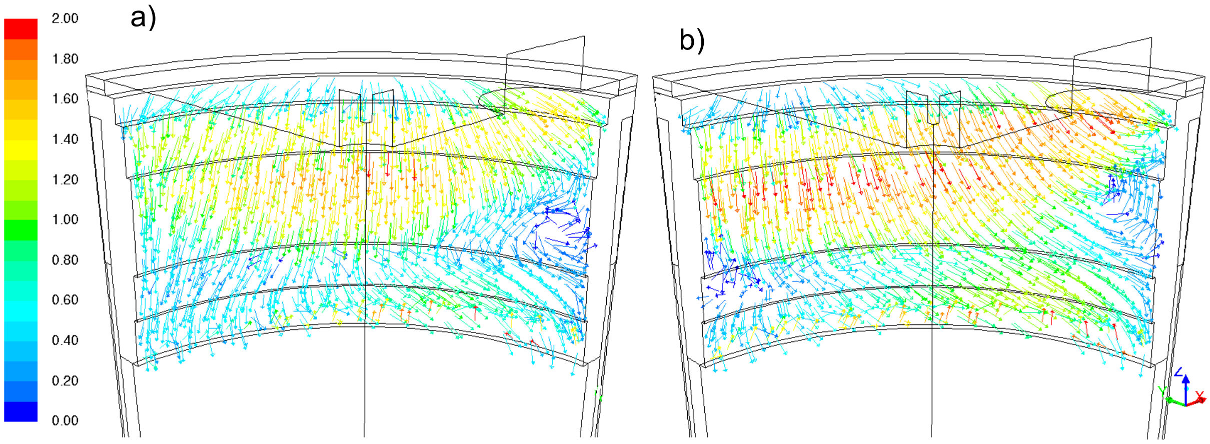

Fig. 43: Velocity vectors in m/s at 1 cm distance from MgO-C refractory wall after a) 36.8 and b) 39 h of preheating

Fig. 44 shows the calculated temperature distribution in the gas phase and in the ladle lining. Computed peak flame temperatures were 1825 °C within the 20th h of preheating and 1930 °C within the 36th h of preheating. The gas temperature distribution in the ladle agrees with the velocity flow pattern shown in Fig. 42. The temperature field of the flame depends on the preheating phase. In Fig. 44a, the flame is short and a high temperature region concentrates close to the burner. In Fig. 44b in 36th h of preheating, the flame stretches, the highest temperatures are achieved in the middle of the ladle height and the hot gas stream reaches the ladle bottom.

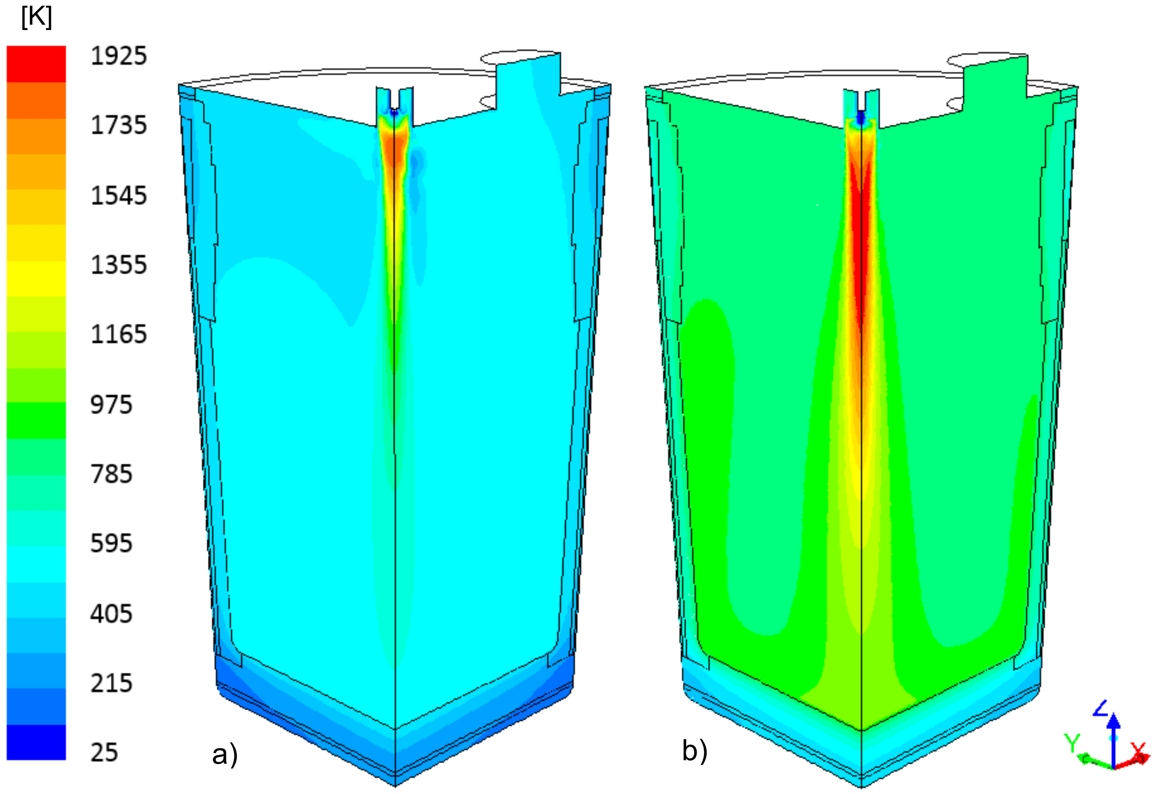

Fig. 44: Simulated temperature distribution in the gas and in the lining after a) 20 and b) 39 h

4.6.2 Temperature distribution in the lining

Steel ladle preheating is controlled by the temperature measured at the ladle bottom, which should coincide with a specified preheating temperature curve. To verify simulation results calculated and measured temperatures at the ladle bottom have been compared (Fig. 45). Within the first five hours, when the ladle is purged only with hot air, both temperatures agree with one another. After starting gas firing, the calculated values are about 25-30% higher than the measured ones. The temperature difference could be explained by incorrect assumption of primary air amount or by inadequately considered possible heat losses. In spite of this uncertainty, the calculated and measured temperature curves show similar trend.

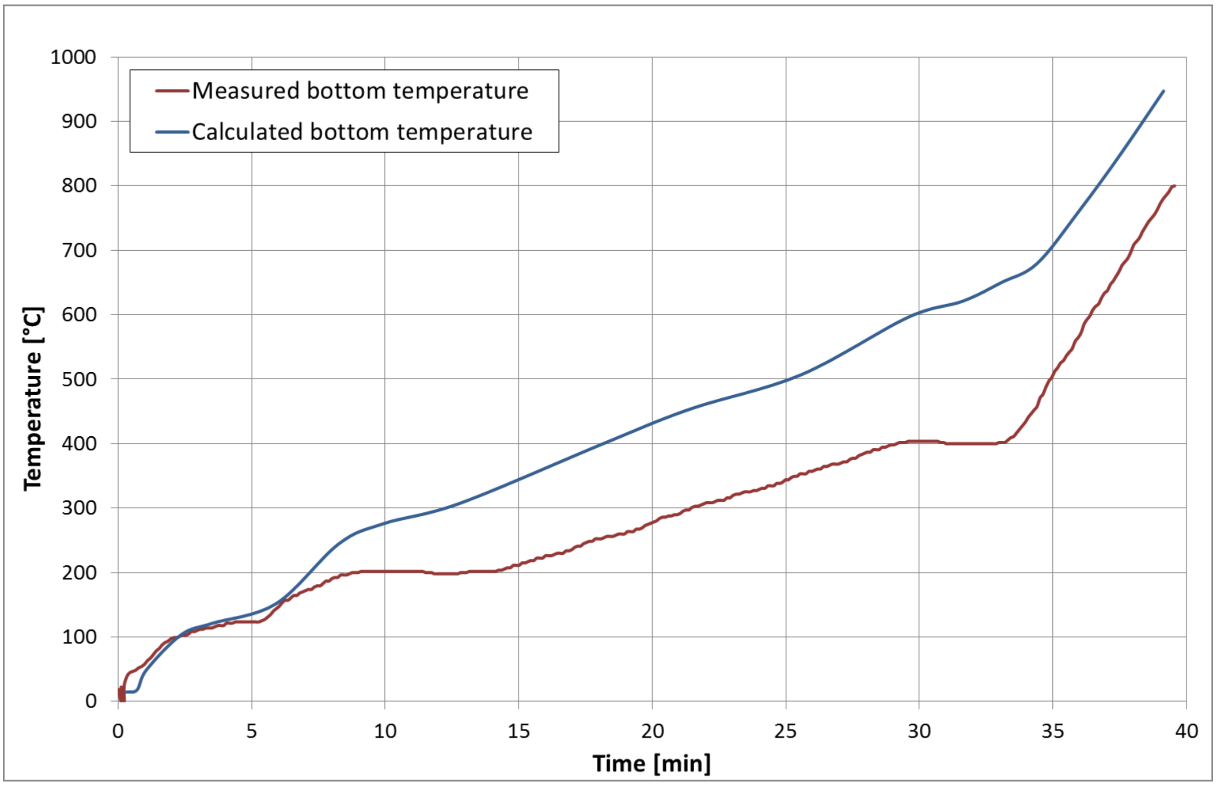

Fig. 45: Comparison of the calculated and with the measured temperature at the ladle bottom

The temperature distribution in the ladle lining after 20 h, 36 h and at the end of preheating after 39 h is shown in Fig. 46. Within the last six hours, the heating rate of the gas burner increases and thereby the lining temperature rises faster (see Fig. 46). Because of this comparison, it can be concluded that within the thin castable side wall temperature is distributed consistently. On the contrary, at the bottom region with castable thickness of 0.3 m, the temperature distribution is more uneven. The cold-face temperatures are about 300-400 °C less than the hot-face temperatures.

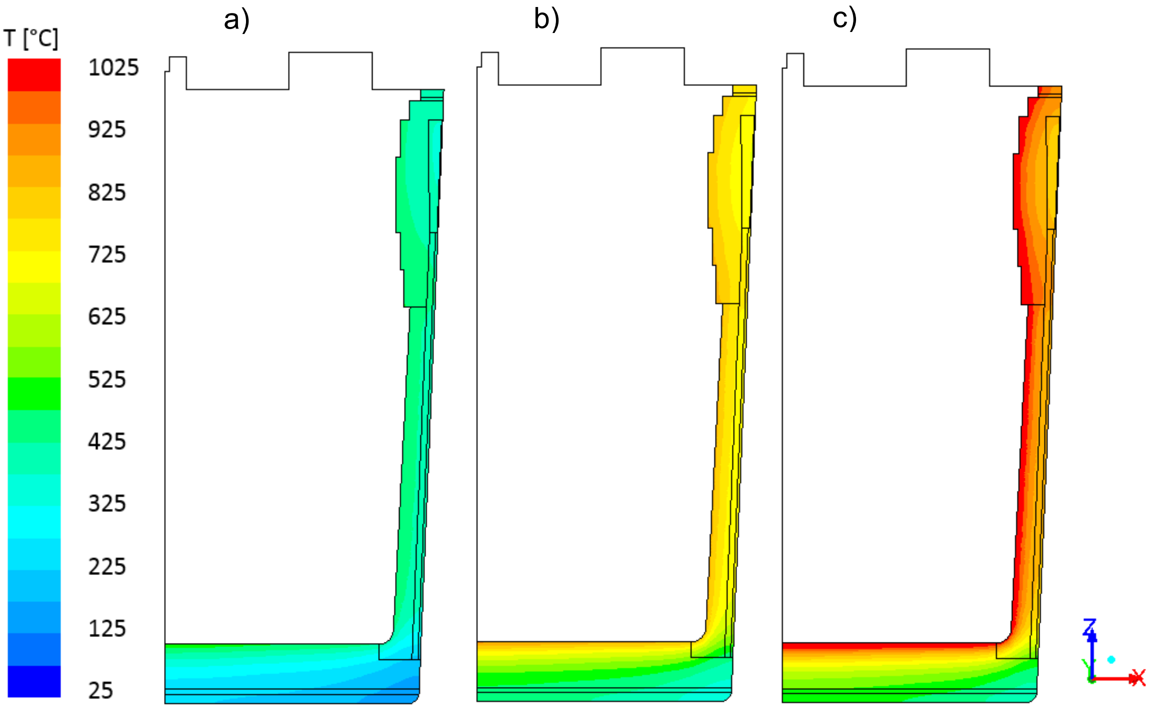

Fig. 46: Cross section of steel ladle presenting the temperature distribution in the lining after a) 20 b) 36 c) 39 h

Fig. 47 illustrates the change of the temperature distribution in the MgO-C refractory during ladle preheating. The marked lines indicate the height measured from the ladle bottom and are further used in Fig 48 for comparison of the temperature development within the lining in dependency of the height.

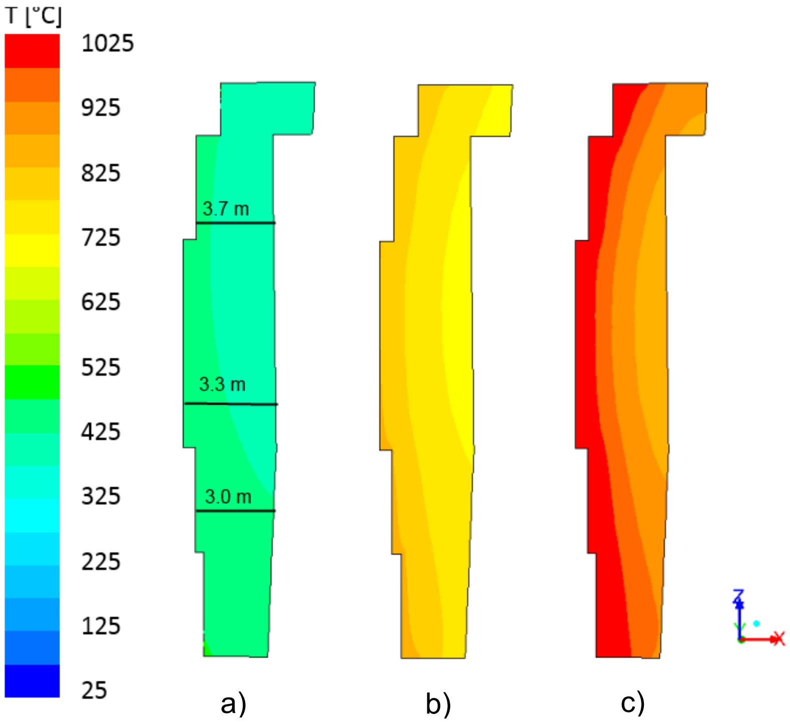

Fig. 47: Temperature distribution in MgO-C refractory after a) 20 b) 36 c) 39 h

The temperature at the surface of the MgO-C refractory during preheating is presented in Fig. 48. The three curves described with z=3 m, z=3.3 m and z=3.7 m correspond to marks in Fig. 47a and present the temperature at various heights of the ladle. The dashed curves present the temperature difference between the hot face and the cold end of the refractory. The temperature at the surface is nearly independent from the ladle height, while this is not the case for the temperature at the cold end. The temperature difference between hot and cold end of the lining at the ladle height of 3 m is about 40 °C; at the height of 3.3 m about 44 °C and 50 °C at 3.7 m . At the diagram, we can see three different preheating phases. Within the first 6 h, the ladle is heated only with hot air and the curve appears rather flat. The next 30 h the ladle is heated by natural gas firing with a similar energy input. The temperature at the surfaces rises constantly; the difference to the cold end does not change and is approximately 40 °C. Within the last six hours, when the heating rate rises rapidly, also the surface temperature and the temperature difference increase.

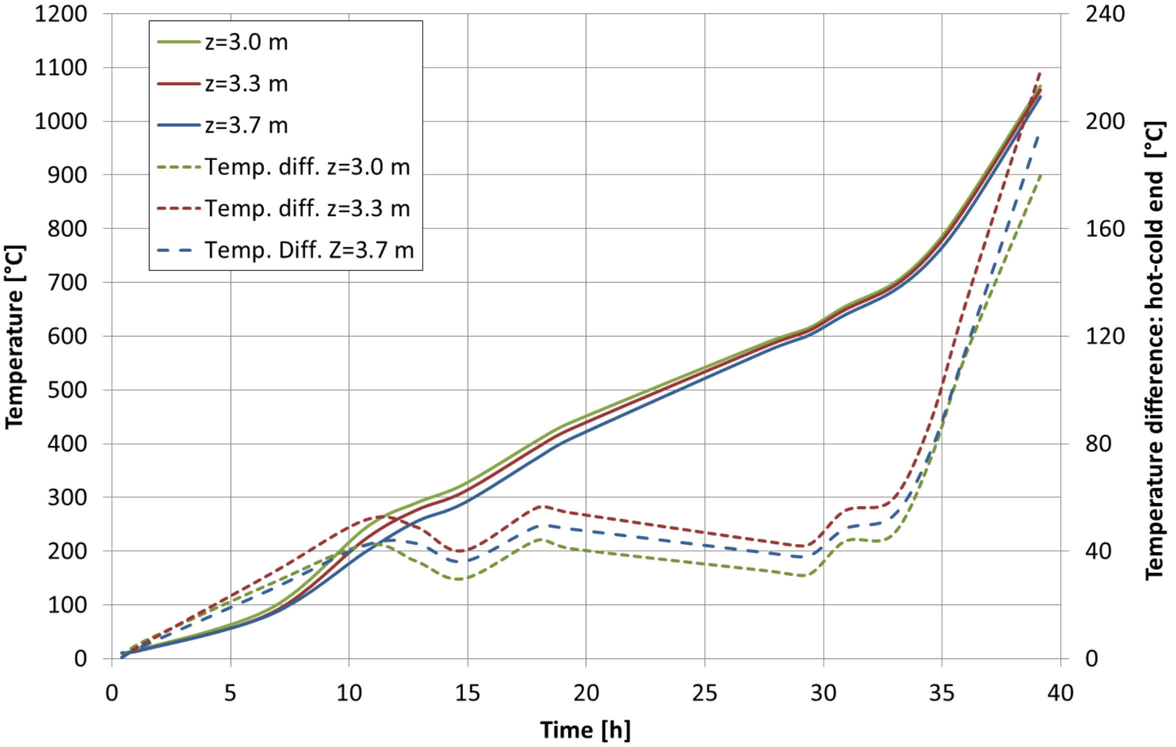

Fig. 48: Temperature evolution at the hot face and temperature difference between hot face and cold end during ladle preheating within MgO-C refractory at various ladle heights

Considering the possible carbon burnout in the MgO-C refractory and relating it to graphite oxidation kinetics described in Chapter 2.2.2, especially the regions exceeding the temperature of 800 °C are of interest. According to Fig. 48 those temperatures occur after 35 hours of preheating at the refractory surface and two hours later also at the cold end of the refractory.

4.6.3 Heat flux at the lining walls

Fig. 49 illustrates heat flux at the lining walls after 36 h of preheating. The highest heat transfer occurs at the ladle bottom, the lowest values are reached in upper part of the castable wall. The heat flux at the walls partly reflects the gas flow pattern in the ladle. At the ladle bottom the flame jet meets the lining surface with high velocity and therefore the convective heat flux reaches here its maximum values. Before it reaches the region of the MgO-C refractory the flow along the walls collapses and the convective flux does not play such an important role. The radiative heat transfer is more important in the MgO-C refractory region.

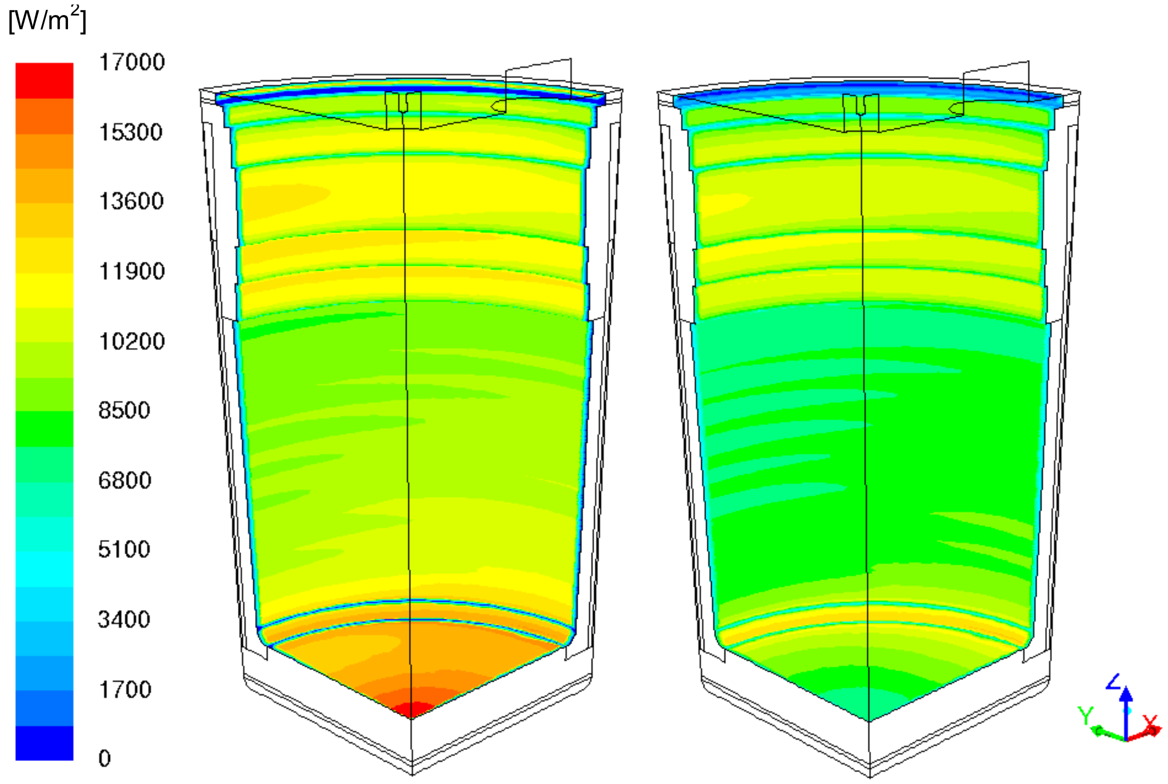

Fig. 49: Comparison of: (a) total heat flux and (b) radiative heat flux at the lining walls after 36 hours of preheating in W/m^2

Fig. 50 presents the comparison of the radiative with the convective heat flux at the lining walls. Close to the flame, at the slag bath area, the radiative heat flux dominates; it comprises nearly 100% of the heat source and rises with increase of the preheating time. At the ladle bottom the convective heat transfer is the dominant one within the first 20 h of preheating. Afterwards, same as at the castable walls, both types of heat flux have a significant impact. As preheating time increases, radiative heat transfer dominates over convective transfer.

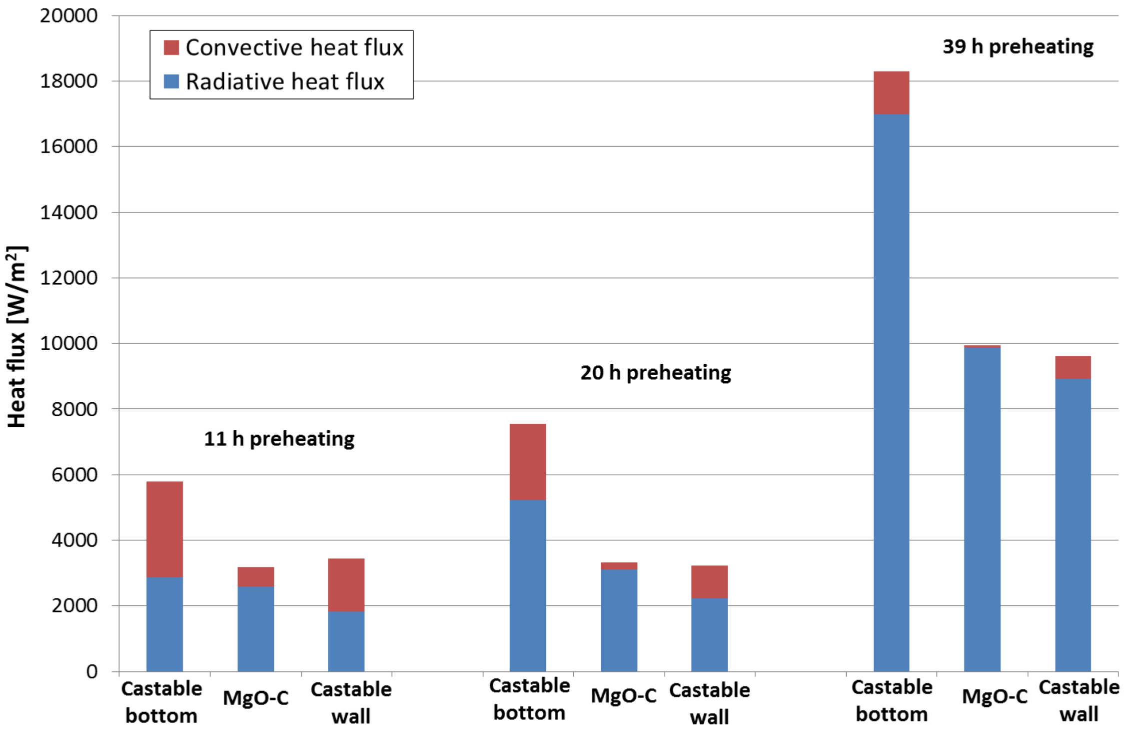

Fig. 50: Convective and radiative heat flux at the lining walls after 11, 20 and 39 h of preheating

Fig. 51 presents an average heat flux at the lining walls during preheating. After the increase within the first 3 h, the heat flux at the lining walls stays constant to a great extend amounts 6000 – 8000 W/m^2 for the ladle bottom and 3000 – 4000 W/m^2 for the castable wall and the MgO-C lining. Within the last 6 h, it increases rapidly and doubles its values.

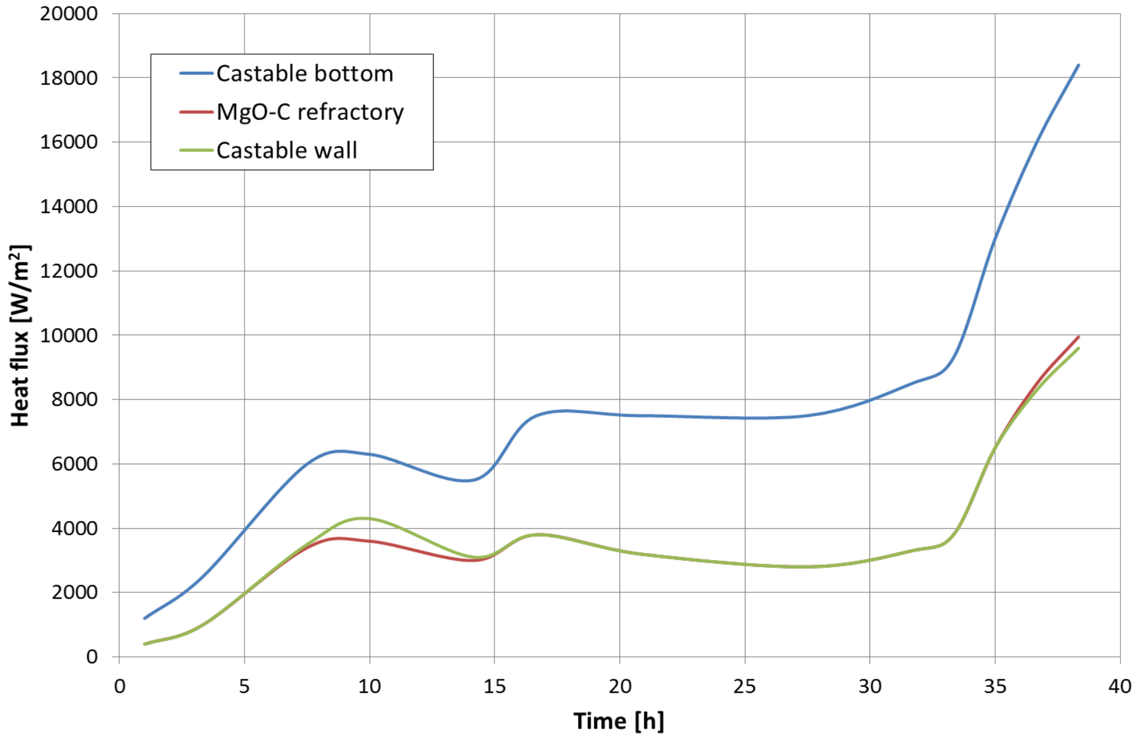

Fig. 51: Heat flux at the lining walls during ladle preheating

4.6.4 Gas composition

Fig. 52 presents the mass fraction of oxygen in phase 13 (37th hour of preheating). Within the reaction zone the oxygen mass fraction changes. In the remaining region a constant value of residual oxygen is reached. In the case of phase 13, this equals 7 mole percentage.

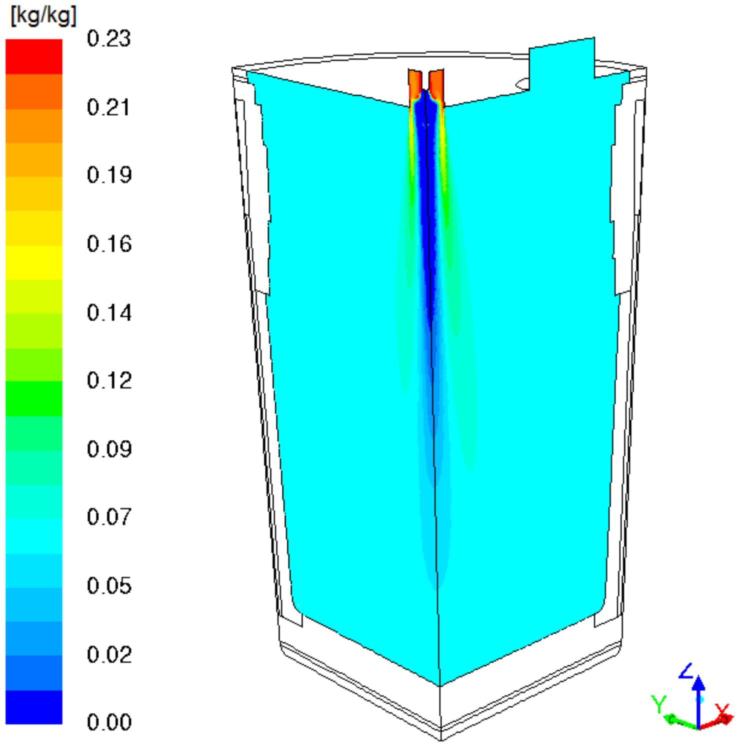

Fig. 52: Mass fraction of oxygen in the gas phase in phase 13 after 36.8 h of preheating

At each phase described in Tab. 7 a quasi-steady state is reached within the gas phase. It means that the gas composition and gas temperature distribution within every phase do not change. In Fig. 53, mole percentage of oxygen for every phase is presented. The first three preheating phases present a period when there is no gas firing and only hot air is purged. Thereby, the mole percentage stays constant and is equal to 21 %. Within the last six hours of preheating (phases 11-14), while the heating rate increases rapidly, the oxygen content in the exhaust gas decreases and at the end reaches six mole percent.

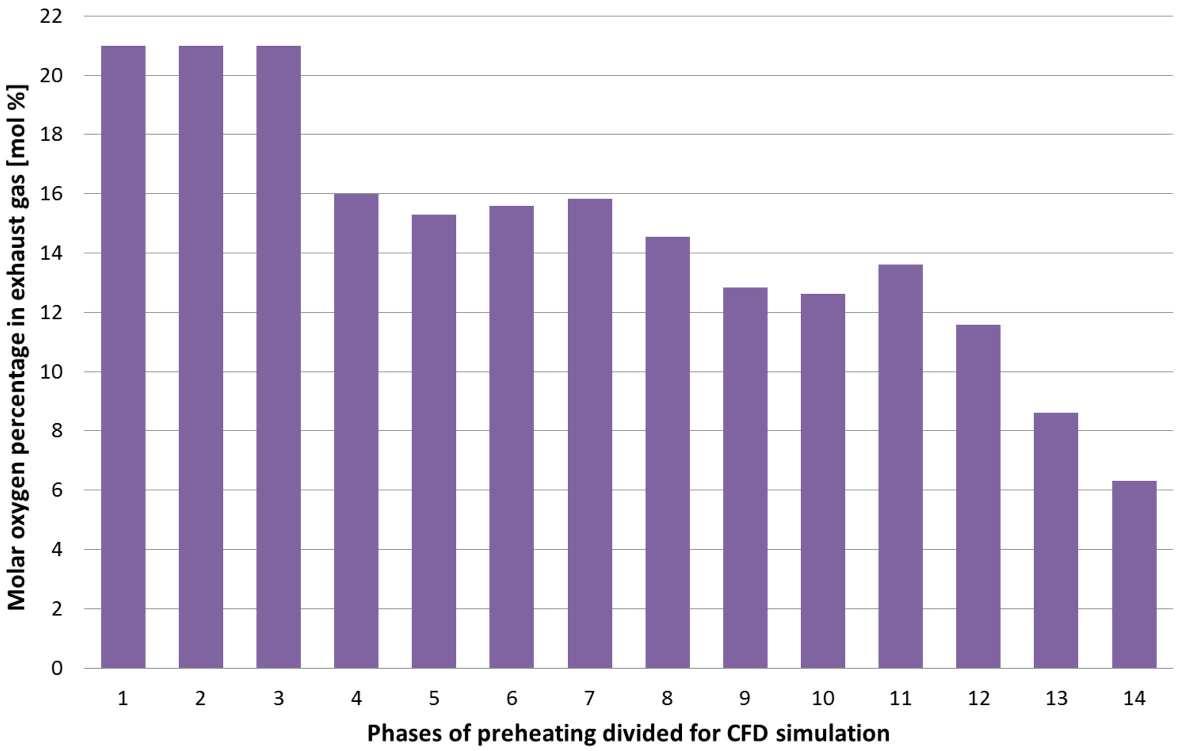

Fig. 53: Calculated mole percentage of oxygen in exhaust gas during ladle preheating in different phases defined for CFD simulation (see Tab. 8)

4.6.5 Meaning of the simulation results for carbon burnout in MgO-C

Based on the preheating simulation shown above, MgO-C refractory decarburization could be predicted. From the CFD calculation results the necessary data like temperature distribution in the lining, gas temperature distribution and gas velocity field and gas composition are known.

Considering the possible carbon burnout in the MgO-C refractory, especially the preheating periods with a lining temperature exceeding 800 °C are of interest. According to the CFD simulation those temperatures occur after 35 h of preheating at the refractory surface and 2 h later also at the cold end of the refractory. The oxygen mass fraction is located between 6 and 12 % within these periods of interest. The calculated gas temperatures in the flame reach about 1700 – 1900 °C. At lower heating rates the flame is short, and a high temperature field concentrates in a region just below the burner. At higher flow rates the flame is longer and the hot gas stream reaches the ladle bottom. The gas flow in region of MgO-C refractory presents no regular pattern. Due to ladle geometry, a circulation develops and the gas velocity vectors show vertical flow with negative direction. The velocity at the slag bath area is in range of 0.1-2 m/s.

5 A model for prediction of carbon burnout in a MgO-C refractory

The aim of this work is to define the possible carbon burnout in the MgO-C lining during steel ladle preheating. In Section 2.2, reaction kinetics of carbon burnout was presented, with three limiting factors: diffusion coefficient, mass transfer coefficient and chemical reaction rate coefficient. In Chapter 3, the determination of diffusion and mass transfer coefficients was described. Within Chapter 4 the operating conditions during steel ladle preheating according to the CFD simulation results were described. In this Chapter a prediction model for the carbon burnout will be presented. The flow chart shown in Fig. 54 gives an overview of the procedure.

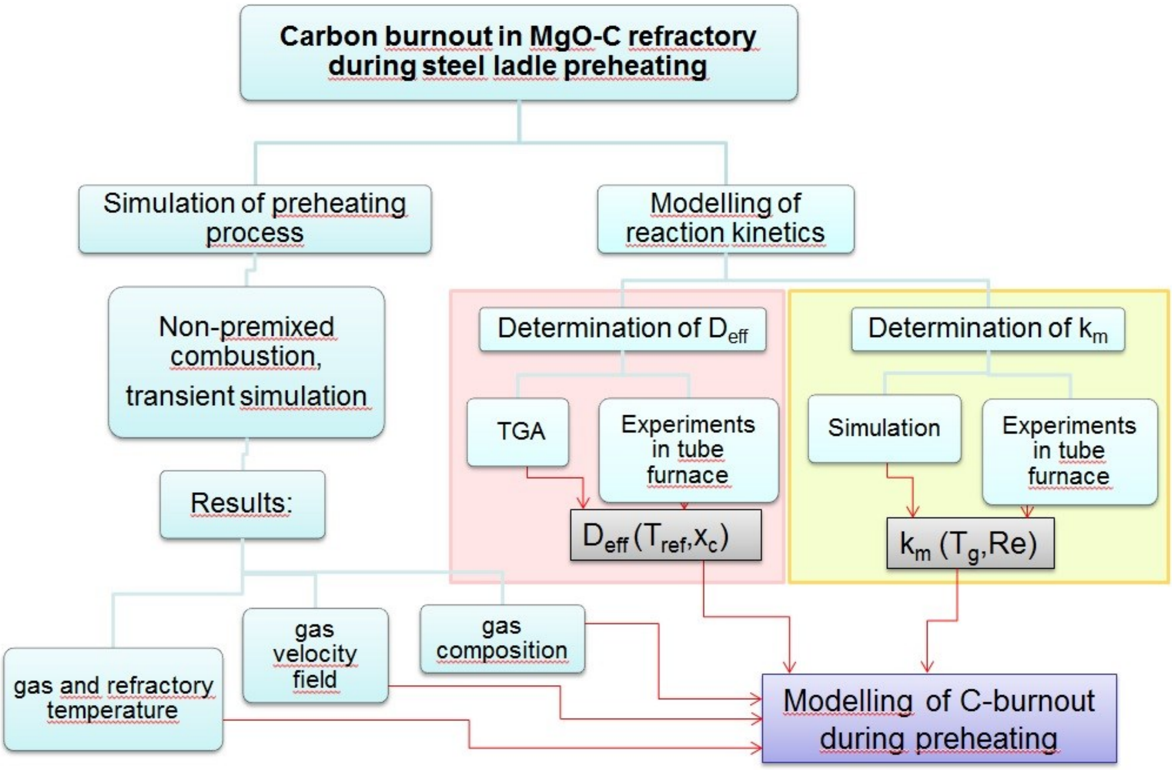

Fig. 54: Flow chart illustrating the procedure chosen for simulation of carbon burnout

For the calculation of decarburization depth, L, in MgO-C refractories during ladle preheating ordinary differential equation Eq. (18) was solved with an explicit Euler method as presented in Eq. (45).

$$L(t+\Delta t) = L(t) + \Delta t \cdot \frac{2}{C^{(C)}} \frac{C_b^{(O_2)}(t)}{\frac{L(t)}{D_{eff}(t)} + \frac{1}{k_m} + \frac{1}{k_c(t)}} \qquad (45).$$

The chosen time step Δt was set to 10 s after examination of sensitivity of the calculation results on the time step size. It was assumed that the temperature change within the first centimeter of the lining is negligible and the temperature was set as a function of time which was determined by the ladle preheating simulation results (Section 4.6.2). According to the lining temperature the diffusion coefficient and rate coefficient of heterogonous chemical reaction were determined, as well as concentration of oxygen in the gas.

5.1 Process parameters and input data

As it was described in Section 4.1, steel ladle preheating is a long process, where the operating conditions are changing with time. The temperature measured at the ladle bottom regulates the heating rate of the burner and thereby influences the oxygen content in the exhaust gas. In Fig. 55 the important parameters for carbon burnout in MgO-C refractory during ladle preheating are represented: the volume percentage of the oxygen in the exhaust gas and the MgO-C lining temperature. The gas temperature near the MgO-C wall region influences the oxygen partial pressure, so it has to be considered in the calculation. Based on CFD simulation results, the gas temperature close to the wall is about 30 °C higher then lining temperature.

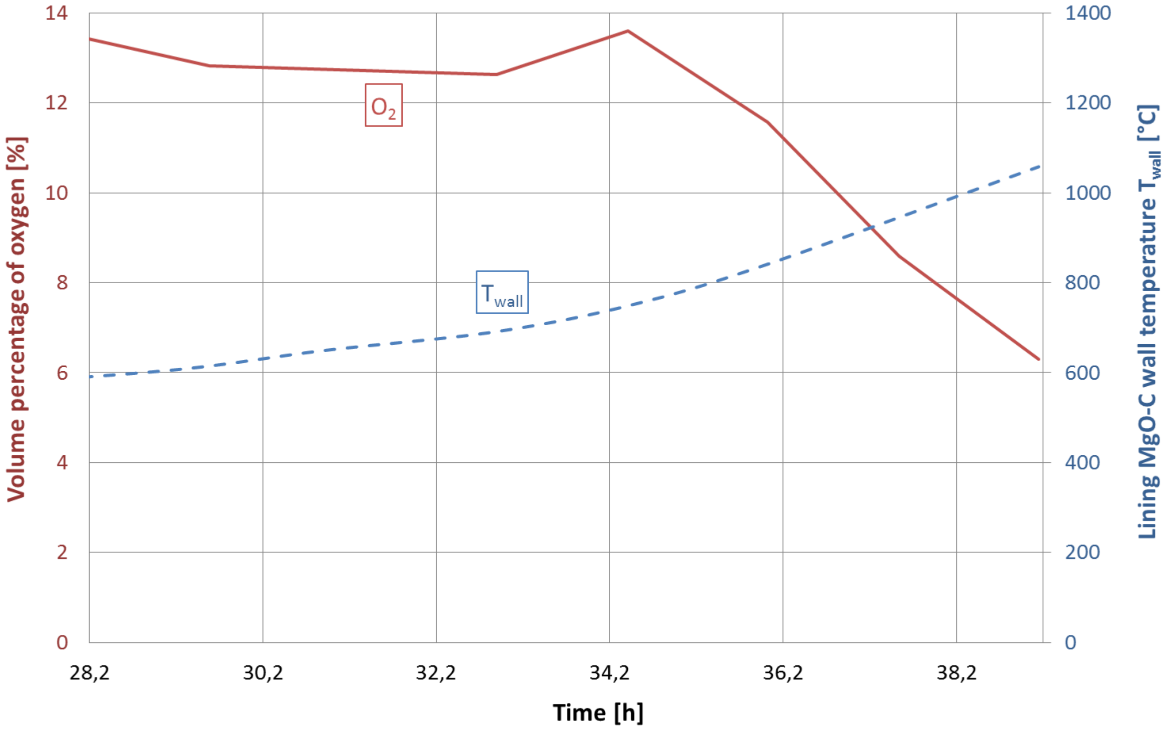

Fig. 55: Operating conditions within last 10 h of steel ladle preheating: MgO-C lining wall temperature and volume percent of oxygen in exhaust gas, according to CFD simulation results

Further data required for prediction of carbon burnout in the MgO-C refractory is the flow characteristic, necessary for mass transfer coefficient calculation. The gas flow in the ladle was presented in Section 4.6.1. According to the CFD simulation no characteristic flow pattern was found close to MgO-C lining, but for the purpose of this work it was assumed, that it could be similar to a flow along a plate. The gas velocities in distance of 1 cm varied between 0.1-2.0 m/s (see Fig. 43). To calculate the mass transfer coefficient, Eq. (25) was applied, there, the Sherwood number was defined with a correlation of dimensionless variables for a laminar flow over a plate according to [58]:

$$Sh_{lam,pl} = 0.664 \cdot \mathrm{Re}^{1/2} \cdot Sc^{1/3} \qquad (46).$$

The characteristic length in Eq. (25) plays the role of the plate length according to [58]. Because of the ladle geometry two options could be considered: the whole length of the MgO-C lining, equal to 1.6 m, as well as the length of the most exposed part of the MgO-C, equal to 0.5m (see Fig. 47). In Fig. 56 the calculated mass transfer coefficients depending on the velocity and the characteristic length are presented. The red curve represents the calculation of k_m in dependence of L_{char} and constant v_g equal to 1 m/s; the blue curve represents the calculation of k_m in dependence of v_g and constant L_{char} equal to 1 m. The temperature was set to 1227 °C for both cases. The achieved k_m values are located in the range of 0.003 – 0.014 m/s.

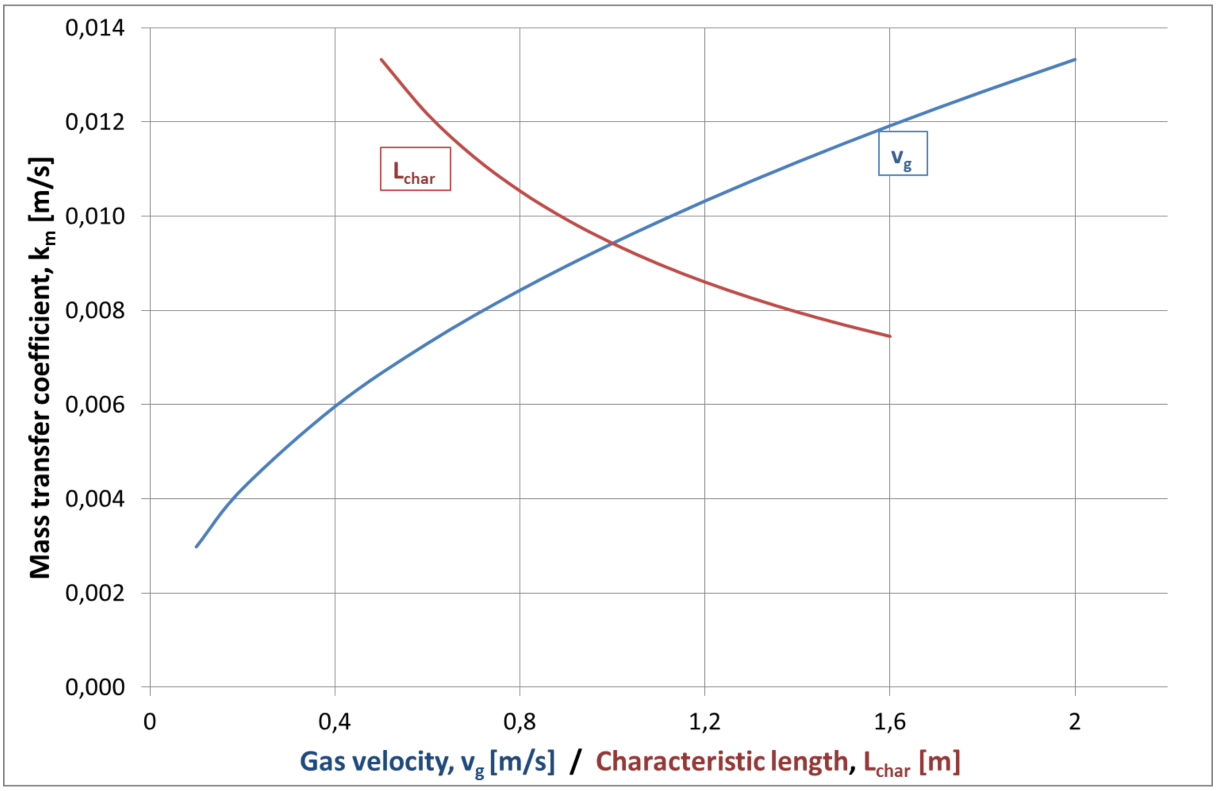

Fig. 56: Mass transfer coefficient in dependence on gas velocity and characteristic length

5.2 Parameter study

It was shown in Section 4.6.1 and 5.1 that it is not possible to define a single mass transfer coefficient for the whole MgO-C lining region, as the gas velocity changes within it. To investigate the effect of the mass transfer coefficient on the decarburization depth a parameter study was conducted and compared with a second one revealing the impact of the oxygen content.

In the first parameter study 0.005, 0.01 and 0.015 m/s, respectively, were substituted for the mass transfer coefficient. The oxygen volume percentage was 10%. The calculation was started at 28.2 h of preheating, when the lining reached 600 °C.

In the second parameter oxygen volume percent of 5, 10 and 15 % and 21 %, respectively, was considered. The mass transfer coefficient was set to 0.01 m/s.

A comparison of both factors influencing carbon burnout in the MgO-C refractory material is shown in Fig. 57. There, the decarbonized layer at the end of preheating is represented in dependence of the oxygen volume content in the exhaust gas (blue curve) or the mass transfer coefficient (red curve), respectively. The dependence of the decarburization depth on the oxygen content is nearly linear, while it shows a decreasing slope with rising mass transfer coefficient. Within this parameter study the depth of the decarburized layer changed about 30% in dependence of the mass transfer coefficient, whereas the impact of different oxygen contents is much higher.

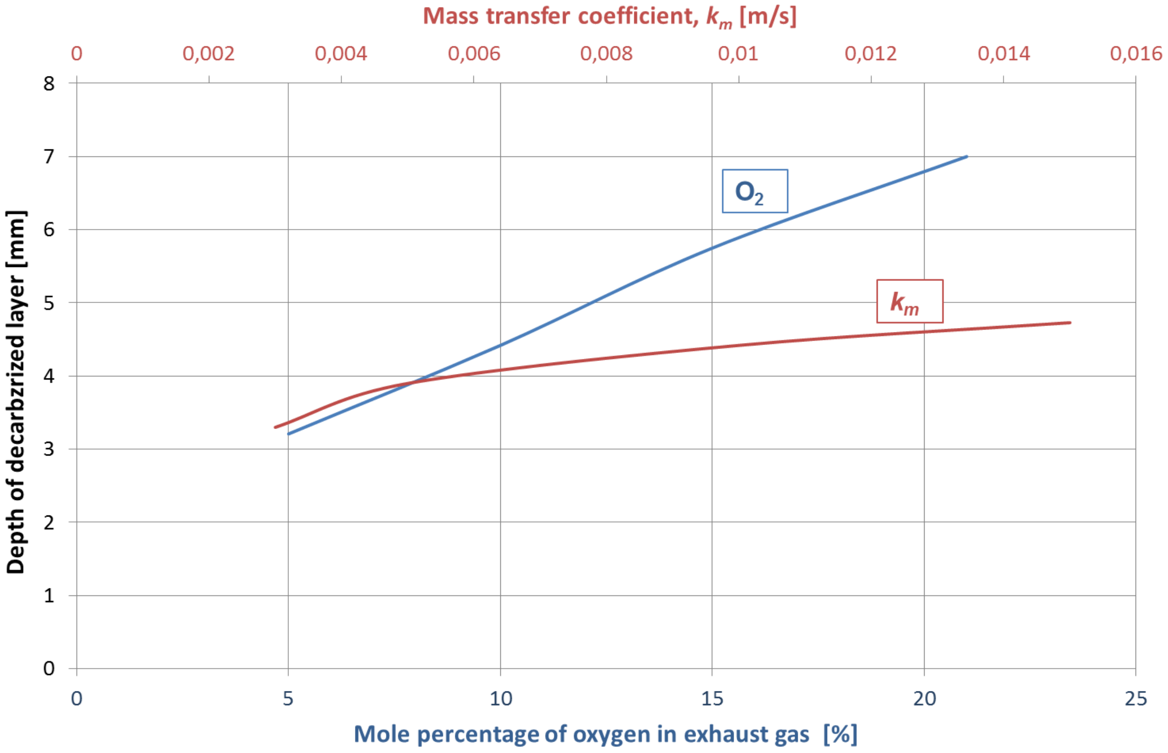

Fig. 57: Comparison of two parameters influencing the depth of decarburized layer in MgO-C refractory

5.3 Calculated carbon burnout in MgO-C refractory during preheating

The calculation of carbon burnout in the MgO-C refractory during preheating of a given steel ladle was carried out based on the lining wall temperature curve presented in Fig. 55. The oxygen mole fraction was set as a function of time also shown in Fig. 55. Gas temperature was chosen 30 °C larger than the wall temperature. The mass transfer coefficient was set to a constant value of 0.01 m/s. The calculation was started at the 28th hour of preheating, after the lining wall reached 600 °C. This temperature was chosen based on the research done for graphite kinetics (see Section 2.2.2), in which the lowest tested temperatures for graphite oxidation were carried out at 600 °C. Also, the oxidation tests, described in Section 3.4, have shown an only minor carbon burnout at 600 °C.

Since there are various data concerning graphite and carbon oxidation rate coefficients, several program runs were executed to compare the kinetics of chemical reaction rate coefficient on the burnout. In addition, the case with infinite chemical reaction rate, also referred as no chemical resistance here, was concerned as it is a common assumption in literature [12], [13], [30]. The results are presented in Fig. 58.

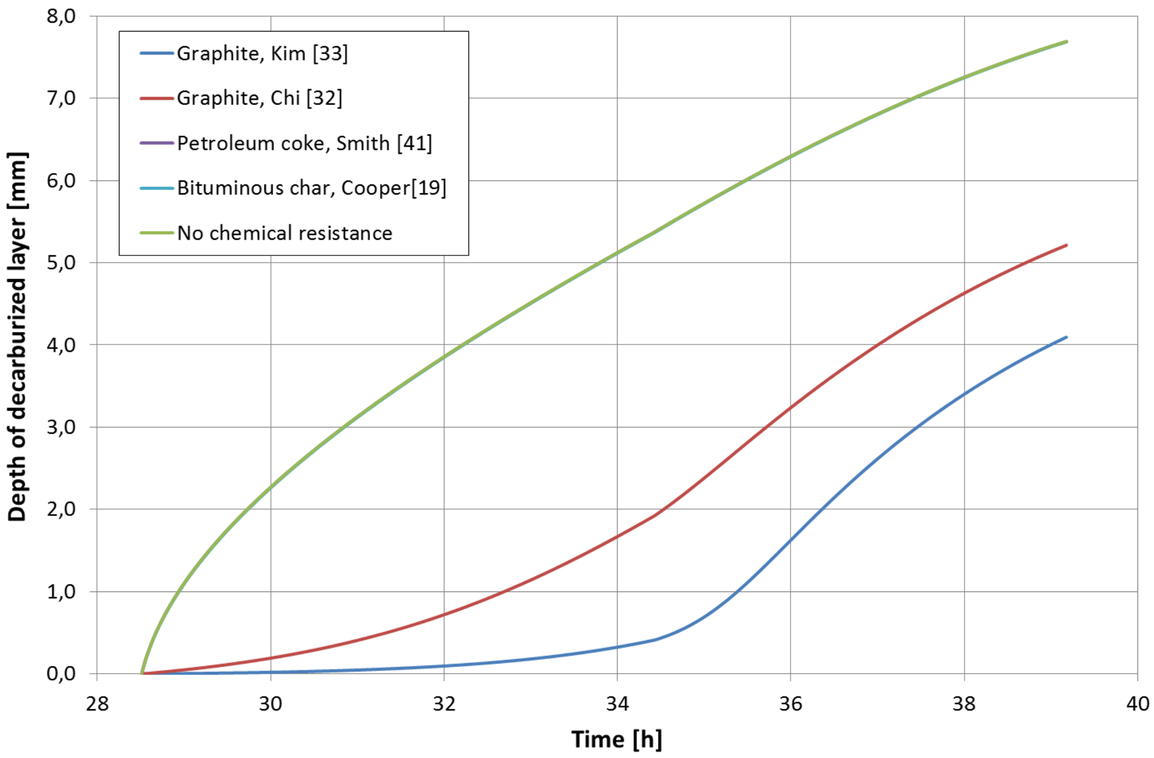

Fig. 58: Change of the decarburized layer depth during steel ladle preheating for MgO-C refractory material M3 with carbon kinetics according to various investigations [19], [32], [33], [41] and also without considering oxidation rate coefficient. The curves presenting carbon oxidation with kinetics proposed in [19] and [41] show the same shape as the curve calculated without chemical resistance. The start temperature for carbon burnout was set to 600 °C

In Fig. 58 the lowest decarburization depth of 4mm is reached with the application of the graphite oxidation kinetics proposed by Kim [33]. Reaction rate coefficients determined by Chi [32] are designated for a temperature range between 600 – 800 °C. Carbon burnout in this case is about one millimeter larger than using Kim's kinetics. The curves presenting carbon oxidation with applied kinetics intended for coke or char are about 150 – 200 % larger than those with graphite oxidation kinetics. They show the same shape as the curve calculated without chemical resistance. They reach a decarburized depth of nearly 8 mm. The calculated results showed that the chemical resistance in the case of applying kinetics for char or coke is not the limiting factor of oxidation kinetics in the temperature region of this calculation.

The amount of the carbon coming from the binder is only about 1-3 mass percent. For further calculation, the oxidation kinetics proposed by Chi [32] or Kim [33] were applied as the graphite constitutes 75 – 90 % wt of the whole carbon comprised in the sample (the actual percentage depends on the MgO-C refractory material).

The decision to start calculations at a temperature of 600 °C is not mandatory as there is also carbon derived from the pitch or resin binder. Therefore, a calculation was executed starting at 400 °C and the results are presented in Fig. 59.

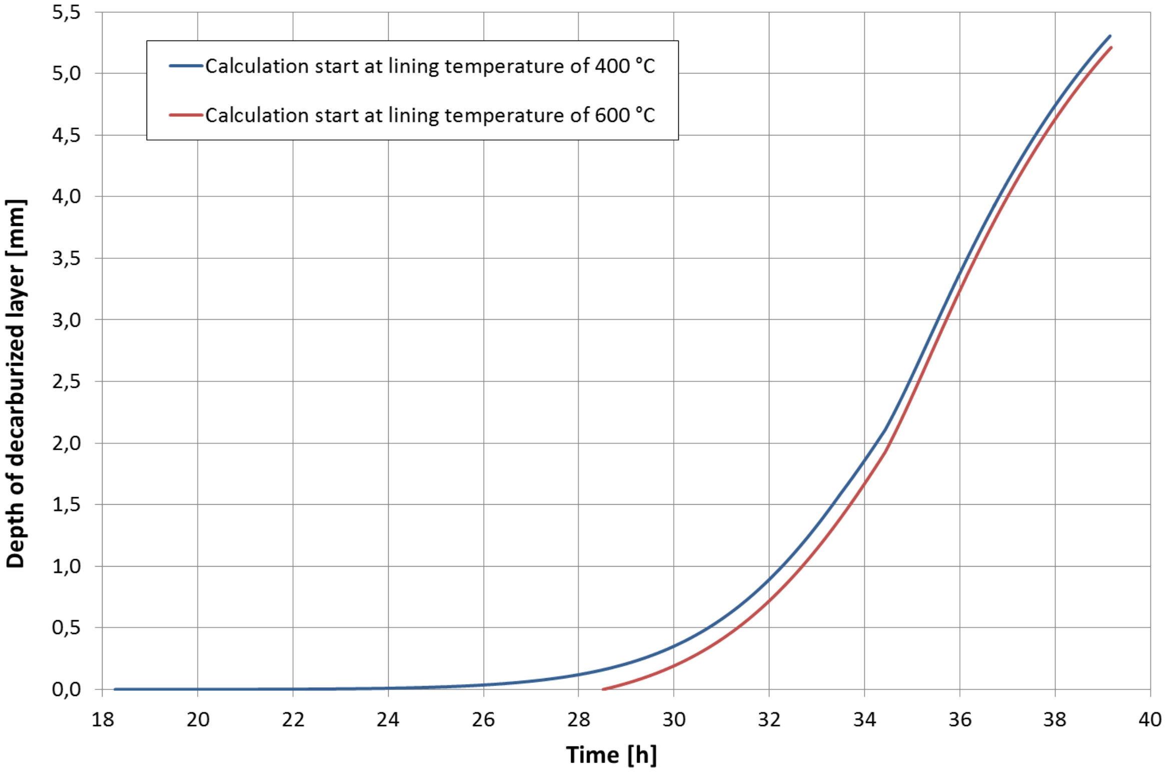

Fig. 59: Change of the decarburized layer depth during steel ladle preheating for MgO-C refractory material M3 with graphite kinetics proposed by Chi [32]. For the red curve the calculation was started at lining temperature of 600 °C, for the blue curve at 400 °C

The decarburization during the time where the lining temperature rises from 400 °C up to a temperature of 600 °C achieves 0.15 mm depth. From that point – the 28th hour of preheating – onwards the second calculation is started. After 34 h both the curves get closer to each other and at the end of preheating the difference between the oxidized depths is only 0.1 mm. At 26th the lining temperature reaches 550 °C. The comparison presented in Fig. 60 shows that overall calculated carbon burnout is similar for both cases; therefore further carbon burnout simulation will be started at a lining temperature of 600 °C.

The results for the calculation of carbon burnout for various MgO-C refractory materials with application of chemical reaction rate coefficient proposed by Chi [32] are presented in Fig. 60.

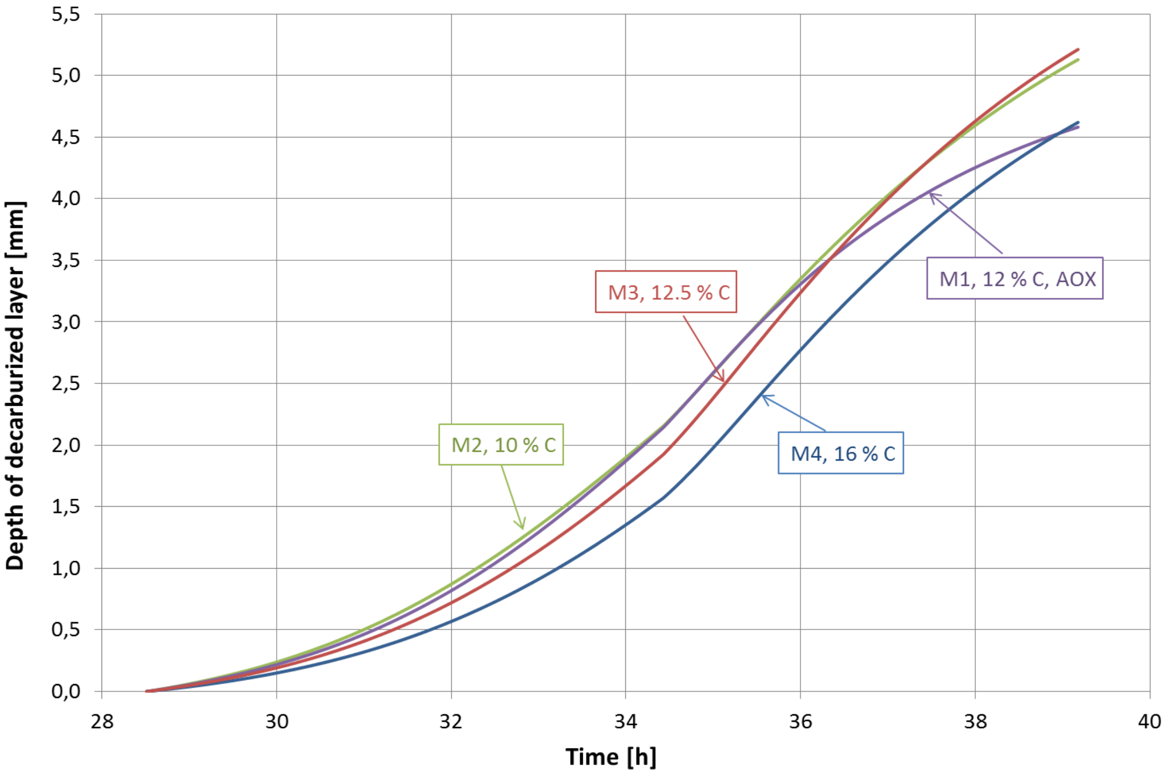

Fig. 60: Change of the decarburized layer depth for various MgO-C refractory materials during steel ladle preheating. The starting temperature for carbon burnout was set to 600 °C. Oxidation kinetics from Chi presented in [32] has been applied

At the end of preheating, the lowest decarburized depth of 4.5 mm occurs in refractory material M1 and M4. Until the 37th hour preheating the curve of MgO-C material M1 containing AOXs shows a similar shape as those of materials M2. Afterwards it levels off. This behavior is connected with the effective diffusion coefficient within the refractory, which is temperature independent in the case of material M1. At 37th hour of preheating, the lining reaches the temperature of 800 °C, at which effective diffusion coefficients of all other materials, except M1, increase considerably. Therefore, the application of AOX is reasonable, if the lining operation temperature mostly exceeds 800 °C. The carbon burnout curves of MgO-C materials M2 and M3 are similar and the end depth of decarburized layer slightly exceeds 5 mm.

In Fig. 61 the results for calculation of carbon burnout for various MgO-C refractory materials with the application of chemical reaction rate coefficient proposed by Kim [33] are presented.

The decarburization depth calculated with the oxidation kinetics coming from Kim is ca. 1 mm less than in the case of the kinetics proposed by Chi [32]. The curves presented in Fig. 61 show a relatively small slope until the 34th hour of preheating. At that time, the wall temperature equals 800 °C (see Fig. 55) and the oxidized depth reaches approximately 0.3 – 0.4 mm for all of the refractory materials investigated. Afterwards, the slope becomes steeper for all materials, however refractory M4 shows the highest oxidation resistance. Similarly as for the kinetics of Chi, material M1 reveals better oxidation resistance at temperatures above 900 °C and at the end of preheating the decarburized depth equals to 3.4 mm. The oxidation depth in case of material M4 is equal to 3.6 mm and for materials M2 and M3, which show nearly identical behavior, this value is 4.1 mm.

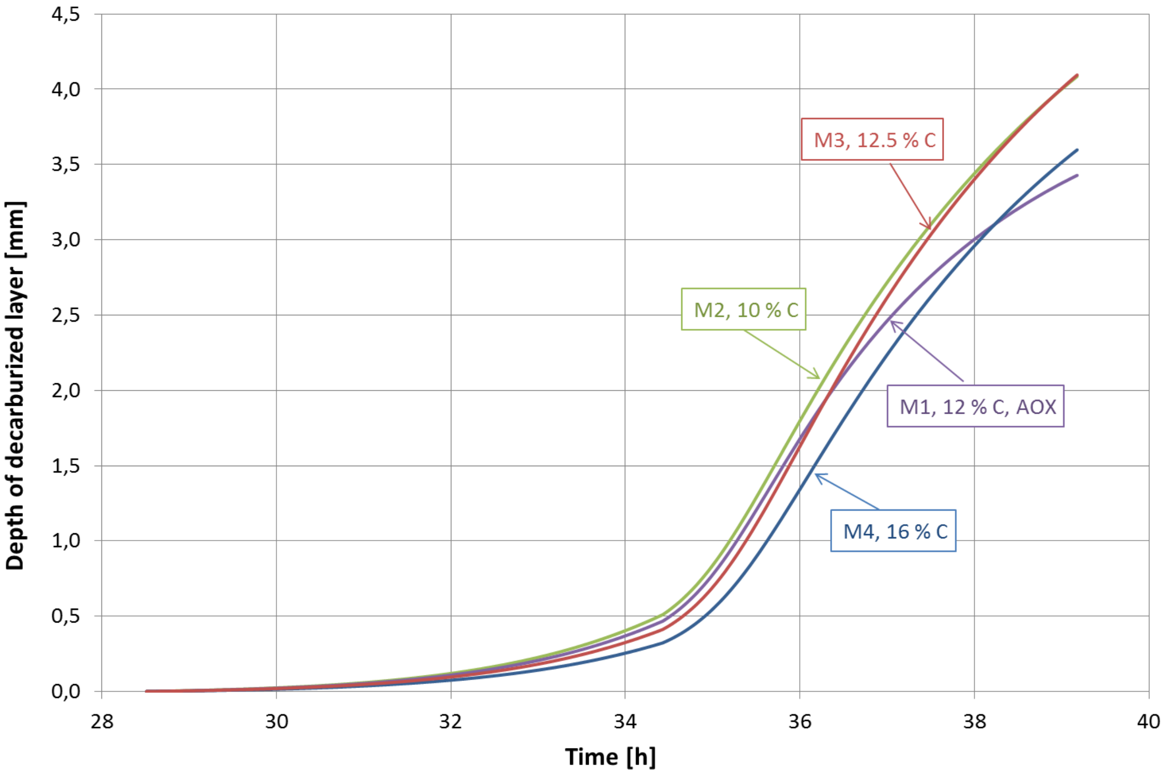

Fig. 61: Change of the decarburized layer depth for various MgO-C refractory materials during steel ladle preheating. The starting temperature for carbon burnout was set to 600 °C. Oxidation kinetics from Kim presented in [33] has been applied

In Section 5.1, it was discussed, that the mass transfer coefficient of oxygen at the MgO-C refractory surface is not at a constant value, but varies in the range between 0.004 – 0.015 m/s. In Fig. 62 the calculation results of carbon burnout during ladle preheating for material M3 are presented, whereupon different mass transfer coefficient values were applied. The difference of the decarburized depth between the calculation with the mass transfer coefficient of 0.015 m/s and that of 0.003 m/s is about two millimeters.

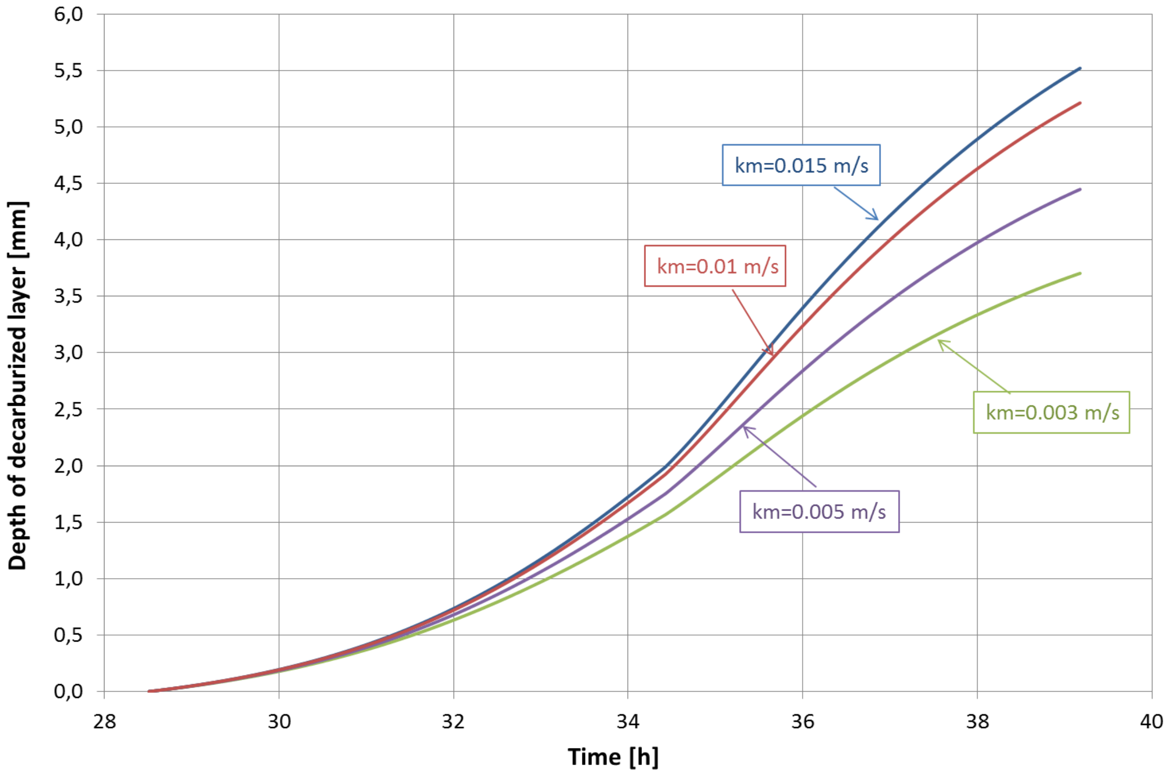

Fig. 62: Change of the decarburized layer depth for MgO-C refractory material M3 during steel ladle preheating considering various mass transfer coefficients. The starting temperature for carbon burnout has been set to 600 °C. Oxidation kinetics from Chi [32] has been applied

According to conducted calculations, carbon burnout in the MgO-C refractory depends strongly on the oxygen content in the exhaust gas and the lining temperature. The mass transfer coefficient also has an impact; it can change the depth of oxidized layer of 30 – 35 % (two millimeters). Great differences in the depth of the decarburized layer occur depending on the applied carbon oxidation kinetics. Oxidation reaction rates for char or coke do not represent the limiting mechanism, the chemical reaction rate k_c in this case presents no additional decisive resistance for the general oxidation kinetics. On the contrary, kinetics for graphite oxidation show strong dependence on the temperature, and decrease at low temperatures to a value decisive for the oxidation process. Therefore the burnout progress is in this case retarded at the lower lining temperatures. This is especially valid below 800 °C – from that point onwards the oxidation rate increases considerably. The same behavior has been observed by oxidation tests (see Section 3.4). Refractory materials M1 and M4 showed the best oxidation resistance; however, M1 improves this property considerably at temperature higher than 900 °C.

6 Conclusion and possible further procedure

The aim of this work was to analyze the impact of steel ladle preheating on the possible decarburization of MgO-C refractory bricks applied in the slag bath area of the ladle lining. This study comprises two sub-goals:

a) To establish a kinetic model for carbon burnout in MgO-C refractories and evaluate it at a laboratory scale.

b) To simulate steel ladle preheating via computational fluid dynamics (CFD).

Aided by the kinetic model and the data obtained from the CFD simulation such as lining temperature and oxygen concentration, a prediction model for carbon burnout in MgO-C refractory during preheating of the steel ladle was developed.

6.1 Kinetic model for carbon burnout and its experimental evaluation

It can be assumed, that the carbon burnout in MgO-C refractory material is mainly caused by the direct oxidation of carbon to carbon monoxide:

$$2C(s) + O_2(g) \rightarrow 2CO(g).$$

The kinetic model of carbon burnout was based on the shrinking core model with three resistances: mass transfer of oxygen from the gas bulk at the refractory surface, effective diffusion of oxygen in the refractory pores and chemical reaction of oxygen with the carbon. The rate of carbon oxidation in terms of the molar flux density (moles per second and square meter) is described with following equation:

$$j_R^C = \frac{2 \cdot C_b^{O_2}}{\frac{L}{D_{eff}} + \frac{1}{k_m} + \frac{1}{k_c}}.$$

The effective diffusion coefficient D_{eff} was determined for various MgO-C refractory materials by thermogravimetric analysis. Received values showed dependence on the temperature of the sample, with exception of the resin bonded MgO-C refractory material M1, which contained antioxidants (AOXs). The second factor influencing D_{eff} was the carbon content of the material. The diffusion coefficient of resin bonded material M2 with carbon content of 10.5% at 1000 °C equaled 10.8 cm^2/min; in the case of pitch bonded material M3 with 12.5% carbon it was equal to 15.7 cm^2/min. At the same temperature D_{eff} for the material M1 containing 11% carbon was equal to 5.1 cm^2/min and for the material M4 with 16% carbon – 16.2 cm^2/min. The activation energies of calculated diffusivities were in the range of 24 kJ/mol and agreed with corresponding values found in the literature.

The mass transfer coefficient k_m was described by relations of the dimensionless variables Sherwood number, Reynold's number and Schmidt number.

The chemical rate coefficient of carbon oxidation k_c was defined based on the Arrhenius relation based on the literature studies. The parameters for the relation varied depending on the carbon sources: graphite oxidation showed strong dependence on the temperature, whereas petroleum or char carbon were temperature independent.

Two types of oxidation tests have been carried out in a tube furnace. The intention of oxidation experiments of pure graphite was to determine the mass transfer coefficient k_m at various air flow rates and to compare it with the values calculated from CFD simulation data. The goal was achieved: the maximal experimental values agreed with those calculated for flow rates 5.3, 7.7 and 10.3 Nl/min and were 10 and 20 % greater for flow rates of 2.7 and 1.8 Nl/min, respectively.

Oxidation tests with MgO-C samples were planned in order to validate the carbon burnout kinetic model. The samples were heated up in a tube furnace to a present temperature in an inert atmosphere and afterwards air was purged through the tube with a given flow rate. The rate of oxidized carbon was determined by the carbon monoxide and carbon dioxide contents of the exhaust gas. The samples were tested at 600 700, 800, 900, 1000 °C. The carbon conversion differed depending on the temperature, whereas a significant change in oxidation kinetics was noticed between 700 and 800 °C. The applied air flow rate during the experiment had a negligible influence on the decarburization depth of the MgO-C refractory.

Parallel to the experiments, the carbon burnout was calculated using proposed kinetic model. The decarburization depths computed using graphite oxidation kinetics proposed by Chi in [32] were about 20 – 30 % greater than experimental values. Applying the graphite kinetics proposed by Kim [33], there was no carbon burnout at 600 °C and the calculated values for 700 °C were about 40 % less than the experimental ones. For the temperature of 800 °C, the calculated curve fitted the experiment with ca. 95 % accuracy. The calculated values at 1000 °C were the same as in the case of kinetics proposed by Chi, at 900 °C they were slightly less. The calculations done with oxidation kinetics designated for char or petroleum coke gave the same decarburization depth values as without considering the chemical resistance at all. However, for all temperatures below 900 °C, the calculated values were much larger than the experimental ones and also larger in comparison with calculations also considering graphite kinetics. Based on own conducted experimental data compared with theoretical results, the graphite kinetics has to be considered for the calculation of carbon burnout in MgO-C refractory material at temperatures lower than 900 °C.

According to the experimental data, effective diffusion coefficients were also determined for 1000 °C at various air flow rates. The achieved values were about 10 cm^2/min for all flow rates, except 2.7 Nl/min, where D_{eff} equaled 13.5 cm^2/min. These values were less than those determined by TGA, which equaled 16 cm^2/min. To clarify the difference, more detailed experimental work would have to be done and the experimental setup should be improved. Proposed improvements should comprise gas temperature and velocity measurements in the tube and considering the size of the gas-solid contact surface.

6.2 CFD simulation of ladle preheating

The second goal of the thesis was the simulation of the preheating process. The computations were executed with ANSYS Fluent as a transient simulation. The heat release from gas combustion and the exhaust gas composition were calculated with a non-premixed approach. Additionally, the laminar flamelet concept which considers the local flame stretching and its further effect on conversion rate was used. The combustion kinetics and the species transport were described with a 41-reaction mechanism for methane combustion proposed by Correa [93]. The convective heat transfer at the ladle lining walls was solved using the standard wall functions in ANSYS Fluent software, which are available within the realizable k-ε turbulence model. The radiative heat exchange was described by a Discrete Ordinates model [87].

Based on numerical calculations the prediction of the MgO-C refractory decarburization depth during ladle preheating was executed. Considering the possible carbon burnout, the part of the preheating period where the lining temperature exceeds 800 °C was of interest. According to the CFD simulation results those temperatures occur after 35 hours of preheating at the refractory surface. The oxygen molar percentage is between 6 and 12 % within that period. The mass transfer coefficient determined with a power relation of dimensionless variables for the laminar flow over a plate together with simulation results was in the range of 0.003 – 0.015 m/s.

6.3 Prediction of carbon burnout during ladle preheating

For the calculation of decarburization depth in MgO-C refractory during ladle preheating ordinary differential equation Eq. (18) was solved. As a numerical method an explicit Euler method was chosen. It was assumed that the temperature change within the first centimeter of the lining is negligible and the temperature was set as a function of time. In the prediction model various kinetic parameters for chemical rate coefficient k_c were applied. The depth of decarburized layer at the end of preheating was in the range between 3 and 5.5 mm depending on the analyzed MgO-C refractory material, applied mass transfer coefficient k_m and used chemical rate coefficient k_c.

According to conducted studies, carbon burnout in MgO-C refractory depends mainly on the oxygen content in the exhaust gas and the lining temperature. The impact of the mass transfer coefficient is smaller. Significant differences of the decarburized layer depth occur depending on the applied chemical rate coefficient k_c for carbon oxidation kinetics. Oxidation kinetics for char or coke does not decelerate the oxidation process as opposed to the kinetics for graphite oxidation proposed by Chi [32] or Kim [33]. The carbon burnout progress in this case is retarded at lower lining temperatures. This is especially the case for temperatures below 800 °C – from that point the conversion rate increases considerably. The decarburization depths calculated with graphite oxidation kinetics proposed by Chi [32] are in the range between 4 and 5 mm, and 3 to 4 mm in the case of kinetics defined by Kim [33]. Using kinetics defined for char or petroleum oxidation, the oxidized depth is about 8 mm and is equal to that one calculated without consideration of chemical resistance.

The resin bonded refractory material M1 containing 11 % of carbon and the pitch bonded material M4 containing 16 % of carbon showed the best oxidation resistance. However, material M1, which contains antioxidants, improves this property considerably at temperatures higher than 900 °C. This behavior is connected with the effective diffusion coefficient within the refractory, which in the case of material M1 is temperature independent. The carbon burnout curves of MgO-C materials M2 and M3 are very similar.

6.4 Possible further procedure

The model proposed for carbon burnout kinetics in MgO-C refractories was accurate enough for the purpose of this work: the estimation of decarburization depth in the MgO-C refractory lining during steel ladle preheating. However, for further investigations, the proposed model should be reviewed considering the influence of the convective mass transfer on the carbon oxidation rate. Also, the oxidation tests described in this work should have better parameter control to become a standardized testing procedure.

To protect MgO-C refractory lining from carbon burnout during steel ladle preheating the oxygen content in the exhaust gas should be kept at the possible lowest level. Also, periods when the lining temperature exceeds 800 °C in presence of oxidizing atmosphere should be as short as possible. Further investigation of carbon burnout via other reactions, like e.g. Boudouard reaction, in MgO-C refractories would be of interest, as well as a detailed study of the oxidation kinetics at lower temperatures.

7 Literature

[1] Schacht C.A.: Refractories Handbook. Testing of Refractory Materials, Marcel Dekker, Inc., New York, Basel (2004)

[2] Riedel R., Chen I.-W.: Ceramics science and technology. Volume 2: Properties., Wiley-VCH Verlag, Weinheim (2010)

[3] Feuerfestbau: Stoffe - Konstruktion - Ausführung. 2. Auflage, Deutsche Gesellschaft Feuerfest- und Schornsteinbau, Vulkan-Verlag Classen (1994)

[4] Telle R.: Keramik. 7., vollständig neubearbeitete und erweiterte Auflage, Springer Verlag, Berlin (2007)

[5] Routschka G.: Taschenbuch Feuerfeste Werkstoffe. 3 Auflage, Vulkanverlag Essen, (2001)

[6] Singh J. P., Banerjee S.: Microstructure and properties of refractories, Trans Tech Publ. (1993)

[7] Rand B., Ahmed A. S., Ramos V. P. S.: The Role of Carbon in Refractories, Tehran International Conference on Refractories, 4-6 May 2004 (2004)

[8] Aneziris C., Hubalkova J., Barabas R.: Microstructure evaluation of MgO-C refractories with TiO_2- and Al-additions, Journal of the European Ceramic Society, vol. 27, no. 1, pp. 73-78 (2007)

[9] Schulle W., Ulbricht J.: Influence of different carbonaceous binders on the properties of refractories, Boletín de la Sociedad Española de Cerámica y Vidrio, vol. 31, no. 5, pp. 419-425 (1992)

[10] Buchebner G., Samm V., Rotsch J.: Latest developments in Magnesia-Carbon Bricks, RHI Bulletin, no. 1, pp. 23-28 (2011)

[11] Buchebner G., Sampayo L., Samm V.: Neuentwicklung kohlenstoffgebundener Magnesiakohlenstoffsteine unter dem Aspekt der verbesserten Umweltverträglichkeit, Berg- und Hüttenmännische Monatshefte, vol. 149, no. 9, pp. 317-321 (2004)

[12] Li X., Rigaud M., Palco S.: Oxidation Kinetics of Graphite Phase in Magnesia-Carbon Refractories, Journal of the American Ceramic Society, vol. 78, no. 4, pp. 965-971 (1995)

[13] Faghihi-Sani M.-A., Yamaguchi A.: Oxidation kinetics of MgO-C refractory bricks, Ceramics International, vol. 28, no. 8, pp. 835-839 (2002)

[14] Leonard R. J., Herron R. H., Significance of Oxidation-Reduction Reactions Within BOF Refractories, Journal of the American Ceramic Society, vol. 55, no. 1, pp. 1-6 (1972)

[15] Ghosh N. K., Ghosh D. N., Jagannathan K. P.: Oxidation mechanism of MgO–C in air at various temperatures, British Ceramic Transactions, vol. 99, no. 3, pp. 124-128 (2000)

[16] Buchebner G., Hanna A., Hochegger M., Zettl K.-M.: Latest developments in Magnesia-Carbon Bricks for modern Electrical Arc Furnaces, RHI Bulletin, no. 1 (2014)

[17] Smoot L. D., Smith P. J.: Coal combustion and gasification, Planum Press, New York and London (1985)

[18] Gupta P., Sadhukhan A. K., Saha R. K.: Analysis of the combustion reaction of carbon and lignite char with ignition and extinction phenomena: Shrinking sphere model, International Journal of Chemical Kinetics, vol. 39, no. 6, pp. 307-319 (2007)

[19] Cooper J., Hallett W.: A numerical model for packed-bed combustion of char particles, Chemical Engineering Science, vol. 55, pp. 4451-4460 (2000)

[20] Chejne F., Hernandez J. P.: Modelling and simulation of coal gasification process in fluidised bed, Fuel, vol. 81, no. 13, pp. 1687-1702 (2002)

[21] Biba V., Malecha J., Macak J., Klose E.: Mathematical model for coal gasification under pressure, Industrial and Engineering Chemistry Process Design and Development, vol. 17, no.1, pp. 92-98 (1978)

[22] Miessen G.: Simulation der Koksverbrennung unter Verwendung detaillierter Reaktionsmechanismen, Doctoral Thesis, Naturwissenschaftlich-Mathematische Gesamtfakultät, Universität Heidelberg (2000)

[23] Bews I., Hayhurst A., Richardson S., Taylor S.: The order, Arrhenius parameters, and mechanism of the reaction between gaseous oxygen and solid carbon, Combustion and Flame, vol. 124, no. 1-2, pp. 231-245 (2001)

[24] Levenspiel O.: Chemical reaction engineering. Third Edition., Wiley, New York (1999)

[25] Fogler H.: Elements of Chemical Reaction Engineering. Third Edition, Pearson Education Limited, New Jersey (1999)

[26] Joos F.: Technische Verbrennung. Verbrennungstechnik, Verbrennungsmodellierung, Emissionen, Springer Verlag, Berlin (2006)

[27] Yagi S., Kunii D., Fluidized-solids reactors with continuous solids feed: Residence time of particles in fluidized beds, Chemical Engineering Science, vol. 16, no. 3-4, pp. 364-371 (1961)

[28] Sadrnezhaad S. K., Mahshid S., Hashemi B., Nemati Z. A.: Oxidation Mechanism of C in MgO–C Refractory Bricks, Journal of the American Ceramic Society, vol. 89, p. 1308–1316 (2006)

[29] Faghihi-Sani M.-A., Yamaguchi A.: Effect of Al and Alumina Additions on Oxidation Rate of MgO-C Refractory, Journal Ceramic Society Japan, vol. 110, no. 8, pp. 699-702 (2002)

[30] Sadrnezhaad S. K., Nemati Z. A., Mahshid S., Hosseini S., Hashemi B.: Effect of Al Antioxidant on the Rate of Oxidation of Carbon in MgO-C Refractory, Journal of the American Ceramic Society, vol. 90, no. 2, pp. 509-515 (2007)

[31] Gray D., Cogoli J. G., Essenhigh R. H.: Problems in Pulverized Coal and Char Combustion, American Chemical Society Advanced Chemical Series, vol. 131, no. 6, pp. 72-91 (1976)

[32] Chi S.-H., Kim G.-C.: Comparison of the oxidation rate and degree of graphitization of selected IG and NBG nuclear graphite grades, Journal of Nuclear Materials, vol. 381, pp. 9-14 (2008)

[33] Kim E. S., No H. C.: Experimental study on the oxidation of nuclear graphite and development of an oxidation model, Journal of Nuclear Materials, vol. 349, no. 1-2, pp. 182-194 (2006)

[34] Fuller E. L., Okoh J. M.: Kinetics and mechanisms of the reaction of air with nuclear grade graphites: IG-110, Journal of Nuclear Materials, vol. 240, no. 3, pp. 241-250 (1997)

[35] Yang H.-C., Eun H.-C., Lee D.-G.,. Jung C.-H, Lee K.-W.: Analysis of Combustion Kinetics of Powdered Nuclear Graphite by using a Non-isothermal Thermogravimetric Method, Journal of Nuclear Science and Technology, vol. 43, no. 11, pp. 1436-1439, (2006)

[36] Hinssen H.-K., Kühn K., Moormann R., Schlägl B., Fechter M., Mitchell M., Oxidation experiments and theoretical examinations on graphite materials relevant for the PBMR, Nuclear Engineering and Design, vol. 238, no. 11, pp. 3018-3025 (2008)

[37] El-Genk. M. S., Tournier J.-M. P, Travis B. W.: Graphite Oxidation Simulation in HTR Accident Conditions - Final and 3rd Year Technical Report, Technical Report No. UNM-ISNPS-1-2012, vol. Institute for Space and Nuclear Power Stud (2012

[38] Rodriguez-Reinoso F., Thrower P. A., Jr Walker P. I.: Kinetic Studies of the Oxidation of Highly Oriented Pyrolytic Graphites, Carbon, vol. 12, pp. 63-70 (1974)

[39] Gelbard F.: Graphite Oxidation Modeling For Application in MELCOR, Sandia National Laboratories Report, 1–43, New Mexico (2009)

[40] Bi J., Luo C., Aoki K.-I., Uemiya S., Kojima T.: A numerical simulation of a jetting fluidized bed coal gasifier, Fuel, vol. 76, no. 4, pp. 285-301 (1997)

[41] Smith I. W.: The Combustion Rates of Coal Chars: a Review, Nineteenth Symposium (International) on Combustion, The Combustion Institute, Pittsburgh, pp. 1045-1065 (1982)

[42] Zoglmeyr G.: Oxidation behavior of carbon containing basic refractories, Radex-Rundschau, vol. Band 2, pp. 382-390 (1984)

[43] Hashemi B., Nemati Z. A., Faghihi-Sani M. -A.: Effects of resin and graphite content on density and oxidation behaviour of MgO-C refractory bricks, Ceramics International, vol. 32, pp. 313-319 (2006)

[44] Gokce A. S., Gurcan C., Ozgen S., Aydin S.: The effect of antioxidants on the oxidation behaviour of magnesia-carbon refractory bricks, Ceramics International, vol. 34, no. 2, pp. 323-330 (2008)

[45] Ichikawa K., Nishio H., Hoshiyam Y.: Oxidation test of MgO-C bricks, Taikabutsu Overseas, vol. 14, no. 1, pp. 13-19 (1994)

[46] Matsui K., Kawano F.: Effect of Impurities in Magnesia on Reaction Between Magnesia Clinker and Carbon, Taikabutsu Overseas, vol. 14, no. 1, pp. 3-12 (1993)

[47] Mukhopadhyay S., Chatterjee S., Ali S., Arvey R.: Study on Oxidation Resistance of Magnesia-Carbon Refractories at Various Temperatures, 2008 AISTech Conference Proceedings (2008)

[48] Bae I., No J., Um C.J., Shin M.: The improvement of casting ladle lining for clean stainless steel production, Proceedings of the UNITECR'07, pp. 186-189 (2007)

[49] Nandy S. K., Ghosh N. K., Das G. C.: Oxidation kinetics of MgO–C in air with varying ash content, Advances in Applied Ceramis, vol. 104, no. 6, pp. 306-311 (2005)

[50] Rief A., Heid S., Höck M.: Effects of Metal Powder Additives on MgO-C Brick Performance, RHI Bulletin, no. 1 (2013)

[51] Volkova O., Scheller P. R., Lychatz B.: Kinetics and Thermodynamics of Carbon Isothermal and Non-isothermal Oxidation in MgO-C Refractory with Different Air Flow, pp. 1-11 (2014)

[52] Liu B., Sun J.-l., Tang G. -S., Liu K. -Q., Li L., Liu Y.-F.: Effects of Nanometer Carbon Black on Performance of Low-Carbon MgO-C Composites, Journal of Iron and Steel Research, International, vol. 17, no. 10, pp. 75-78 (2010)

[53] Hocquet S., Andre S., Erauw P. J., Tirlocq J., Cambier F.: Characteristaion of oxidation phenomena in carbon containing refractory materials for metallurgy, Proceedings of the UNITECR’07, Dresden, Germany (2007)

[54] Zhao S., Mei G., Sun J., Yang W., Xie Z.: Estimation of Effective Diffusion Coefficient of Gaseous Species in MgO-C Refractories by Shrinking Core Model:, ISIJ International, vol. 52, no. 7, pp. 1186-1195 (2012)

[55] Watanabe K., Yabuta K., Okamoto H., Yamamoto H.: Oxidation Behaviour of MgO-C Bricks With Various Additives, UNITECR ’95, Kyoto, Japan (1995)

[56] Baehr H. D., Stephan K.: Wärme- und Stoffübertragung, Springer Verlag, Berlin (2006)

[57] Perry R.: Perry's chemical engineers' handbook. Seventh edition, The McGraw-Hill Companies (1997)

[58] VDI-Wärmeatlas, 10., bearbeitete und erweiterte Auflage, VDI-Gesellschaft Verfahrenstechnik und Chemieingenieurwesen, Springer Verlag, Berlin (2006)

[59] Ghiaasiaan S. M.: Convective heat and mass transfer, Cambridge University Press, (2011)

[60] Bird B., Stewart W. E., Lightfoot E. N.: Transport Phenomena, John Wiley & Sons (2006)

[61] Reid R. C., Prausnitz J. M., Poling B. E.: The properties of gases and liquids, McGraw-Hill (1987)

[62] Javurek M.: Simulation der Temperatur der Ausmauerung und Schmelze im Pfannenzyklus, Report for voest alpine (2008)

[63] Jr. Baukal C. E.: Heat Transfer in Industrial Combustion, CRC Press Inc., Boca Raton (2000)

[64] Starck A., Mühlbauer A., Kramer C.: Handbook of Thermoprocessing Technologies, Vulkan Verlag (2005)

[65] Investigations and measures to reduce emissions and energy consumption during the preheating of steel ladles, Research Fund for Coal and Steel, European Comission Community Research, Luxembourg (2008)

[66] Volkova O., Janke D.: Modelling of Temperature Distribution in Refractory Ladle Lining for Steelmaking, Iron and Steel Institute of Japan International, vol. 43, no. 8 (2003)

[67] Bender W., Sucker D., Niggeschmidt W.: Neuartiges thermisches Drehregenerator-Brenner-System zur besseren Energieausnutzung in Hochtemperatur-Prozeßfeuerungen, http://www.bine.info/fileadmin/content/Publikationen/Projekt-Infos/Zusatzinfos/2004-03_Vortrag.pdf (2009).

[68] Günther R.: Verbrennung und Feuerungen, Springer Verlag, Berlin (1974)

[69] Jr Baukal C. E.: Industrial Burners Handbook, CRC Press Inc., Boca Raton (2004)

[70] Kelly J., Dentella F., Recanati A., Visus J. E. M.: Oxygen Enhanced Ladle Preheating Systems: Improved Tap-to-tap Cycle Time and Operating Cost Reductions, 2010 AISTech Conference Proceedings, Pittsburgh (2010)

[71] Manthur P., Riley M. F., Nandi A., Nath R., Ghose A.: Improving Energy Efficiency and Reducing Emissions in the Steel Industry with Praxair's Oxy-Fuel Technologies, Steel Tech, no. 1 (2014)

[72] Scheele J., Ekman T.: Efficient heating with low calorific gases, Nordic Steel and Mining Review, no. 3 (2008)

[73] Cates L., Nakao T., Shimamoto T.: Performance and results of Praxair's DOC Technology for Lalde Preheating at Steel mill in Japan, 2011 AIST Conference, Indianapolis (2011)

[74] Milani A., Saponaro A.: Diluted combustion technologies, International Flame Research Foundation Combustion Journal (2001)

[75] AGA, Industrial Gases Denmark, http://www.aga.dk/en/processes_ren/melting_heating/ladle_heating/index.html.

[76] Bobek J., Scifres M., Hernandez M., Kelly J.: Stove Oxygen Enrichment at Arcelor Mittal's 7. Blast Furnace, 2008 AIST Conference (2008)

[77] promeos® - Porous Burner Technology, http://www.promeos.com/cms/front_content.php?idcat=256.

[78] B. Glaser, A Study on the Thermal State of Steelmaking Ladles, Doctoral Thesis, Division of Micro-Modelling, Department of Materials Science and Engineering, School of Industrial Enineering and Management, Sweden (2012)

[79] Glaser B., Görnerup M., Sichen D.: Fluid Flow and Heat Transfer in the Ladle during Teeming, Steel Research International, vol. 82, no. 7 (2011)

[80] Fredman T. P., Saxe'n H.: Model for Temperature Profile Estimation in the Refractory of a Metallurgical Ladle, Metallurgical and Mateterials Transactions B, vol. 29B (1998)

[81] Al-Harbi M., Al-Nefai A., Al-Jarallah S., Al-Dossary A., Jagan Y., Comprehensive CFD simulation of the ladle cycle toward lining service life optimization, Materials Science and Engineering, no. 33, pp. 1-9 (2012)

[82] Jin S., Auer T., Gruber D., Harmuth H., Fréchette M. H., Li Y.: Thermo-Mechanical Modelling of Steel Ladle Process Cycles, Interceram, no. 1, pp. 37-41 (2012)

[83] Poirier J., Gasser A., Boisse P.: Thermo-mechanical Modelling of Steel Ladle Refractory Structure, Interceram, vol. 54, no. 3 (2005)

[84] Gruber D., Harmuth H.: Thermomechanical Behaviour of Steel Ladle Linings and the Influence of Insulations, Steel Research International, vol. 85, no. 4 (2014)

[85] Volkova O., Sahebkar B., Hubalkova J., Aneziris C. G., Scheller P. R.: Ladle preheating procedure and its influence on the oxidation resistance of MgO-C refractories, UNITECR 2007, Dresden, Germany (2007)

[86] Warnatz J., Maas U., Dibble R. W.: Combustion. Physical and Chemical Fundamentals, Modeliung and Simulation, Experiments, Pollutant Formation, Springer Verlag, Berlin (1995)

[87] Fluent 6.3 User's Guide, Fluent Inc. (2006)

[88] Peters N.: Turbulent Combustion, Cambridge University Press (2000)

[89] Peters N.: Laminar diffusion flamelet models in non-premixed turbulent combustion, Progress in Energy and Combustion Science, vol. 10, no. 3, pp. 319-339 (1984)

[90] Peters N.: Fifteen Lectures on Laminar and Turbulent Combustion, Ercoftac Summer School, RWTH Aachen (1992)

[91] Baburic M.: Numerically efficient modelling of turbulent non-premixed flames, Doctoral Thesis, Faculty of Mechanical Engineering and Naval Architecture, University of Zagreb (2005)

[92] Yang B., Pope S. B.: Treating chemistry in combustion with detailed mechanisms-In situ adaptive tabulation in principle directions-Premixed combustion, Combustion and Flame, vol. 112, no. 1-2, pp. 85-112 (1998)

[93] Correa S. M., Gulati A.: Measurements and modelling of a bluff body stabilized flame, Combustion and Flame, vol. 89, Issue 2, p. 195 - 213 (1992)

[94] Rieger J.: Bildung und Konvertierung von Schadstoffen bei der thermischen Verwertung von Kuppelgasen, Doctoral Thesis, Chair of Process Technology and Industrial Environmental Protection, Montanuniversität Leoben (2013)

[95] Kreft A. J.: Beiträge zur Quantifizierung der Stickoxidbildung im Heizsystem einer Kokereibatterie mithilfe numerischer Strömungssimulation, Master Thesis, Chair of Process Technology and Industrial Environmental Protection, Montanuniversität Leoben (2008)

[96] Bredeberg J.: On the Wall Boundary Condition for Turbulence Models, Internal Report 00/4, Chalmers University of Technology (2000)

[97] Smith P. J., Shen Z. F., Friedman J. N.: Evaluation of Coefficients for the Weighted Sum of Gray Gases Model, Heat Transfer, vol. 104, pp. 602-608 (1982)

[98] Ferziger J. H., Peric M.: Computational Methods for Fluid Dynamics. 3rd edition, Springer-Verlag, Berlin (2002)

[99] Pyun S. I., Barin I.: Untersuchungen über die Kinetik des Kohlenstoffabbrandes aus den Teerdolomitsteinen mit gasförmigen Sauerstoff, Radex Rundschau, vols. 1-2, pp. 554-559 (1985)

[100] Spijker C. J.: Unsteady Laminar Flamelet Modellierung zur Beschreibung von Mündungsmischbrennern, Master Thesis, Chair of Thermal Processing, Montanuniversität Leoben (2010)

Appendix

Fig.A. 1: Chemical compositions of tested refractory materials. Averaged values are presented.

	M1			M2			M3			M4		
C	10.85	±	0.15	10.5	±	0.1	12.45	±	0.25	16.65	±	0.05
MgO	90.9	±	0	97.2	±	0	95.95	±	0.05	94.15	±	0.05
Al_2O_3	5.085	±	0.015	0.225	±	0.005	0.27	±	0	1.77	±	0.08
SiO_2	1.965	±	0.005	0.83	±	0.01	1.025	±	0.035	1.16	±	0.04
P_2O_5	0.04	±	0	0.045	±	0.005	0.065	±	0.005	0.05	±	0
SO_3	0.02	±		0.01	±		0.015	±	0.005	0.235	±	0.015
K_2O	0.02	±	0	0.015	±	0.005	0.025	±	0.005	0.02	±	0.01
CaO	0.92	±	0.01	1.02	±	0.01	1.855	±	0.035	1.62	±	0.01
TiO_2										0.02	±	0
Cr_2O_3	0.22	±	0	0.01	±		0.02	±	0	0.14	±	0.1
MnO	0.045	±	0.005	0.04	±	0	0.05	±	0	0.06	±	0
Fe_2O_3	0.7	±	0.01	0.51	±	0.01	0.595	±	0.015	0.685	±	0.065
ZrO_2	0.065	±	0.005	0.06	±	0.01	0.065	±	0.015	0.095	±	0.005
BaO	0.02	±	0	0.02	±		0.025	±	0.005	0.025	±	0.005
Total	100	±	0	100	±	0	100	±	0	100	±	0
Loss of ignition	9.905	±	0.095	11.65	±	0.05	13.5	±	0.3	18.9	±	0.2
Volatile components	2.28	±	0.09	2.12	±	0	2.565	±	0.055	3.65	±	0.05

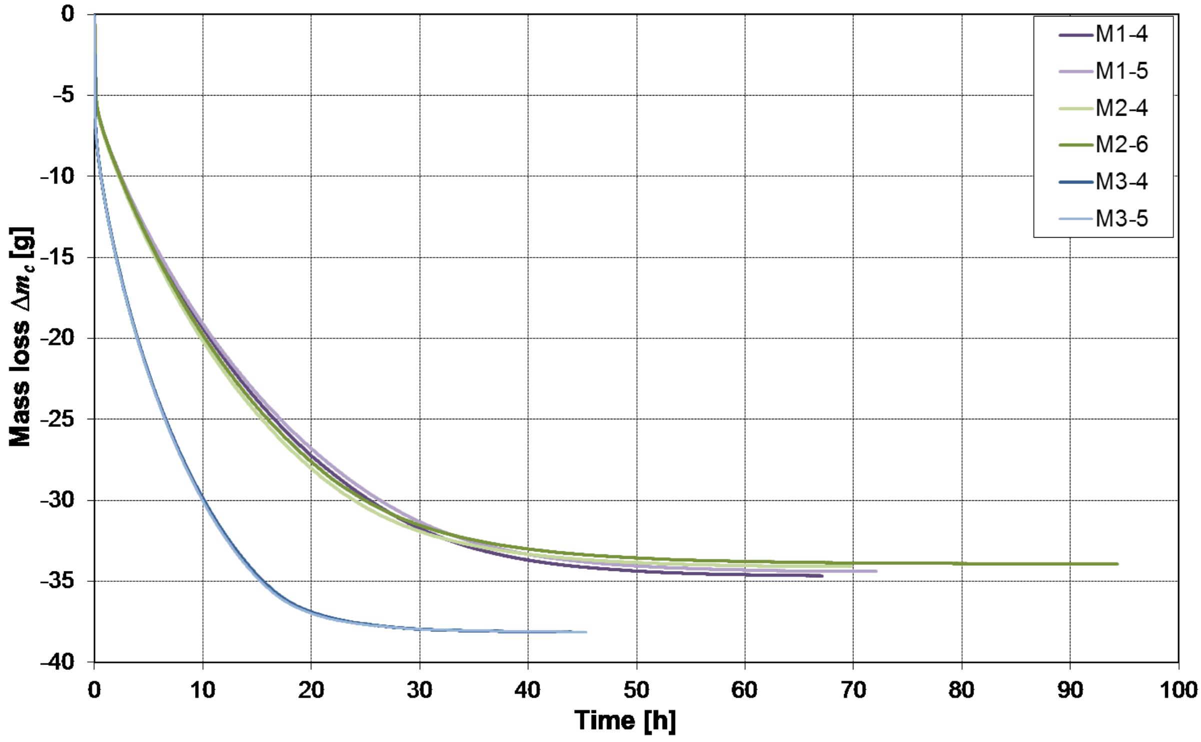

Fig.A. 2: Determination of the effective diffusion coefficient D_{eff} by TGA: mass loss of various MgO-C bricks at 700 °C.

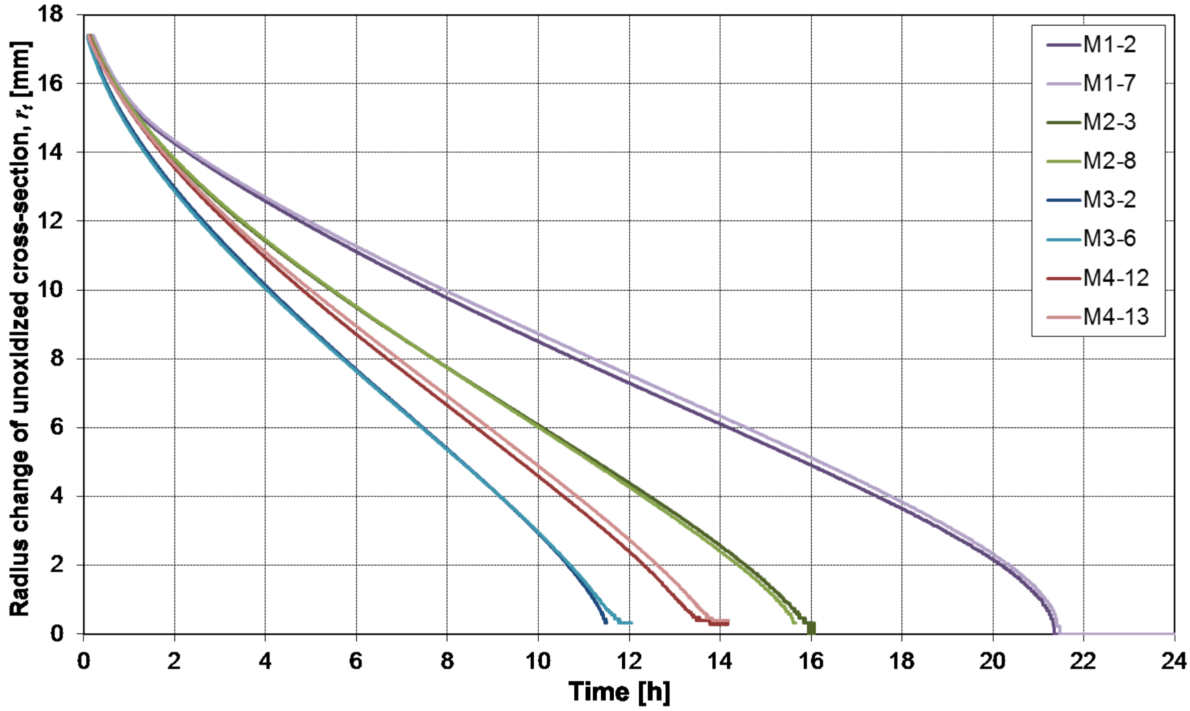

Fig.A. 3: Determination of the effective diffusion coefficient D_{eff} by TGA analysis: radius change of unoxidized cross-section for various refractory materials at 700 °C.

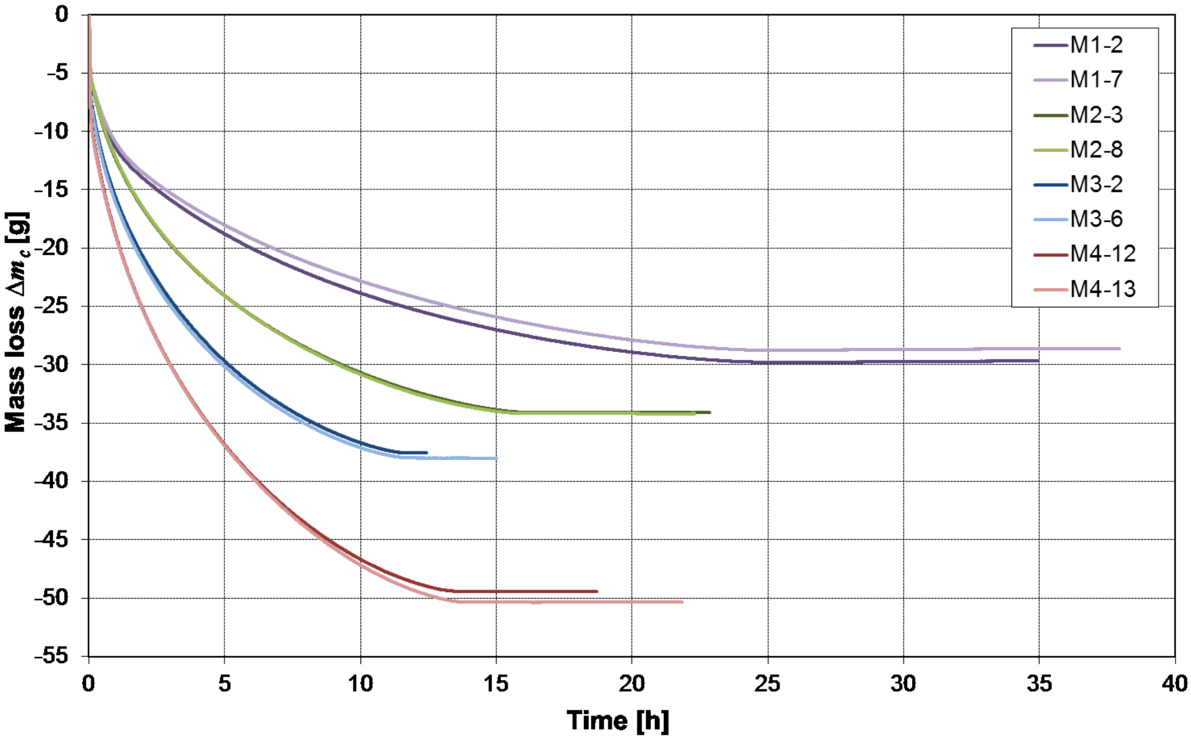

Fig.A. 4: Determination of the effective diffusion coefficient D_{eff} by TGA: mass loss of various MgO-C bricks at 900 °C.

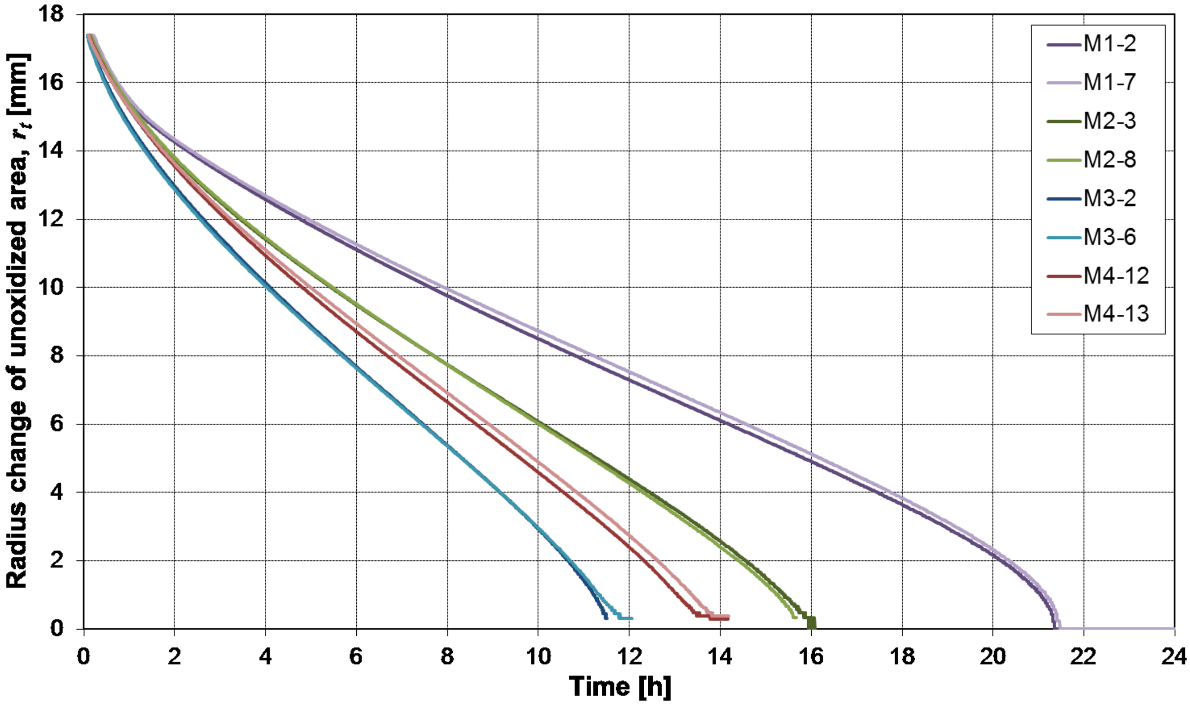

Fig.A. 5: Determination of the effective diffusion coefficient D_{eff} by TGA analysis: radius change of unoxidized cross-section for various refractory materials at 900 °C.

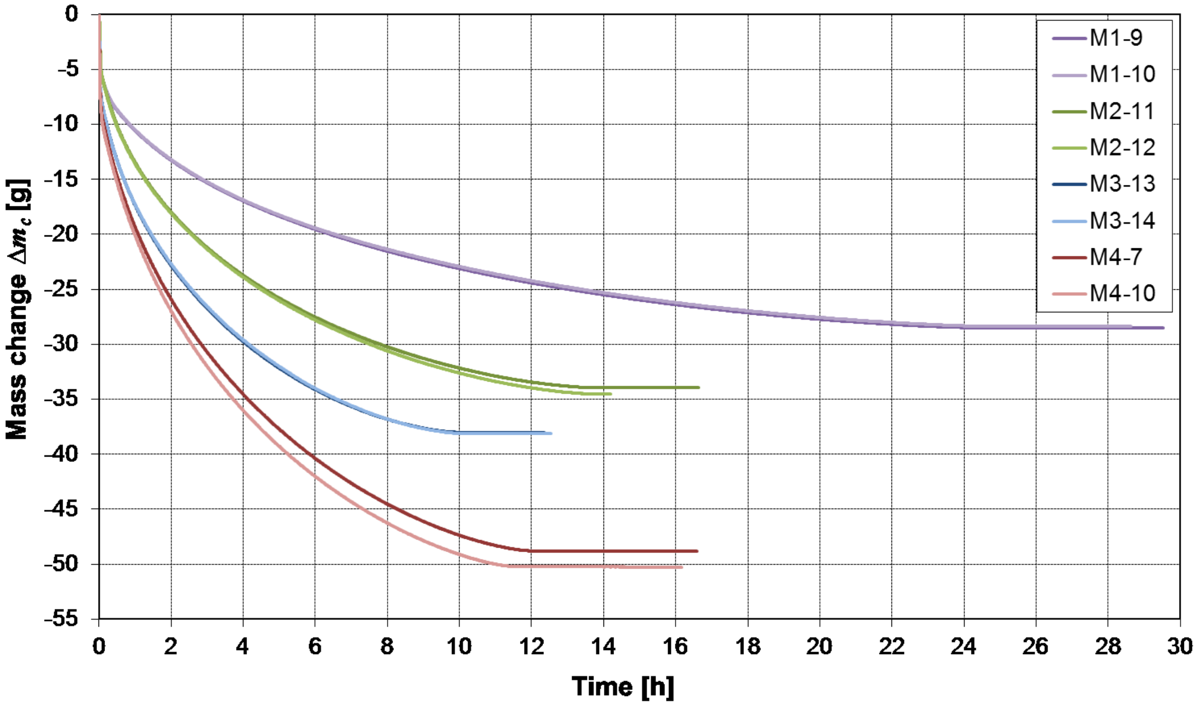

Fig.A. 6: Determination of the effective diffusion coefficient D_{eff} by TGA: mass loss of various MgO-C bricks at 1000 °C .

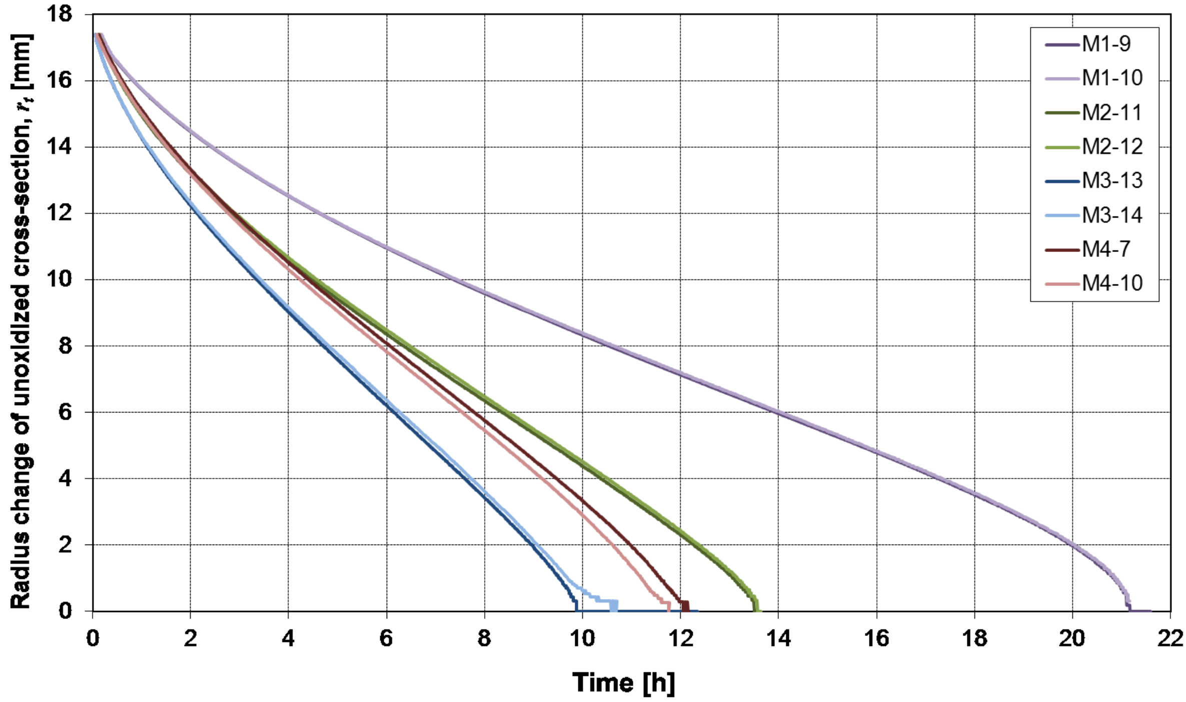

Fig.A. 7: Determination of the effective diffusion coefficient D_{eff} by TGA analysis: radius change of unoxidized cross-section for various refractory materials at 1000 °C .

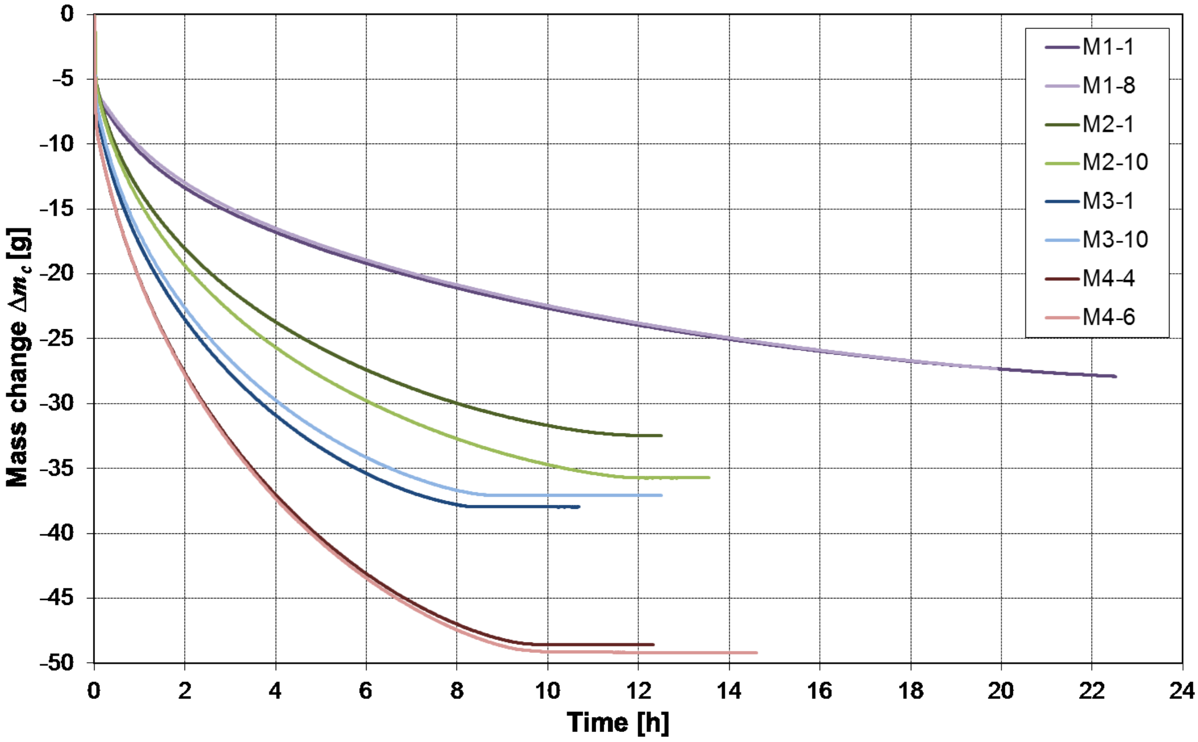

Fig.A. 8: Determination of the effective diffusion coefficient D_{eff} by TGA: mass loss of various MgO-C bricks at 1100 °C.

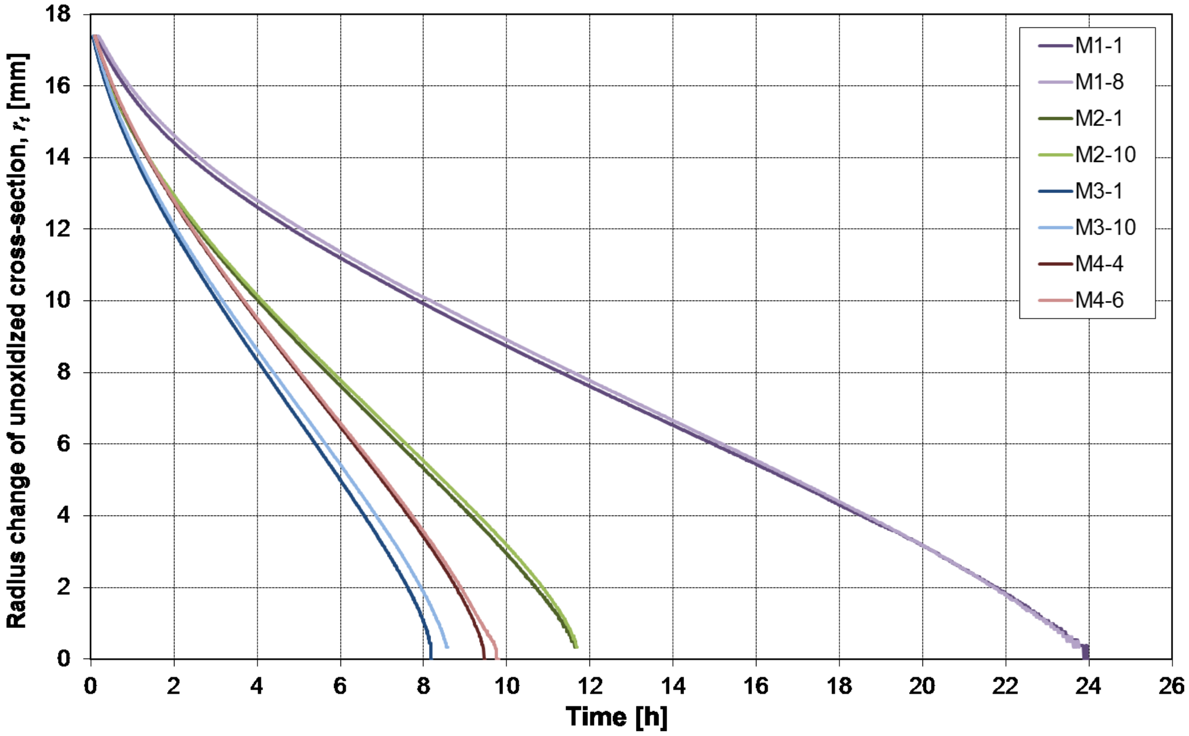

Fig.A. 9: Determination of the effective diffusion coefficient D_{eff} by TGA analysis: radius change of unoxidized cross-section for various refractory materials at 1100 °C.

Fig.A. 10: Determination of the effective diffusion coefficient D_{eff} by TGA analysis: coefficients from Eq. (7) determined by curve fitting of radius change of sample's unoxidized cross-section presented in Fig.A. 5 for temperature of 900 °C.

Equation: y = A*(x)^2*ln(x) + B*(x)^2+C*x+D

Sample	M1-2		M1-7	
R^2	1,000		1,000	
Coefficient	Value	Standard error	Value	Standard error
A	8,95E-02	1,65E-04	9,98E-02	3,24E-04
B	-2,86E-01	5,93E-04	-3,31E-01	1,15E-03
C	-9,28E-01	2,42E-03	-6,42E-01	4,60E-03
D	2,52E+01	3,59E-03	2,48E+01	6,73E-03
Sample	M2-3		M2-8	
R^2	0,999		1,000	
Coefficient	Value	Standard error	Value	Standard error
A	6,92E-02	4,00E-04	6,58E-02	6,46E-05
B	-2,30E-01	1,46E-03	-2,19E-01	2,38E-04
C	-3,50E-01	6,39E-03	-3,58E-01	1,03E-03
D	1,60E+01	1,06E-02	1,58E+01	1,68E-03
Sample	M3-2		M3-6	
R^2	0,999		1,000	
Coefficient	Value	Standard error	Value	Standard error
A	6,92E-02	4,00E-04	4,59E-02	1,68E-04
B	-2,30E-01	1,46E-03	-1,51E-01	6,09E-04
C	-3,50E-01	6,39E-03	-3,31E-01	2,53E-03
D	1,60E+01	1,06E-02	1,19E+01	3,80E-03
Sample	M4-12		M4-13	
R^2	1,000		1,000	
Coefficient	Value	Standard error	Value	Standard error
A	4,94E-02	6,37E-05	5,24E-02	1,05E-04
B	-1,64E-01	2,34E-04	-1,76E-01	3,87E-04
C	-3,79E-01	1,01E-03	-3,37E-01	1,67E-03
D	1,36E+01	1,60E-03	1,39E+01	2,67E-03

Fig.A. 11: Determination of the effective diffusion coefficient D_{eff} by TGA analysis: coefficients from Eq. (7) determined by curve fitting of radius change of sample's unoxidized cross-section presented in Fig.A. 7 for temperature of 1000 °C.

Equation: y = A*(x)^2*ln(x) + B*(x)^2+C*x+D

	M1-9		M1-10	
R^2	1,000		1,000	
	Value	Standard error	Value	Standard error
A	9,83E-02	1,37E-04	1,05E-01	1,59E-04
B	-3,16E-01	5,02E-04	-3,41E-01	5,83E-04
C	-7,95E-01	2,17E-03	-6,76E-01	2,53E-03
D	2,47E+01	3,51E-03	2,45E+01	4,10E-03
	M2-11		M2-12	
R^2	1,000		0,977	
	Value	Standard error	Value	Standard error
A	5,19E-02	4,99E-05	5,40E-02	3,04E-03
B	-1,68E-01	1,82E-04	-1,77E-01	1,12E-02
C	-4,31E-01	7,72E-04	-3,88E-01	4,90E-02
D	1,36E+01	1,20E-03	1,37E+01	8,11E-02
	M3-13		M3-14	
R^2	1,000		1,000	
	Value	Standard error	Value	Standard error
A	3,58E-02	4,80E-05	3,64E-02	1,20E-04
B	-1,17E-01	1,76E-04	-1,18E-01	4,46E-04
C	-3,18E-01	7,57E-04	-3,32E-01	2,02E-03
D	9,95E+00	1,21E-03	1,02E+01	3,51E-03
	M4-7		M4-10	
R^2	1,000		1,000	
	Value	Standard error	Value	Standard error
A	4,51E-02	8,98E-05	4,50E-02	1,02E-04
B	-1,52E-01	3,28E-04	-1,52E-01	3,72E-04
C	-2,84E-01	1,38E-03	-2,55E-01	1,58E-03
D	1,20E+01	2,14E-03	1,16E+01	2,46E-03

Fig.A. 12: Determination of the effective diffusion coefficient D_{eff} by TGA analysis: coefficients from Eq. (7) determined by curve fitting of radius change of sample's unoxidized cross-section presented in Fig.A. 9 for temperature of 1100 °C.

Equation: y = A*(x)^2*ln(x) + B*(x)^2+C*x+D

	M1-1		M1-8	
R^2	1,000		1,000	
	Value	Standard error	Value	Standard error
A	1,15E-01	9,24E-05	1,11E-01	2,06E-04
B	-3,85E-01	3,34E-04	-3,73E-01	7,55E-04
C	-4,06E-01	1,42E-03	-3,96E-01	3,23E-03
D	2,38E+01	2,33E-03	2,38E+01	5,07E-03
	M2-1		M2-10	
R^2	1,000		1,000	
	Value	Standard error	Value	Standard error
A	4,80E-02	3,49E-05	5,43E-02	2,99E-05
B	-1,59E-01	1,27E-04	-1,83E-01	1,10E-04
C	-2,93E-01	5,34E-04	-1,92E-01	4,84E-04
D	1,18E+01	8,35E-04	1,18E+01	8,04E-04
	M3-10		M3-11	
R^2	0,998		1,000	
	Value	Standard error	Value	Standard error
A	0,03518	0,00049472	0,03685	4,3882E-05
B	-0,12003	0,00182	-0,12549	0,00016144
C	-0,13274	0,00799	-0,13847	0,00070499
D	8,25547	0,01343	8,61496	0,00116
	M4-4		M4-6	
R^2	0,974		1,000	
	Value	Standard error	Value	Standard error
A	3,58E-02	2,99E-03	4,50E-02	1,02E-04
B	-1,22E-01	1,10E-02	-1,52E-01	3,72E-04
C	-2,06E-01	4,76E-02	-2,55E-01	1,58E-03
D	9,72E+00	7,65E-02	1,16E+01	2,46E-03

Fig.A. 13: Pre-exponential factor A and activation energy E_a of effective diffusion in MgO-C refractories for various sample types.

Sample	**A [m^2/s]**	**E_a [kJ/mol]**
M2	2.95*10^{-4}	31.54
M3	4.00*10^{-4}	30.00
M4	4.66*10^{-4}	29.98

Fig.A. 14: Details of executed graphite oxidation experiments at 1000 °C.

Sample	G2	G3	G4	G6	G7	G8	G9
Date	28.03.14	29.03.14	30.03.14	13.04.14	14.04.14	15.04.14	16.04.14
Flow rate [Nl/min]	5.30	10.32	1.80	11.27	7.70	5.30	2.77
Mass before experiment [g]	38.9	38.3	38.4	39.7	38.9	38.5	38.6
Mass after experiment [g]	34.2	31.8	35.7	31.6	33.6	33.5	33.7
Mass loss of carbon [g]	4.7	6.5	2.7	8.1	5.3	5.0	4.9

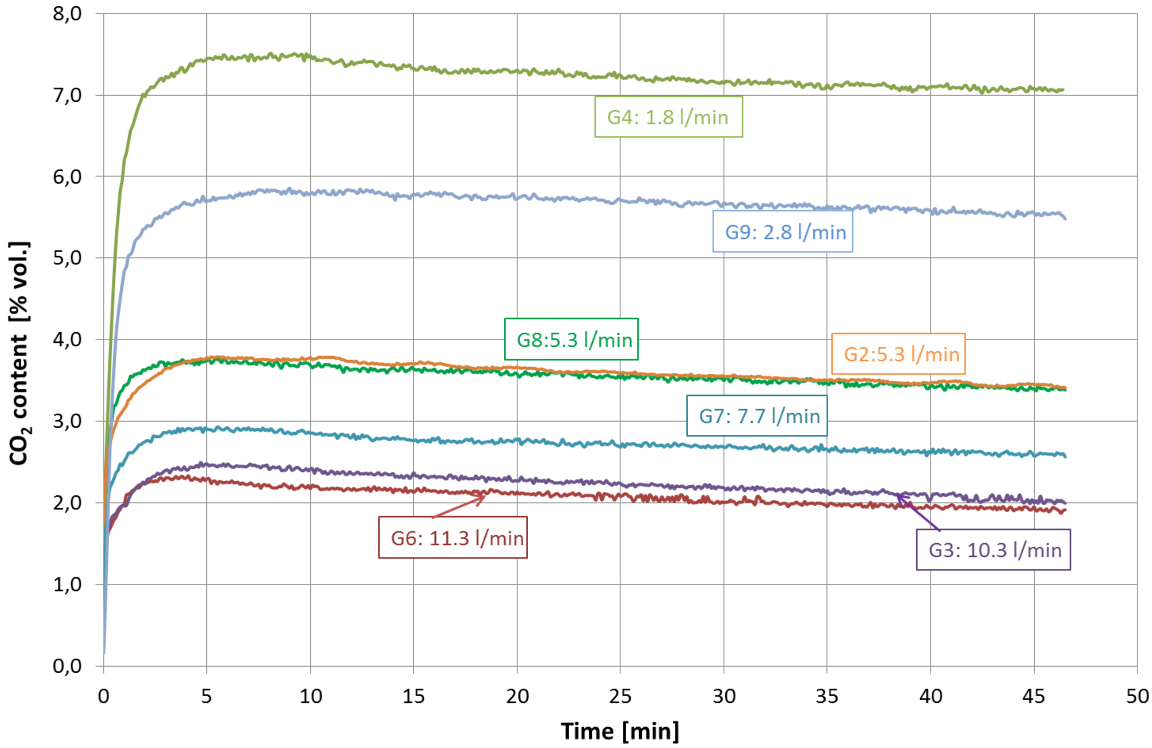

Fig.A. 15: Measured carbon dioxide content in exhaust gas during graphite oxidation tests for various flow rates and temperature of 1000 °C.

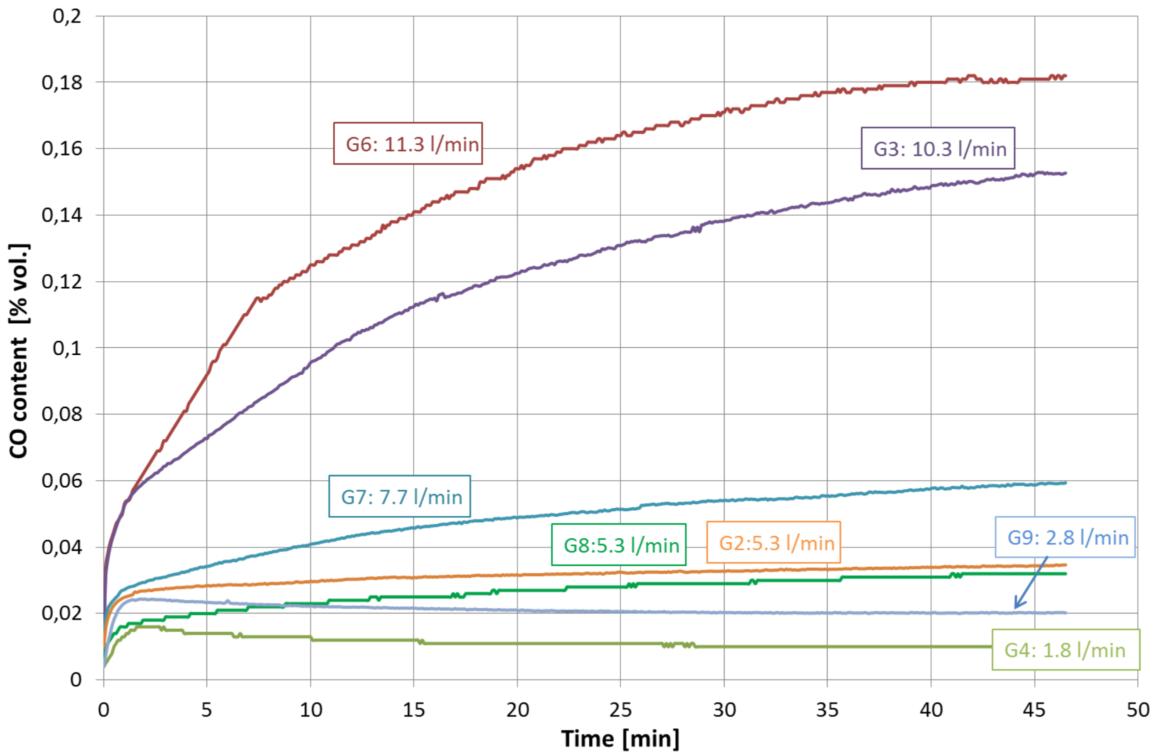

Fig.A. 16: Measured carbon monoxide content in exhaust gas during graphite oxidation tests for various flow rates and temperature of 1000 °C.

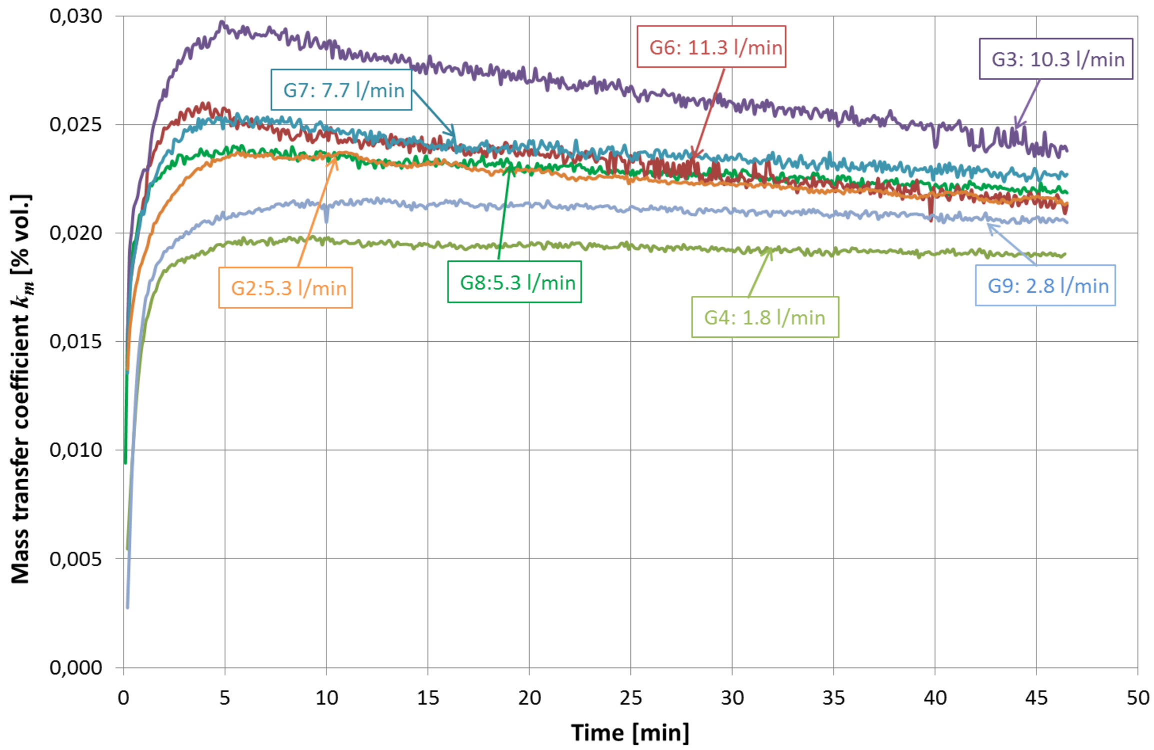

Fig.A. 17: Mass transfer coefficients determined within graphite oxidation tests at various flow rates for the temperature of 1000 °C.

Fig.A. 18: Graphite oxidation tests: CFD simulation data necessary for mass transfer coefficient calculation.

Flow rate [Nl/min]	Temp. [°C]	Velocity [m/s]	Viscosity [m^2/s]	D_G [m^2/s]	Sc [-]	Re [-]	Sh [-]	k_m [m/s]	$k_{m,av.}$ [m/s]
1.8	957	0.12	0.00018	0.00024	0.74	24.0	3.68	0.0255	0.0255
	968	0.12	0.00018	0.00024	0.75	23.9	3.68	0.0255	
2.8	924	0.18	0.00017	0.00024	0.78	35.9	3.70	0.0232	0.0234
	938	0.18	0.00017	0.00024	0.78	35.7	3.70	0.0237	
4.9	865	0.28	0.00015	0.00024	0.65	63.4	3.75	0.0259	0.0259
	881	0.29	0.00016	0.00024	0.66	63.0	3.73	0.0258	
5.3	855	0.30	0.00015	0.00024	0.64	67.8	3.76	0.0260	0.0260
	872	0.31	0.00016	0.00024	0.66	68.3	3.74	0.0259	
7.7	805	0.41	0.00014	0.00024	0.59	100.8	3.85	0.0266	0.0265
	821	0.42	0.00014	0.00024	0.61	100.6	3.81	0.0264	
10.3	757	0.52	0.00013	0.00024	0.55	135.8	3.97	0.0275	0.0273
	773	0.53	0.00013	0.00024	0.56	135.9	3.91	0.0271	
11.27	743	0.56	0.00013	0.00024	0.54	150.6	4.03	0.0279	0.0276
	759	0.57	0.00013	0.00024	0.55	149.3	3.96	0.0274	

Fig.A. 19: Details of executed MgO-C refractory oxidation experiments at 1000 °C.

Sample	Temperature [°C]	Flow rate [Nl/min]	Sample's length [cm]	Mass before coking [g]	Mass before experiment [g]	Mass after experiment [g]	Mass loss of carbon [g]
M28	900	5.1	16	520.4	510.8	499.1	11.7
M29	800	5.3	16	533.8	523.8	512.8	11
M30	700	5.2	16	527.9	518.4	512.8	5.6
M32	1000	5.3	8	264.0	259.4	254.7	4.7
M33	1000	10.3	8	271.2	266.6	261.0	5.6
M34	1000	2.7	8	266.4	261.9	256.7	5.2
M35	800	5.3	8	261.1	256.6	253.1	3.5
M36	600	5.4	8	255.6	251.1	250	1.1
M37	1000	7.7	8	259.5	255.1	249.4	5.7
M38	1000	10.2	8	252.80	248.1	242.6	5.5

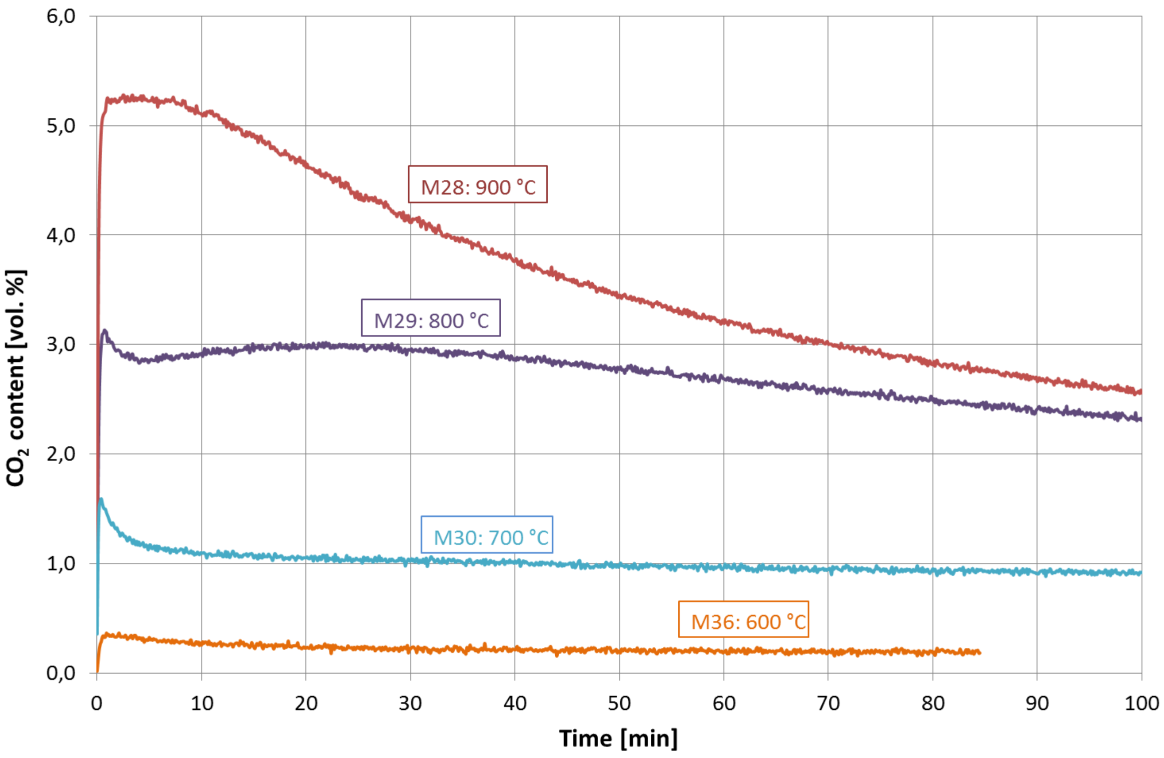

Fig.A. 20: Measured carbon dioxide content in exhaust gas during MgO-C refractory oxidation tests for various temperatures and flow rate of 5 Nl/min.

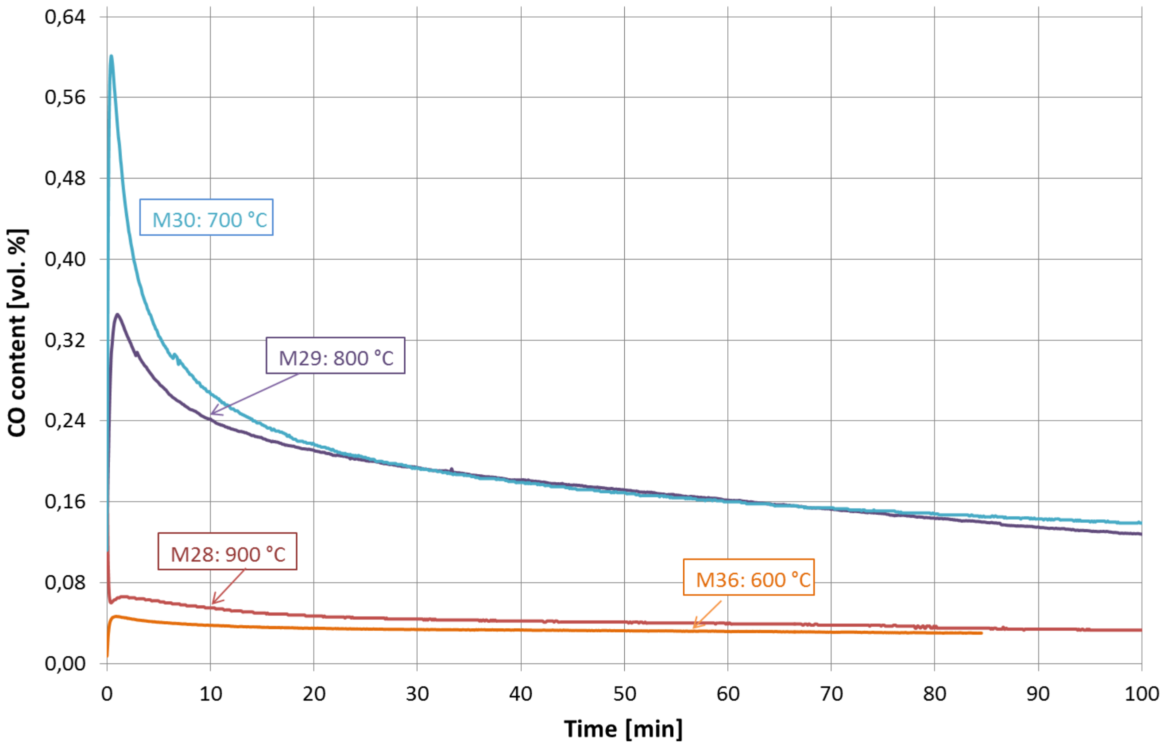

Fig.A. 21: Measured carbon monoxide content in exhaust gas during MgO-C refractory oxidation tests for various temperatures and flow rate of 5 Nl/min.

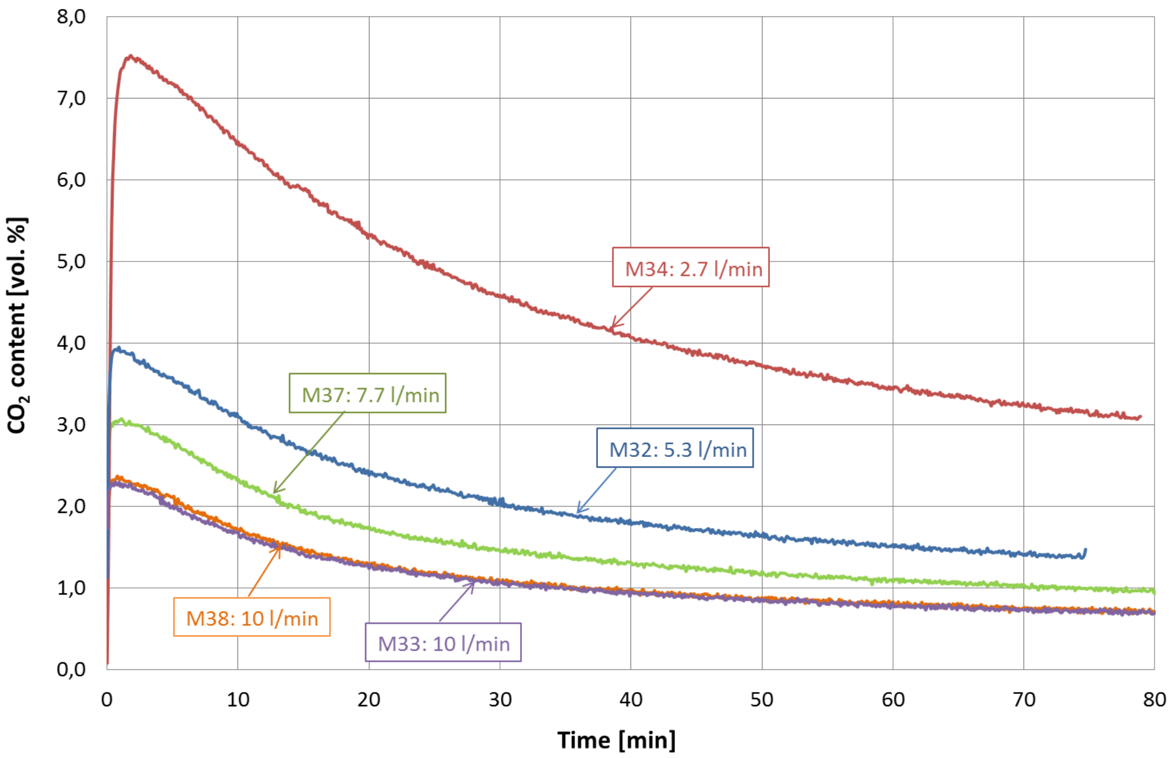

Fig.A. 22: Measured carbon dioxide content in exhaust gas during MgO-C refractory oxidation tests for various flow rates at temperature of 1000 °C.

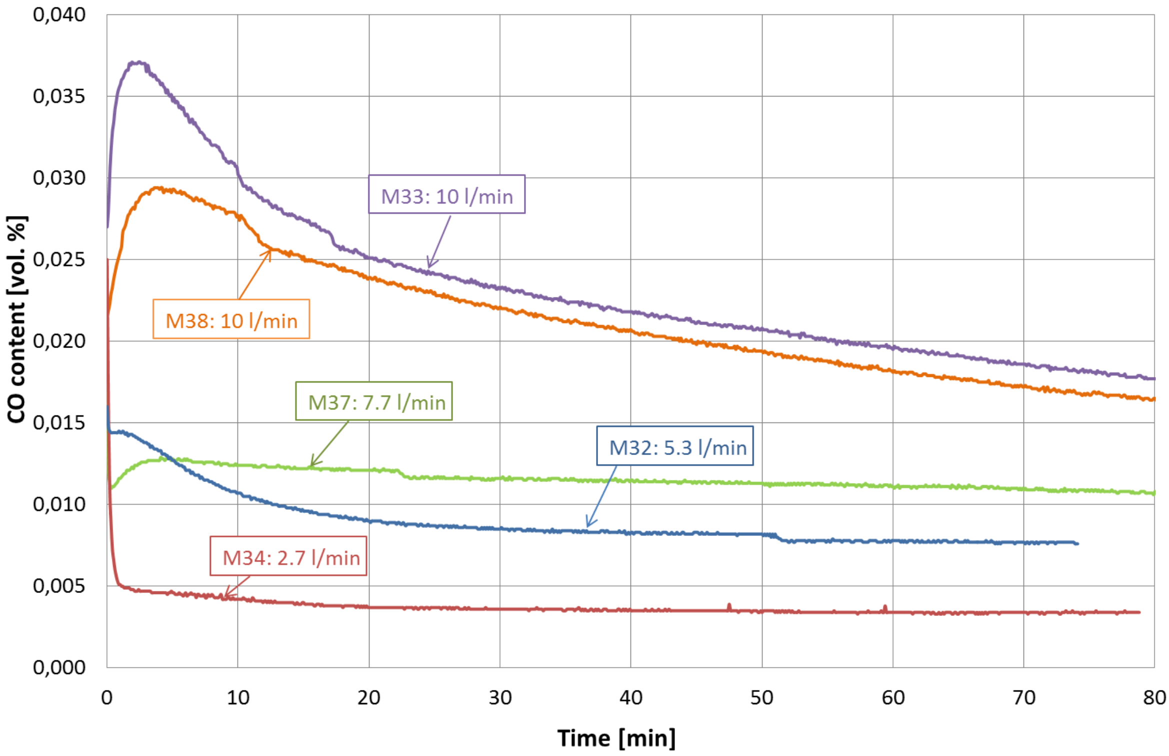

Fig.A. 23: Measured carbon monoxide content in exhaust gas during MgO-C refractory oxidation tests for various flow rates at temperature of 1000 °C.